Molecular modeling of the complexation of proteins with strong anionic polyelectrolytes

Dissertation

zur Erlangung des akademischen Grades

DOCTOR RERUM NATURALIUM

(Dr. rer. nat.)

im Fach Physik

eingereicht an der

Mathematisch-Naturwissenschaftlichen Fakultät
der Humboldt-Universität zu Berlin

von

Herrn MSc-Phys. Xiao Xu

Präsident der Humboldt-Universität zu Berlin
Prof. Dr. Sabine Kunst

Dekan der Mathematisch-Naturwissenschaftlichen Fakultät
Prof. Dr. Elmar Kulke

Gutachter: 1. Prof. Dr. Joachim Dzubiella
2. Dr. Stefan Kirstein
3. Prof. Dr. Felix Höfling

Tag der mündlichen Prüfung: 21.02.2018

List of publications

Chapter 4 [I, IV], **chapter 5** [II] and **chapter 6** [III] contain work from the following original papers published in peer-reviewed journals:

[I] X. Xu, M. Kanduč, J. Wu, and J. Dzubiella. "Potential of mean force and transient states in polyelectrolyte pair complexation". *J. Chem. Phys.* 145, 034901 (2016).

[II] X. Xu, Q. Ran, P. Dey, R. Nikam, R. Haag, M. Ballauff, and J. Dzubiella. "Charged Dendrimers Revisited: Effective Charge and Surface Potential of Dendritic Polyglycerol Sulfate". *Macromolecules* 50, 4759–4769 (2017).

[III] X. Xu, Q. Ran, P. Dey, R. Nikam, R. Haag, M. Ballauff, and J. Dzubiella. "Counterion-release entropy governs the inhibition of serum proteins by polyelectrolyte drugs". *Biomacromolecules* 19, 409–416 (2018).

[IV] S. Yu, X. Xu, C. Yigit, M. van der Giet, W. Zidek, J. Jankowski, J. Dzubiella, and M. Ballauff. "Interaction of human serum albumin with short polyelectrolytes: a study by calorimetry and computer simulations". *Soft Matter* 11, 4630–4639 (2015).

Not included in this thesis are:

[V] F. Schwoerer, M. Trapp, X. Xu, O. Soltwedel, J. Dzubiella, R. Steitz, and R. Dahint. "Drastic Swelling of Lipid Oligobilayers by Polyelectrolytes - A Potential Molecular Model for the Internal Structure of Lubricating Films in Mammalian Joints". *Langmuir* 34, 1287 (2018).

[VI] Q. Ran, X. Xu, P. Dey, S. Yu, Y. Lu, J. Dzubiella, R. Haag, and M. Ballauff. "Interaction of human serum albumin with dendritic polyglycerol sulfate: A comparison of calorimetry with simulations" (2018). *J. Chem. Phys.*, Submitted.

[VII] Q. Ran, X. Xu, R. Haag, J. Dzubiella, and M. Ballauff. "Binding of lysozyme to a charged dendrimer: The effect of salt and temperature" (2018). In preparation.

Statement of author's contribution

Paper I: I built up the simulation system, processed the data, carried out all calculations and wrote the paper. Dr. Matej Kanduć and Prof. Dr. J. Wu provided insightful suggestions and revised the paper. This research study was supervised by Prof. Dr. J. Dzubiella.

Paper II: I conducted all simulations, developed the coarse-grained force field, analyzed the electrostatic properties of the dendrimers and wrote the paper. Qidi Ran performed the Zetasizer experiments. Prof. Dr. R. Hagg and Prof. Dr. M. Ballauff provided insightful suggestions and revised the paper. This research study was supervised by Prof. Dr. J. Dzubiella.

Paper III: I carried out the coarse-grained simulations, analyzed the data, and wrote the paper. Qidi Ran performed isothermal titration calorimetry experiments. P. Dey synthesized the dendrimers and R. Nikam conducted atomistic simulations. Prof. Dr. R. Hagg and Prof. Dr. M. Ballauff provided insightful suggestions and revised the paper. This research study was supervised by Prof. Dr. J. Dzubiella.

Paper IV: I performed the coarse-grained simulations to support the isothermal titration calorimetry experiments carried out by Dr. Shun Yu. This research study was supervised by Prof. Dr. M. Ballauff and Prof. Dr. J. Dzubiella.

Abstract

Electrostatically driven complexation in nature has been long realized with its important roles for regulating biological processes and drug design. A system predominantly of electrostatic nature is the protein associated with strong ionic polyelectrolytes. The dominance of electrostatics offers great chances for exogenous control of the binding affinity of macromolecules and the resultant complex, by manipulating the electrostatic properties of the molecules. Despite the simplicity of the electrostatic interactions between charges governed by Coulomb's law, the complexity of the association escalates on the account of the intermolecular interactions as well as individual interactions with water and counterions. A deeper insight into the physicochemical properties and the modeling of the association process thus requires the use of more advanced methods, via both computational and experimental means.

In this thesis, we conducted a comprehensive study of the electrostatic complexation between proteins and anionic linear/dendritic polyelectrolytes, by means of molecular dynamics simulations with implicit solvent and explicit salt. The proteins and polyelectrolytes are both represented in a coarse-grained fashion. Each coarse-gained segment represents either an amino acid residue or the repeating chemical subunit of the polyelectrolyte. This modeling strategy allows for simulations of big proteins such as human serum albumin and dendritic polyelectrolytes of large generations, while the crucial molecular electrostatic properties are still well retained. Our simulations are validated further by calorimetry experiments. Finally, we propose theories based on counterion condensation and charge renormalization for interpreting the system binding free energies.

Regarding all systems investigated here, the thesis demonstrates the crucial and ubiquitous role of condensed counterions which participates in the electrostatic complexation. For both linear and dendritic polyelectrolytes, we find a strong charge renormalization induced by the condensed counterions, which consequently suppresses electrostatic interactions to an appreciable extent. The resultant binding is governed by the release of those condensed counterions, resulting in a massive entropy gain. Due to the presence of the multivalent binding, we propose a new interpretation of the conventional Langmuir adsorption isotherm, which ensures a meaningful comparison between simulations and experiments.

This thesis proposes an entire methodology ranging from the characterization of the molecular effective charge to the ultimate calculation of the binding affinity. With that, our findings provide an elegant access to the quantitative understanding of the electrostatic complexation between proteins and polymeric ligands. We also believe that our results open a new perspective for the rational design of charged polymeric drugs.

Zusammenfassung

Elektrostatisch gesteuerte Komplexierung spielt eine wichtige Rolle bei der Regulierung biologischer Prozesse und ist daher äußerst bedeutend für Arzneimittel-Designverfahren. Komplexierung eröffnet weitreichende Möglichkeiten in der exogenen Kontrolle der Bindungsaffinität von Makromolekülen durch Einflussnahme auf ihre elektrostatischen Eigenschaften. Ein in diesem Kontext relevantes System besteht aus einem Protein, das mit stark geladenen ionischen Elektrolyten assoziiert ist. Trotz der einfachen Natur der elektrostatischen Wechselwirkungen zwischen den Ladungen (bestimmt durch das Coulombsche Gesetz), wächst die Komplexität der Assoziation aufgrund von Vielteilchenwechselwirkungen sowie individuellen Wechselwirkungen mit Wasser und mit Gegenionen enorm an. Eine tiefere Einsicht in die physiko-chemischen Eigenschaften und in die Modellierung des Assoziations-Prozesses erfordert neue, fortgeschrittene experimentelle Methoden und Computermodelle.

In dieser Arbeit untersuchen wir die elektrostatische Komplexierung zwischen Proteinen und anionischen, linearen bzw. dendritischen Polyelektrolyten mittels Molekulardynamik Simulationen in implizitem Lösungsmittel und mit expliziten Salzen. Die Proteine und Polyelektrolyte werden mit vergröberten Details simuliert. Jedes vergröberte Segment repräsentiert eine Aminosäure oder eine sich wiederholende chemische Untereinheit des Polyelektrolyten. Die Vergröberung ermöglicht Simulationen von großen Proteinen wie Humanalbumin oder dendritischen Polyelektrolyten, ohne dabei die essentiellen elektrostatischen Eigenschaften der Moleküle zu vernachlässigen. Wir validieren unsere Simulationen durch Kalorimetrieexperimente. Zur Interpretation der resultierenden Bindungs-freien Energien schlagen wir Theorien vor, die auf Gegenionen-Kondensation und Ladungs-Renormalisierung basieren.

Die Arbeit zeigt die äußerst wichtige Bedeutung der kondensierten Gegenionen auf, die in allen untersuchten Systemen an der elektrostatischen Komplexierung teilhaben. Sowohl bei linearen als auch dendritischen Polyelektrolyten bewirken die kondensierten Gegenionen Ladungsrenormalisierung, die die elektrostatischen Wechselwirkungen in den Systemen abschwächt. Die Bindung wird durch die Freisetzung von Gegenionen bewirkt, was mit einem massiven Anstieg der Entropie einhergeht. Aufgrund der multivalenten Bindung können unsere Ergebnisse nicht mithilfe des konventionellen Langmuir-Adsorptionsisothermen interpretiert werden. Daher schlagen wir eine neuartige Interpretation der Langmuir-Adsorption sisothermen vor, die einen sinnvollen Vergleich zwischen Simulationen und Experimenten ermöglicht.

In dieser Arbeit entwickeln wir eine Reihe von allgemein anwendbaren und eleganten Methoden, die uns, angefangen mit der Charakterisierung der effektiven Molekularladung bis zur Berechnung der Bindungsaffinität, ein besseres quantitatives Verständnis für die elektrostatische Komplexierung zwischen Proteinen und Polymeren geben. Wir sind zudem überzeugt, dass unsere Ergebnisse neue Wege für die Entwicklung von Arzneimitteln eröffnen, die auf geladenen Polymeren basieren.

Contents

1 Introduction

All functions of living systems ranging from primitive bacteria to higher-order organisms, as well as their interactions with their surroundings, are realized through macromolecular interactions. These interactions might be simple or rather complex, with at least one of the partners being a biological macromolecule, usually a protein. Proteins are large biomolecules, with the primary structure consisting of one or more sequences of amino acid residues, linked through peptide chains. They are abundant in number and carry out a wide range of functions in the body. The protein can serve as an antibody, binding to specific foreign particles, such as viruses and bacteria, to help protect the body. Transport proteins, such as human serum albumin (HSA) or Ferritin, can bind and carry atoms and small molecules within cells throughout the body. Similar functions of proteins in biological science are ubiquitous, ranging from structural (cytoskeleton), mechanical (muscle), biochemical (enzymes), to cell signaling (hormones) processes. Essentially, a protein realizes its biological function by directly interacting with other molecules [1].

The protein association with ligands results from different types of interactions. As the building block of proteins, amino acids can be classified based on their propensity in contact with a polar solvent (such as water). For hydrophobic ones (low propensity to be in contact with the solvent), they build non-polar or hydrophobic parts of the peptide chains which are well hidden in the protein interior. As a result, proteins possess the ability to address ligands via hydrophobic attractions. On the contrary, hydrophilic amino acids (in favor of bonding with the solvent) create electronic displacements, leading to a local dipole moment or even net charges on acidic or alkaline amino acids. The protein accordingly carries specific dipole moments and charged patches of nonzero net charges, which forms the basis for electrostatic interactions with solution ions and charged ligands [4, 5, 6].

In spite of the complex nature of protein-ligand interactions, the presence of the protein in a highly protonated state or the ligand with many charges can make the electrostatic interaction dominant for the complexation. In case of protein-DNA complexation which is found responsible for the control of the information stored in the genome, electrostatic interactions entirely govern the complexation [7]. Moreover, the interactions between the protein and its charged ligands result predominantly from its charged patches [4]. Other preliminary examples include the interaction of antibody-antigen, enzyme-inhibitor, potassium channel-peptide inhibitor and so forth [8]. Understanding of the above processes in general is related to protein electrostatics, which includes not only direct charge-charge interactions between the protein and the ligand, but also hydrogen bonding, salt bridges and metal interactions [9].

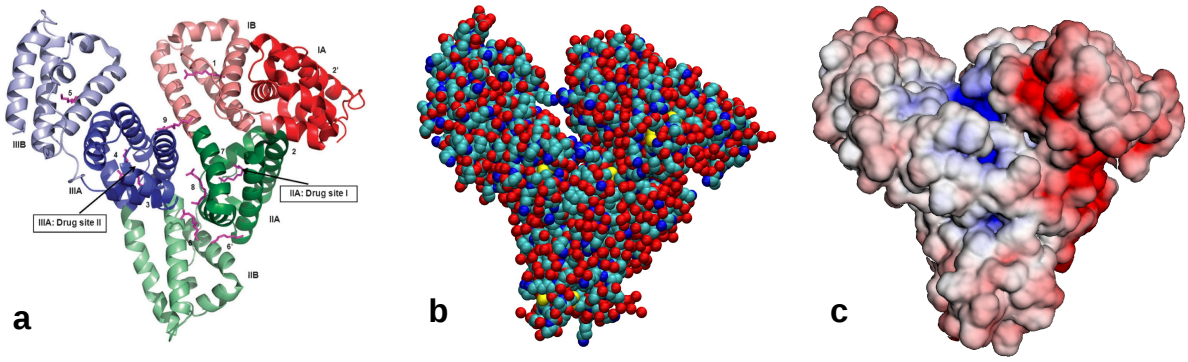

Figure 1.1: The HSA is plotted in terms of (a) three polypeptide domains [2], (b) the atomistic structure and (c) the surface electrostatic potential. In panel (a) we show the three HSA domains color coded and labeled I-III (each with two sub-domains A and B). In panel (b), the carbon, nitrogen, oxygen, and sulfate atoms are depicted by green, blue, red, and yellow spheres, respectively. The HSA surface potential is calculated by Adaptive Poisson-Boltzmann Solver [3] in physiological pH conditions.

The awareness that protein complexation is dominated by electrostatics has motivated a bunch of applications in biophysics and technological science. An important situation that takes advantage of electrostatic complexation is the the adsorption of proteins on surfaces, which appears to be a central issue for developing certain biomaterials and medical devices. The insights into protein electrostatic interactions with a surface give access to the way reducing strong nonspecific protein adsorption on implant surfaces, which consequently increases the effectiveness of membranes and biosensors as well as facilitates drug releasing from delivery vehicles [10]. As opposed to that, from the perspective of the pharmaceutical industry, the discovery of a ligand with a desirable protein binding affinity has become one of the major preoccupations for drug development in an early stage [11]. Recently, biomaterials with polymeric coatings and dendritic polymeric carriers with desirable protein binding affinity were developed [10]. In that regard, a comprehensive, large-scale comparative study on protein-ligand complexation with different electrostatic properties may uncover principles that inspire the ligand design.

The first challenge to understand the electrostatic complexation starts from a resolution of the electrostatic potential of the charged molecule. Apparently, this potential is not only a function of the molecular intrinsic charging properties, but also depends on the interacting salt and solvent. Note that the experimentally measured surface potential of the charged molecule has been found with a great deviation from the value that calculated by its intrinsic charges [12, 13]. Thus, it becomes crucial to understand this charge renormalization, and more importantly, to properly define the molecular charge and potential after the charge renormalization. However, consistent theoretical definitions in that aspect are still lacking, which further hinders a tractable theory to describe the electrostatic complexation. In particular, quite a few studies had pointed out that this charge renormalization directly

impacts on the molecular physiochemical properties [12, 14, 15].

A second challenge to study the electrostatic complexation is due to the promiscuity of the interactions, namely, the hydrophobic and electrostatic forces between the protein and ligands come into play simultaneously. Although for the electrostatic complexation, the hydrophobic forces are of minor importance, the remaining electrostatic interactions indeed cover both the charge-charge and the protein/ligand-salts/solvent interactions. In particular, the presence of the protein/ligand-salts/solvent interactions indicates the coupling between charged molecules and solution environment, which has been found vital for determining the binding free energy and the phase diagram of charged molecules [16, 17, 18, 19]. An example in that respect refers to the charged polymer chain. The condensed counterions from the solution environment can trigger polymer contraction under certain conditions, in spite of intra-chain charge-charge repulsions. This particular role of salts/solvent in the electrostatic complexation hinders the understanding of the molecular association and frustrates ligand design based on its electrostatic properties.

The third challenge arises from the requirement for a theoretical formalism to address the complexation energy between charged macromolecules. At the bio-environment, charged macromolecules are usually mediated by polar solvents (water) and solvated salts. As a result, the electrostatic potential arising from the charged molecule is screened both by salt ions and polar solvents (usually treated as a dielectric background continuum). The analytical resolution of the electrostatic potential was initialized by the Possion-Boltzmann theory. The adoption of that theory has demonstrated that, at the far field, the electrostatic potential decays in an exponential manner with distance [20], in response to a number of diffusive ions. As opposed to that, at the near field, the potential deviates greatly from the previous exponential decay, given the correlated condensed ions layer that is triggered by the high surface potential. Apparently, the resultant complexation energy is contributed both by the energy change in the far and the near field. It would be desirable, if one can decouple these two energy terms, which may lead to a full theoretical prediction of the complexation energy.

To address these challenges, we perform a comprehensive molecular modeling of the proteins interacting with highly charged anionic ligands. The ligands under investigation are restricted to anionic polyelectrolytes (PEs). They are macromolecules with ionizable groups that can release cations into the solution and leave negative charges on the polymer chains in a polar environment. If the charges are strong enough, the interactions of PEs with other macromolecules are governed by electrostatics, as evidenced by various important applications in many areas of natural sciences, ranging from materials to biophysics [21]. In this thesis, we concentrate on linear and dendritic PEs, with an emphasis on their electrostatic

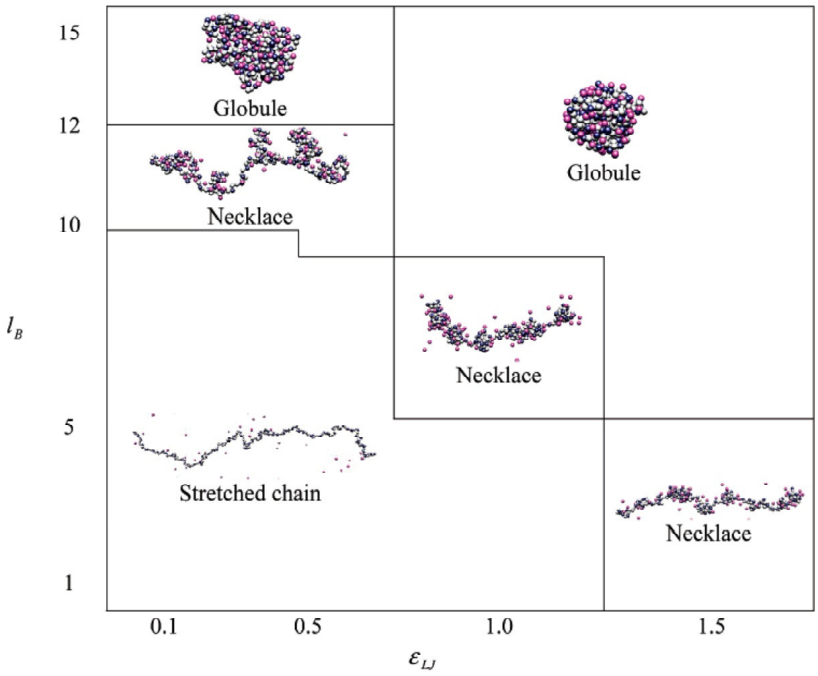

Figure 1.2: Typical conformations of PE chain with degree of polymerization $N = 304$ and fraction of charged monomers $f = 1/3$ [29]. The x and y-axis denotes the magnitude of the nonbonded and electrostatic interaction, respectively.

properties.

Linear PEs (LPEs) have the simplest structure in the PE family. A LPE is a polymer chain composed of many (poly) repeating units joined together. Those units typically have ionizable side groups dissociated in polar solvents at neutral pH of 7. LPE has properties of both electrolytes (salts) and polymers (high molecular weight molecules). LPE solutions are electrically conductive, such as salts, and often viscous like polymers. The status of the ion dissociation gives rise to 'strong' or 'weak' LPEs. Examples like cationic LPEs possessing quaternary ammonium groups and anionic LPEs like poly(sodium styrene sulfonate) (NaPSS) that dissociate completely in solvents are considered as strong LPEs. Poly(acrylic acid) (PAA) instead, only partially dissociates, is categorized as a 'weak' LPE. The dissociated LPE is electrically conductive and consequently yields distinct properties compared with non-ionic polymers. Therefore, LPEs are often used in the development of lithium batteries and proton exchange membranes for fuel cell technology [22, 23]. In addition, LPE complexes (LPECs), the product formed by the profound electrostatic interactions, are an ideal tool for protein separation [24, 25], film fabrication [26], and even gene therapy [27, 28].

Due to the highly charged nature, LPEs interact strongly with polar solvents and salts. Depending on those interactions, LPEs' conformations correlate with the solution environment. A minimal example is presented in Fig. 1.2 [29], where a diagram of LPE conforma-

tions is sketched in terms of the electrostatic interaction parameter l_B, and the short-ranged nonbonded interaction parameter ϵ_{LJ}. In the presence of weak or strong short-ranged nonbonded attractions, the LPE reasonably possesses an elongated or contracted state, respectively. However, the globular state resolved from Fig. 1.2 in the upper limit of electrostatics conflicts with the expected elongated state, in view of the underlying strong electrostatic repulsions. This discrepancy indicates a drastic reduction of the polymeric net charge and intrachain repulsion, which is attributed to the counterion condensation in response to the increasing electrostatics. This modulation of the LPE charges by counterions will notably affect the complexation behavior with proteins, which constitutes an important topic of this thesis.

Other than LPEs, dendritic polyelectrolytes (charged dendrimers) are a class of artificial macromolecules with a tree-like (hyperbranched) architecture emanating from a central core. The dendrimer of the so-called generation zero consists of a multifunctional core with chemical bonds linking the dendritic branching groups in the first outer layer. The successive layers are created by iteratively adding shells to the dendritic branching groups of the layer beneath, which constitutes a dendrimer of a higher generation, cf. Fig. 1.3(a). The homogeneous structure among the branching groups facilitates the synthesis of the dendrimer on a kilogram scale and in a broad range of molecule weight, even though the resultant dendrimer is hyperbranched, possessing a fraction of linear defects. The dendrimer properties rest much on the multifunctional groups represented by the terminal segments. If the terminal groups are acidic or alkaline, the dendrimer gets charged in polar solvents.

The dendritic structure has inspired many applications of the dendrimer. The first synthesized and now commercialized charged dendrimers were polyamidoamines (PAMAMs). For the cationic PAMAM, possessing primary amine terminal groups, the induced electrostatic interactions make PAMAM-amine participate in complexing with DNA, siRNA and solvable proteins [31, 32]. An excellent ability of forming PAMAM-DNA complexes results in PAMAM's widespread uses as a commercial DNA transfection kit [33], while the conjugation with proteins often provides the basis of PAMAM to modulate the biological responses of proteins [34]. The conjugation with charged dendrimers is not always favorable. For instance, the association of the charged dendrimer with erythrocyte membrane proteins can result in changes of the protein conformations, which can make "Cationic" dendrimers generally haemolytic and cytotoxic [35]. These changes, which increase with the dendrimer generation and the concentration, still remain poorly understood. Other applications of charged dendrimers arise from the presence of internal cavities. Small drug molecules can be encapsulated in these cavities, which results in the applications of dendrimers as drug delivery platforms. In particular, the spatial structure of the charged dendrimer shows a

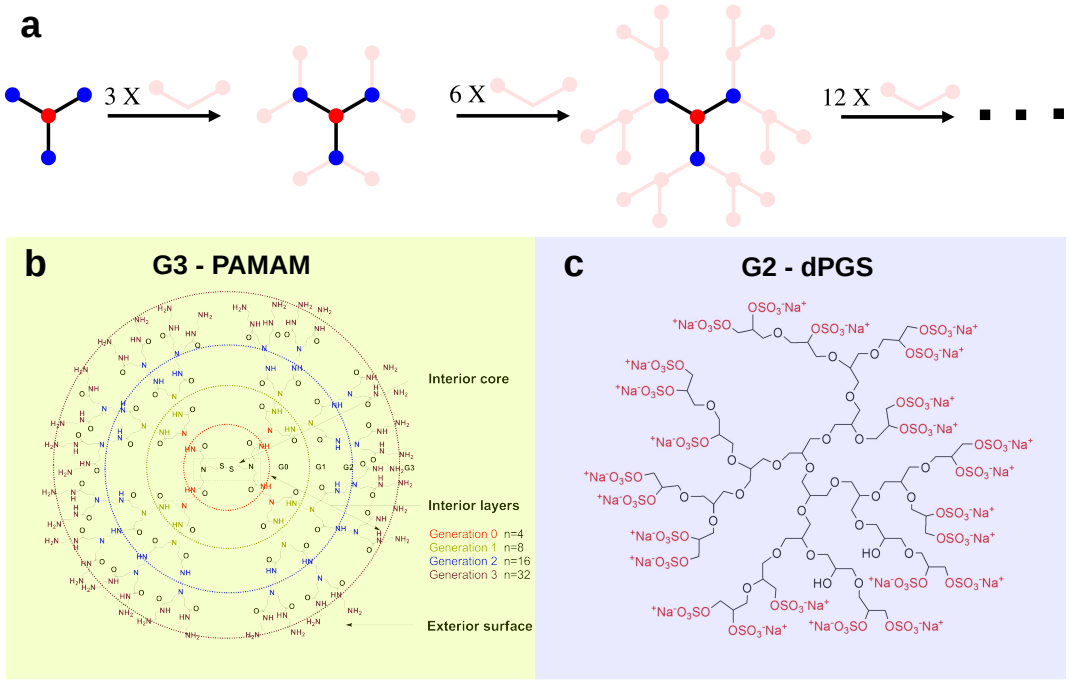

Figure 1.3: (a) The schematic process of the dendrimer growth in terms of generations. The red and blue circles stand for the core and the branching dendritic chemical subunits, respectively. (b) and (c) [30] severally depicts the chemical structure of the G3-PAMAM and G2-dPGS macromolecule.

sensitive response to the salt concentration, temperature and the pH of the environment [36, 37, 38], which enables the release of drug molecules from the dendrimer in a well controlled manner.

Another charged dendrimer that becomes increasingly important is dendritic polyglycerol sulfate (dPGS). The dPGS can be easily synthesized on a kilogram scale consisting of glycerol repeating units and sulfate terminal groups [39, 40]. The most important property of dPGS arises from the known high binding affinity with L/P-selectin, which makes dPGS a potent anti-inflammatory drug regarding the chronic inflammation process [30]. The dendritic structure offers dPGS greater variability compared with other anti-inflammatory drugs. After the conjugation of the drug molecules to the dPGS, the drug molecules can be efficiently transported to the inflamed tissues on the basis of the dPGS inflammation-targeting properties. For instance, dPGS can deliver paclitaxel (PTX) to tumor cells. The amount of the dPGS-PTX conjugated in the tumor cells is shown as non saturable [41]. As a highly anionic macromolecule in solution, the high binding affinity with L-selectin and thus the anti-inflammatory potential is primarily due to electrostatic interactions [30]. In this thesis, we will amend this concept after a systematic study of the dPGS-selectin complexation. We demonstrate, counterions play a vital role for the complexation between the protein and the heavily charged dendrimer. The binding is driven by the released counterions that are previously sitting on the dendrimer surface. In that regard, the incoming L-selectin or other

ligands have to compete with ions and displace counterions. Such ionic exchange processes are the key to understanding the high dPGS anti-inflammatory potential and the stability of the binding complexes formed.

2 Aims of the thesis

Driven by the need to have a comprehensive understanding of the protein-ligand complexation that is predominantly of electrostatic nature, the thesis aims at unraveling the driving force of the complexation at the molecular level, by resolving the binding free energy profile and the resultant binding affinity. We focus on systems involving polyelectrolyte ligands with strong anionic charges. In that case, the inter-molecular interactions are more likely to be governed by electrostatics, while the hydrophobicity/hydrophilicity of the molecules and thus the influence of the solvents is of minor importance. These considerations motivate the development of computational tools, especially coarse-grained (CG) models delving deeper into the characterization of a generic ligand-receptor binding process. The ultimate goal of this thesis aims at mapping the binding affinity contributed by various interactions on the atomistic level, to some macroscopically observable quantities, or better expressed, the origin of the binding. With this in mind, the present thesis comprises the research goals as follows:

In **chapter 4**, we start with the LPE involved complexation with the LPE itself and human serum albumin (HSA). For the former case, PECs consisting of oppositely charged linear polymer chains have been studied for decades owing to their fundamental importance in biophysics and technological applications [42, 43]. Despite the extensive simulation works on PEC formation on a pair level, to the best of our knowledge, little attention has been given to the variation of the system's free energy and structures along the LPE pair association pathway. The previous simulation studies indicated very fast and cooperative association processes once the isolated LPE coils come into first contact [44, 45, 18]. A systematic exploration of the pair PMFs for different LPE charge densities, however, is still absent, as well as their quantitative description by a tractable theory. Also the nature of the transient states right at the onset of attraction and during complexation is not fully characterized, despite the need for a better understanding of PEC metastable states and preceding association kinetics, e.g., in gene delivery and therapy [46, 47, 48]. Therefore, the complex formation between two oppositely charged LPEs right at the onset of the association and the intermediate range before collapsing into the final state is the first research goal of the thesis. An extension of this study is made towards the interactions between the LPE and the protein. Despite of extensive studies being introduced [49], the previous emphasis was placed on the monopole electrostatic interactions. Relevant studies will be enriched here on the basis of the LPE modeling adopted before, with a particular focus on the counterions in the protein-LPE complexation.

In **chapter 5**, we move on from linear PEs to dendritic PEs (charged dendrimers). As we

introduced before, the research to the charged dendrimers has attracted strong interest due to their versatile bioapplications [36, 37, 38]. Somewhat surprisingly, however, it has been hardly attempted to consistently calculate the effective surface potential (and its location) of the charged dendrimer so far, despite its significance for electrostatic interactions. One reason could be that the identification of condensed counterions requires the definition of a cut-off region in space that contains condensed-types of ions distinct from those in the diffusive double layer, with highly varying definitions [50, 51, 52, 53, 54]. As a consequence, effective charges and the spatial delimitation of diffusive double-layer behavior have been inconsistently defined, hampering a meaningful comparison to analytical theory and experiments. This consequently impairs the future understanding of the interactions of charged dendrimers with biomolecules in general, in spite of their high biological importance. Driven by the urgent need to develop accurate modeling tools and the interpretation for the interactions between charged dendritic drugs that are predominantly of electrostatic nature, we investigate the dPGS with a particular focus on its electrostatic surface properties. With that, the dPGS effective radius and charge will be determined accordingly.

In **chapter 6**, we attack the key challenge of this thesis, that is to understand the polyelectrolyte ligands interacting with proteins. As we stressed in the introduction, the rational design of polymeric drugs and nanocarriers has become a central task in medicine and pharmacy in the recent years [55, 56, 57], and can be limiting to the desired biomedical application. The aim of this part is looking for a quantitative rationalization of the complexation of such substances with various proteins relevant for the pharmaceutical problem, which is to date hindered by a lack of molecular mechanistic insights, the promiscuity of the interactions and the possible cooperative effects [58]. We aim at a major step forward in understanding the interactions between charged dendrimers and various proteins, with a particular focus on the dPGS-selectin complexation which provides the basis for the dPGS as a potent anti-inflammatory drug [30, 59, 60].

3 Basic principles and methods

This chapter introduces the theoretical framework, simulation and experimental methods involved in this thesis. Specifically, we discuss the theoretical framework in section 3.1. An introduction to the simulations is presented in section 3.2. In addition to that, a few experiments are designed to verify and enrich the insights on the protein-polyelectrolyte complexation, with the relevant methods being introduced in section 3.3.

3.1 Theoretical description of macromolecular complexation

The effective pair interaction potential

We start with the system comprising one ligand and one receptor, composed of particle number N_{L} and N_{P}, respectively. They are solvated in N_{i} solvent and ion particles. The reaction coordinate in that case is taken as the ligand-receptor center-of-mass (COM) distance. The corresponding effective pair interaction potential between the ligand and receptor reads [61]

$$V(R) = -k_{\mathrm{B}}T \ln \left\{ A \int d\boldsymbol{r}^{N_{\mathrm{P}}+N_{\mathrm{L}}+N_{\mathrm{i}}} \exp\{-\beta V[\boldsymbol{r}_1 \dots \boldsymbol{r}_{N_{\mathrm{P}}+N_{\mathrm{L}}+N_{\mathrm{i}}}]\} \delta\left(\boldsymbol{R} - (\boldsymbol{r}^0_{\mathrm{L}} - \boldsymbol{r}^0_{\mathrm{P}})\right) \right\}. \tag{3.1}$$

Here, $\boldsymbol{r}_i$ denotes the coordination vector of the ith particle, and $\boldsymbol{r}^0_{\mathrm{L,P}} = (\sum_{i=1}^{N_{\mathrm{L,P}}} \boldsymbol{r}_i m_i)/(\sum_{i=1}^{N_{\mathrm{L,P}}} m_i)$ is the center of mass vector of the ligand and the receptor, respectively. We have used the shorthand notation $d\boldsymbol{r}^{N_{\mathrm{P}}+N_{\mathrm{L}}+N_{\mathrm{i}}}$ to denote $d\boldsymbol{r}_1 d\boldsymbol{r}_2 \cdots d\boldsymbol{r}_{N_{\mathrm{P}}+N_{\mathrm{L}}+N_{\mathrm{i}}}$. V denotes the potential energy with the coordinate configuration $\boldsymbol{r}_1 \dots \boldsymbol{r}_{N_{\mathrm{P}}+N_{\mathrm{L}}+N_{\mathrm{i}}}$. The ligand-receptor COM distance vector $\boldsymbol{R}$ is ensured by the delta function in Eq. (3.1). The normalization constant A can be chosen appropriately in order to satisfy the desired asymptotic behavior of $V(R)$ [61]. The binding free energy is equal to the difference of the potential between the bound and the unbound state as

$$\Delta G_b = V(r_b) - V(\infty), \tag{3.2}$$

where r_b corresponds to the reaction coordinate at the bound state. Note that ΔG_b is identical to the potential of mean force (PMF) of the binding process, that is, the work performed to force the system to move along the binding pathway from $R = \infty$ to $R = r_b$.

There are enthalpic and entropic components in ΔG_b. In particular, concerning the complexation dominated by electrostatics, the enthalpic component of ΔG_b can be partially captured by the Poisson-Boltzmann (PB) theory, which will be introduced in the following sections.

Electrostatics

Poisson-Boltzmann theory

In this section, we present a theoretical treatment of the PB equation, and discuss various approximations that enter into it. The general consideration starts from the Poisson equation, which determines the relation between the potential ϕ and the charge density ρ at any point $\mathbf{r}$ in presence of ions assumed to be mobile and in thermodynamic equilibrium, as [62]

$$\nabla^2\phi = -\frac{\rho(\mathbf{r})}{\epsilon_0\epsilon_r} = -\frac{e}{\epsilon_0\epsilon_r}[\sum_i z_+^i n_+^i(\mathbf{r}) + \sum_j z_-^j n_-^j(\mathbf{r})]. \tag{3.3}$$

Here, ϵ_0 is the permittivity of vacuum and ϵ_r is the relative permittivity of the medium. The local charge density $\rho(\mathbf{r})$ is a sum of particles number densities $n_\pm$ with charge valency $z_\pm$, whereas running superscripts i and j go over all the positive and negative charge species in the solution, respectively. Equation (3.3) is readily accessible to the electrostatic potential given the distribution of all ionic species. Moreover, given the mobile ions in thermodynamic equilibrium, their distribution in the mean-field level without any ion-ion correlations follows the Boltzmann distribution as

$$n_\pm^i(\mathbf{r}) = n_\pm^{i,0}\exp(-ez_\pm^i\phi(\mathbf{r})/k_\mathrm{B}T), \tag{3.4}$$

where $n_\pm^{i,0}$ is the bulk density of the ith charged species (with valency $z_\pm^i$), corresponding to the value at zero potential. Combining Eq. (3.3) with Eq. (3.4) finally leads to the PB equation reading [62]

$$\nabla^2\phi(\mathbf{r}) = -\frac{e}{\epsilon_0\epsilon_r}\{\sum_i n_+^{i,0}z_+^i\exp(-ez_+^i\phi(r)/k_\mathrm{B}T) + \sum_j n_-^{j,0}z_-^j\exp(-ez_-^j\phi(r)/k_\mathrm{B}T)\}. \tag{3.5}$$

The nonlinear essence of the PB equation prohibits solutions in closed analytical forms. We therefore rely on approximations of some simple boundary conditions. Concerning more general cases, the solution of the PB equation resorts to numerical approaches. In addition to that, the ions under consideration are deemed as charged point particles. The absence

of the ion specific interactions can probably lead to unrealistic high ion condensation at the charged interface, consequently the electrostatic screening induced by ions is overestimated especially for the highly charged surface. The errors of the PB theory may also arise from the exclusion of the electrostatic correlation among ions and other interactions not included in PB. Hence, the PB equation is most appropriate for approximating the electrostatic potential at the surface in the presence of monovalent salts at concentrations smaller than 0.2 M and potentials not exceeding 50-80 mV [63]. For instance, the PB equation describes rather well the ionic distributions in physiological conditions (electrolyte strength of about 0.1 M) [62].

Deybe-Hückel theory and Yukawa potential

In case of low surface potential ϕ and symmetric ions, the exponential terms in Eq. (3.5) can be linearized in terms of the potential ϕ, which gives the Deybe-Hückel (DH) theory or the linearized Poisson Boltzmann (LPB) equation

$$\nabla^2\phi(\mathbf{r}) = \frac{e^2}{\epsilon_0\epsilon_r k_\mathrm{B}T}\left(\sum_i n_+^{i,0}(z_+^i)^2 + \sum_j n_-^{j,0}(z_-^j)^2\right)\phi(\mathbf{r}). \tag{3.6}$$

In case of symmetric monovalent ions, a compact form of the above equation follows

$$\nabla^2\phi(\mathbf{r}) = \kappa^2\phi(\mathbf{r}), \tag{3.7}$$

where $\kappa = \sqrt{8\pi n_0 l_\mathrm{B}}$ is the inverse Deybe length with n_0 being the density of the ions in bulk solution and $l_\mathrm{B} = e^2/4\pi\epsilon_0\epsilon_r k_\mathrm{B}T$ the Bjerrum length. $l_\mathrm{B} = 0.7$ nm holds at room temperature ($T = 300$ K) and in the aqueous phase. In view of a simple homogeneously charged sphere with net charge valency Z, radius R and with the boundary condition [64]

$$\epsilon_r \frac{d\phi(r)}{dr}\bigg|_{r=R} = -\frac{Ze}{4\pi\epsilon_0 R^2}, \quad \phi(r)|_{r\to\infty} = 0, \tag{3.8}$$

the solution of Eq. (3.7) leads to the famous Yukawa potential

$$e\beta\phi_\mathrm{DH} = Z l_\mathrm{B}\frac{\exp(\kappa R)}{1+\kappa R}\frac{\exp(-\kappa r)}{r}. \tag{3.9}$$

Concerning its functional form, the factor $1/r$ accounts for the Coulombic decay, whereas the ion screening is represented by factor $\exp(-\kappa r)$. $Z\exp(\kappa R)/(1+\kappa R)$ can be regarded as the effective charge of the charged sphere. The DH theory is in absence of any nonlinear effects near the surface and thus is valid only in case of a weakly charged sphere. The DH or PB theory can be advanced to fit more realistic systems. For instance, substituting in

Eq. (3.6) with asymmetric charge distributions leads to the electrostatic potential stemming from molecules with multipoles [65]. The inclusion of ion specific interactions even push the framework beyond standard PB theory [66].

Intermolecular interactions

The intermolecular electrostatic interaction, U_{el}, between two charged spheres (with valencies Z_1 and Z_2, radii R_1 and R_2), can be obtained from the electrostatic energy of the second sphere with the effective charge $Z_2\exp(\kappa R_2)/(1+\kappa R_2)$ in the potential $\phi_{\mathrm{DH},1}$ of the first sphere

$$U_{\mathrm{el}} = \phi_{\mathrm{DH},1} Z_2 \frac{\exp(\kappa R_2)}{1+\kappa R_2}. \tag{3.10}$$

The expression of $\phi_{\mathrm{DH},1}$ refers to the Yukawa potential Eq. 3.9. The charge of the second sphere is seen to be concentrated at its center, which leads to the well-known screened-Coulomb interaction energy [62]

$$\beta U_{\mathrm{el}} = Z_1 Z_2 l_{\mathrm{B}} \frac{\exp[\kappa(R_1+R_2)]}{(1+\kappa R_1)(1+\kappa R_2)} \frac{\exp(-\kappa r)}{r}, \tag{3.11}$$

where r denotes the intermolecular distance. In particular, at distance $r = R_1+R_2$, Eq. (3.11) readily provides an estimate of the intermolecular electrostatic binding energy,

$$\beta U_{\mathrm{el,b}} = \frac{Z_1 Z_2 l_{\mathrm{B}}}{(1+\kappa R_1)(1+\kappa R_2)(R_1+R_2)}. \tag{3.12}$$

Again, Eq. (3.12) is based on the framework of the DH theory, which completely neglects nonlinear effects present for charged molecules. In addition, Eq. (3.12) is derived on the hard sphere approximation. Thus, the deformations at the binding interface and altering of the salt bridges and hydrogen bonds upon complexation are not included.

Hamaker interactions

As short-ranged non-bonded interactions, Van der Waals (vdW) forces play a crucial role in all phenomena involving intermolecular forces. For pairwise macromolecules with radii R_1 and R_2 at small separation distances, the vdW interacting free energy can be calculated by summing up the vdW potentials of the form $\sim -C/r^6$ individually for all atomistic pairs [67] as

$$U_{\mathrm{vdW}} = -\frac{A}{6r}\frac{R_1 R_2}{R_1+R_2}, \tag{3.13}$$

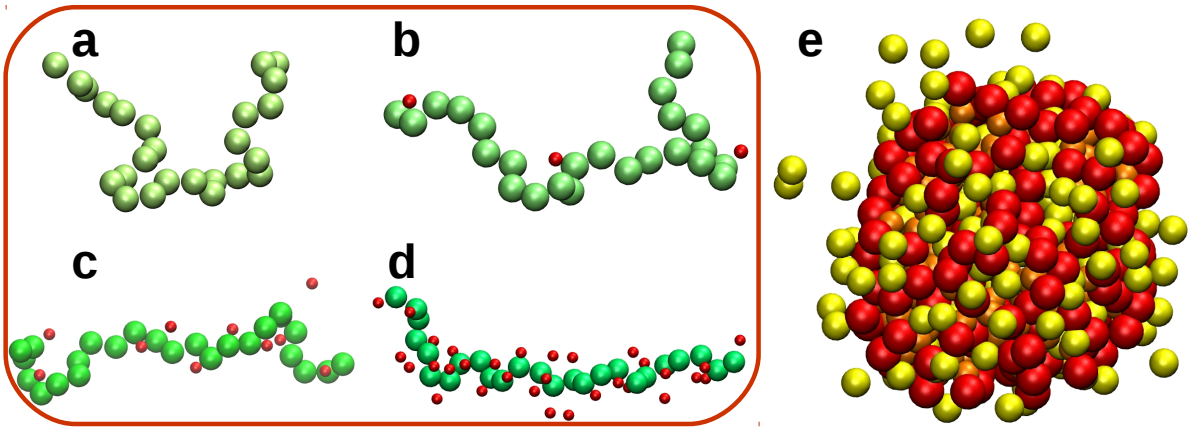

Figure 3.1: Snapshots of condensed counterions presented at various modeled systems. Panel (a-d) exhibits the polyelectrolyte modeled in CG fashion with salt concentration $c = 20$ mM and with Manning parameter $\xi = 0.29, 0.87, 1.73$ and 3.5, respectively. Every segment of the polyelectrolyte is positively charged labeled with green color, whereas the anions are of an opposite charge -1 e, depicted with red spheres. Only the condensed anions are presented here, revealing a number increase from low to high ξ. In parallel to that, the polyelectrolyte gets progressively prolonged at higher ξ, in response to a stronger repulsion from the intra-chain electrostatics. In panel (e), the G5-dPGS in CG representation is shown, with red and orange beads corresponding to negatively charged and neutral CG segments, respectively. The condensed counterions in that case are depicted in orange.

where r is the intermolecular distance and A is the Hamaker constant reading

$$A = \pi^2 C \rho_1 \rho_2. \tag{3.14}$$

Equation (3.14) contains $\rho_{1,2}$, the atom number density of the individual macromolecule. The value of A relies on a specific system, however, for proteins in aqueous solution the experimental values A fortunately shows small variations as $A \sim 3-10\ k_{\mathrm{B}}T$ [68]. With that, combining Eq. (3.11) with Eq. (3.13), a simple addition of the electrostatic interactions at the LPB level and the vdW contributions leads to the traditional Derjaguin-Verwey-Landau-Overbeek (DLVO) [69, 70, 71] interaction as

$$U_{\mathrm{D}} = U_{\mathrm{el}} + U_{\mathrm{vdW}}. \tag{3.15}$$

As a dispersion stabilizing theory, Eq. (3.15) is useful to explain the colloidal stability and adsorption dominated by vdW and Coulombic forces. Apparently, the additivity of these two while leaving out the underlying correlations does not always hold. Besides, more complicated means, for instance, the deformations of the molecular structure upon complexation are omitted in the current framework.

Counterion condensation and Charge renormalization

In vicinity of the charged surface, a number of ions condense at the surface due to the electrostatic attraction. These ions comprising mostly the oppositely charged counterions, form the so called "diffuse layer", which contributes substantially to electrostatic screening. Near the surface, the strong ion-ion correlation and non-linear effects triggered by this diffuse layer break down the LPB approach. These effects die out in the far field, which make the LPB equation applicable again, and consequently the electrostatic field decays to the Yukawa potential. Importantly, the sphere charge valency entering Eq. (3.9) serves as the renormalized (termed also as effective) charge. In other words, the bare charge on the surface is reduced from its actual value because of "binding" of oppositely charged counterions.

Condensation on polyions: Manning condensation

Concerning an infinitely long cylinder of radius r_0 and line charge density $\lambda > 0$ enclosed in a cylindrical cell of radius R, the corresponding PB equation (Eq. (3.5)) can be written as

$$\left(\frac{d^2}{dr^2} + \frac{1}{r}\frac{d}{dr}\right) y(r) = \kappa^2 \exp\{y(r)\}, \tag{3.16}$$

where $y(r) = e\beta\phi(r)$ denotes the dimensionless potential of the charged cylinder and r labels the radial distance from the cylinder axis. In the presence of the boundary condition of the isolated cylinder

$$dy(r_0)/dr = -2\xi/r_0, \;\; dy(R)/dr = 0. \tag{3.17}$$

Here, we define ξ as the Manning parameter as

$$\xi = |z_\pm| l_\mathrm{B} (\lambda/e), \tag{3.18}$$

where $|z_\pm|$ stands for the counterion valency. Equation (3.16) possesses the analytical solution [72, 73, 74, 75]

$$y(r) = -2 \ln \left\{ \frac{r}{R} \sqrt{1+\gamma^{-2}} \cos\left(\gamma \ln \frac{r}{R_\mathrm{M}}\right)\right\}. \tag{3.19}$$

With that, the counterion density can be expressed with a Boltzmann factor as $n(r) = n(R)\exp\{y(r)\}$, where $n(R)$ is the counterion bulk density. This follows the normalized

total charge density, $\lambda_t(r)/\lambda$, within a cylinder of radius $r \in [r_0, R]$ as

$$\lambda_r(r)/\lambda = 1 - \frac{1}{\lambda}\int_{r_0}^{r} en(r)2\pi r dr = 1 - (1 - \frac{1}{\xi}) - \frac{\gamma}{\xi}\tan\left(\gamma \ln \frac{r}{R_{\mathrm{M}}}\right). \tag{3.20}$$

Equation (3.20) has two limits, $\lambda_r = \lambda$ for $r = r_0$, and $\lambda_r = 0$ for $r = R$. In particular, γ and R_{M} (known also as the Manning radius) presented in Eq. (3.19) and (3.20) are parameters as a transcendental function of ξ, r_0 and R. A numerical calculation demonstrates that R_{M} exceeds r_0 only when $\xi > \xi_{\mathrm{min}}$. As the concentration of the charged cylinder is infinitly dilute, *i.e.*, in condition of $R \to \infty$ and $r_0 \to 0$, ξ_{min} simply goes to 1. Hence, the Manning radius R_M is larger than the charged cylinder only if $\xi > 1$. In that case, the fraction extent θ of the charge neutralization by condensed counterions within R_{M} turns out to be $\theta = 1 - 1/\xi$. The above discussions constitute the essence of the celebrated Manning–Oosawa counterion condensation [76, 77, 78, 79, 80, 81].

The conventional model for ion distribution in the diffusive double layer is based on a cylindrical cell model with the polyion chain placed at the center [82, 83]. According to the Manning theory, counterion condensation occurs if $\xi > 1$, i.e., if the Manning parameter exceeds unity. When $\xi > 1$, the analysis towards Eq. (3.20) predicts a fraction $\theta = 1 - 1/\xi$ of counterions in the condensed state. If the polymer backbone is treated as a cylinder, the effective, renormalized charge density of such a cylinder with $\xi > 1$ for monovalent counterions is then

$$\lambda_r = e/l_{\mathrm{B}}, \tag{3.21}$$

The cell model provides simple expressions for the condensation threshold radius r_0, the Manning parameter ξ, and the fraction θ of condensed counterions [84]. It predicts that the fraction θ of condensed ions is independent of the cell size [85, 78, 79, 80]. When $\xi < 1$, as we demonstrated before, counterion condensation does not occur and the polyion bare charge and the effective charge are the same.

Manning's condensation theory is elegantly simple, which has won broad research interests [86]. However, the polymer under Manning's consideration is approximated as a straight rod with negligible radius and is immersed in infinite dilute solution. Thus, although Manning condensation is at least qualitatively supported by some experimental work [87, 88], it is still highly controversial in the PE research community [89, 90, 91, 92, 93]. On one hand, most polymers involved in experiments and industry are very flexible. On the other hand, the state of condensed counterions is not well understood. The mobile counterions in the bound state could add important corrections to the Manning theory.

Electrostatic interactions with renormalized charge

As we previously stressed, the LPB description on the molecular electrostatic field breaks down in the vicinity of the surface in the presence of the counterion condensation. However, the successful application of the Manning theory on polyelectrolytes indicates that the counterion condensation can be explicitly included in the concept of its effective charge. On that basis, given pairwise spherical molecules immersed in a solution, the corresponding interacting free energy by referring to Eq. (3.11) can be formulated as

$$\beta U_{\mathrm{el}} = Z_1(1-\theta_1)Z_2(1-\theta_2)l_{\mathrm{B}}\frac{\exp[\kappa(R_1+R_2)]}{(1+\kappa R_1)(1+\kappa R_2)}\frac{\exp(-\kappa r)}{r}. \tag{3.22}$$

Equation (3.22) is essentially still an outcome of the LPB equation. Yet, the complicated many body and nonlinear effects via condensed counterions are effectively captured by θ_1 and θ_2, which denote the fraction extent of charge neutralization for the sphere 1 and 2, respectively. Similar to the Manning's pioneered work on polyelectrolytes, theoretical predictions of θ has been proposed for charged spheres [94, 95, 96, 97]. However, these attempts equally suffer from the drawbacks we discussed for the Manning theory. The investigation of a proper formulation on θ for spherical molecules constitutes an important research goal of this thesis.

The entropical terms for macromolecule complexation

Entropical terms contribute to complexation

Possible entropy changes that contribute to complexation stem from various sources. A typical example is the decrease of the ligand translational entropy $\Delta S_{\mathrm{trans}}$ upon complexation resulting in the free energy loss $-k_{\mathrm{B}}T\Delta S_{\mathrm{trans}}$. Another important factor corresponds to the receptor-ligand binding interface. That is, as the complexation takes place, a certain amount of the entropy cost can be triggered, as a loss of the degree of freedom of the molecular terminal groups, and as dendrimers restructure themselves to stretch or squeeze into/onto the ligand surface [98]. The restructure of the receptor-ligand interface could moreover give rise to a number of released molecules. For instance, a couple of water molecules due to the broken hydrogen bonds or a few counterions via the loss of the ionic pairings. As a result, the releasing entropy, proportional to the released particle number, could significantly drive the binding process, a statement firstly proposed from studying the protein-brush interactions [99]. In the following, we will discuss the Record-Lohman analysis [100], serving as a practical tool to identify the counterion release. The formulation of the released entropy is given via the counterion release model discussed in the following.

Record-Lohman analysis

Concerning the association process of the ligand (B) and the protein (C) converted to the non-covalent complex BC, but with a few released particles (A) (counterions or water molecules for instance), the reaction is

$$\mathrm{B} + \mathrm{C} \rightleftarrows \mathrm{BC} + N_{\mathrm{CR}}\mathrm{A}. \tag{3.23}$$

Let us assume the chemical activity of the ligand, the protein, the complex and the released particle as α_{B}, α_{C} α_{BC} and α_{A}, respectively. N_{CR} denotes the number of the released particles. The binding constant then can be expressed as [100]

$$K_{\mathrm{ABC}} = \frac{\alpha_{\mathrm{BC}}\alpha_{\mathrm{A}}^{N_{\mathrm{CR}}}}{\alpha_{\mathrm{B}}\alpha_{\mathrm{C}}}. \tag{3.24}$$

Recall $\epsilon = -k_{\mathrm{B}}T\ln K$ the definition of the binding constant, the binding free energy ϵ_{ABC} of the above reaction can be written as

$$\epsilon_{\mathrm{ABC}} = \epsilon_{\mathrm{BC}} - N_{\mathrm{CR}}k_{\mathrm{B}}T\ln(\alpha_{\mathrm{A}}). \tag{3.25}$$

Here, $\epsilon_{\mathrm{BC}} = -k_{\mathrm{B}}T\ln(\alpha_{\mathrm{BC}}/\alpha_{\mathrm{B}}\alpha_{\mathrm{C}})$ refers to the binding free energy for the conversion of B and C in absence of the released particle A. In case of ϵ_{BC} much smaller than ϵ_{ABC}, the differentiation of $\ln K_{\mathrm{ABC}}$ with respect to $\ln\alpha_{\mathrm{A}}$ follows with [100]

$$\frac{d\ln K_{\mathrm{app}}}{d\ln\alpha_{\mathrm{A}}} = N_{\mathrm{CR}}. \tag{3.26}$$

This primary analysis reveals the way to connect the binding affinity K_{app} with the stoichiometric coefficient N_{CR}, adopted by the pioneering work of Record-Lohman [100]. In terms of the counterion-release interactions, the adoption of Eq. (3.26) may indicate the dominant role of the counterion release, which has been discussed in the context of the protein-DNA binding reaction [100], biological macroion association in a solution [101], assembly of polyelectrolyte-surfactant complexes [102] and so on. In the following section, we will construct a minimal model in the canonical ensemble which comprises both the enthalpic and entropic changes of the system upon complexation. With that, we will show the Record-Lohman analysis essentially originates from the entropic change due to a few released counterions via binding. Moreover, this model initializes the idea of the Langmuir adsorption isotherm that will be elaborated later.

Counterion release model

Given the canonical ensemble of ideal gases with the particle number N, the free energy of the system is

$$\beta F = N\left[\ln\left(\frac{N}{V}\Lambda^3\right) - 1\right]. \tag{3.27}$$

Here, V is the box size and Λ is defined as the cubed thermal (de Broglie) wavelength. Now, we assume this is a three-component system consisting of particle type A, B and C, with number N_A, N_B, and N_C, respectively. The complexation can happen between A and B, forming AB complex with concentration $[\mathrm{AB}] = N_\mathrm{AB}/V$, or between B and C forming BC with concentration $[\mathrm{BC}] = N_\mathrm{BC}/V$. As compared to the reaction considered for the Record-Lohman analysis, particle A can be understood as counterions or water molecules, which can be bound with particle B in a solution, and get released after the complexation between the complex AB and the particle C. Without loss of generality, $N_\mathrm{CR} = 1$ is set here, namely, only 1 particle is released per reaction. The complexation brings products AB and BC in a solution, with number N_AB and N_BC, respectively. As a result, the residual unbound A, B and C particle number is $N_\mathrm{A} - N_\mathrm{AB}$, $N_\mathrm{B} - N_\mathrm{BC} - N_\mathrm{AB}$ and $N_\mathrm{C} - N_\mathrm{BC}$, respectively. The complex and unbound particles are individually approximated as ideal gases. Summing up the free energy of each component formulated by Eq. 3.27 gives rise to

$$\begin{aligned}
\beta F^\mathrm{id} = {} & (N_\mathrm{A} - N_\mathrm{AB})\left[\ln\left(\frac{N_\mathrm{A} - N_\mathrm{AB}}{V}\Lambda^3\right) - 1\right] \\
& + (N_\mathrm{B} - N_\mathrm{BC} - N_\mathrm{AB})\left[\ln\left(\frac{N_\mathrm{B} - N_\mathrm{AB} - N_\mathrm{BC}}{V}\Lambda^3\right) - 1\right] \\
& + (N_\mathrm{C} - N_\mathrm{BC})\left[\ln\left(\frac{N_\mathrm{C} - N_\mathrm{BC}}{V}\Lambda^3\right) - 1\right] \\
& + N_\mathrm{AB}\left[\ln\left(\frac{N_\mathrm{AB}}{V}\Lambda^3\right) - 1\right] + N_\mathrm{BC}\left[\ln\left(\frac{N_\mathrm{BC}}{V}\Lambda^3\right) - 1\right].
\end{aligned} \tag{3.28}$$

Moreover, the A-B and B-C complexation contributes the binding energy ϵ_AB and ϵ_BC per complex, which leads to the overall complexation energy

$$\beta F^\mathrm{comp} = N_\mathrm{AB}\beta\epsilon_\mathrm{AB} + N_\mathrm{BC}\beta\epsilon_\mathrm{BC}. \tag{3.29}$$

Lastly, we account the free energy

$$\beta F^\mathrm{id,b} = N_\mathrm{AB}\ln\frac{\Lambda^3}{v_0^\mathrm{AB}} + N_\mathrm{BC}\ln\frac{\Lambda^3}{v_0^\mathrm{BC}}, \tag{3.30}$$

for the ligand locked into the accessible volume $v_0^{\mathrm{AB/BC}}$ of the complex AB/BC in the bound state. The total free energy of the system is thus the summation

$$F = F^{\mathrm{id}} + F^{\mathrm{comp}} + F^{\mathrm{id,b}} \tag{3.31}$$

of the above three terms. In equilibrium, minimization with respect to the N_{AB} and N_{BC},

$$\left.\frac{\partial F}{\partial N_{\mathrm{AB}}}\right|_{N_{\mathrm{BC}}} = 0, \quad \left.\frac{\partial F}{\partial N_{\mathrm{BC}}}\right|_{N_{\mathrm{AB}}} = 0 \tag{3.32}$$

leads to

$$K_{\mathrm{AB}} = v_0^{\mathrm{AB}} \exp(-\beta\epsilon_{\mathrm{AB}}) = \frac{[\mathrm{AB}]}{[\mathrm{A}][\mathrm{B}]}, \quad K_{\mathrm{BC}} = v_0^{\mathrm{BC}} \exp(-\beta\epsilon_{\mathrm{BC}}) = \frac{[\mathrm{BC}]}{[\mathrm{B}][\mathrm{C}]}. \tag{3.33}$$

with

$$\begin{aligned} [\mathrm{A}] &= (N_{\mathrm{A}} - N_{\mathrm{AB}})/V, \\ [\mathrm{B}] &= (N_{\mathrm{B}} - N_{\mathrm{AB}} - N_{\mathrm{BC}})/V, \\ [\mathrm{C}] &= (N_{\mathrm{C}} - N_{\mathrm{BC}})/V, \end{aligned} \tag{3.34}$$

being the concentrations of unbound A, B, and C particles, respectively.

We assume, the complex AB can be formed as a result of ionization of ligand B. Consequently, in the thermodynamic equilibrium we end up with a mixture of the unbound ligand B and the complex AB, that is

$$[\mathrm{B}]_{\mathrm{exp}} = [\mathrm{B}] + [\mathrm{AB}]. \tag{3.35}$$

As a result, the binding constant expresses as

$$\begin{aligned} K_{\mathrm{BC}}^{\mathrm{exp}} &= \frac{[\mathrm{BC}]}{[\mathrm{B}]_{\mathrm{exp}}[\mathrm{C}]} = \frac{[\mathrm{BC}]}{([\mathrm{B}] + [\mathrm{AB}])[\mathrm{C}]} \\ &= \frac{[\mathrm{BC}]}{[\mathrm{B}][\mathrm{C}]} \frac{1}{1 + K_{\mathrm{AB}}[\mathrm{A}]} = \frac{K_{\mathrm{BC}}}{1 + K_{\mathrm{AB}}[\mathrm{A}]}. \end{aligned} \tag{3.36}$$

In case the ion condensation is notable, that is when $K_{\mathrm{AB}}[\mathrm{A}] \gg 1$, we have

$$K_{\mathrm{BC}}^{\mathrm{exp}} \approx K_{\mathrm{BC}} - K_{\mathrm{AB}} - \ln([\mathrm{A}]). \tag{3.37}$$

Applying logarithm to both side of Eq. (3.37) leads to

$$\epsilon_{\mathrm{BC}}^{\mathrm{exp}} = \epsilon_{\mathrm{BC}} - \epsilon_{\mathrm{AB}} - k_{\mathrm{B}}T \ln\left(\frac{1}{v_0^{\mathrm{AB}}[\mathrm{A}]}\right). \tag{3.38}$$

The interpretation of Eq. (3.38) is twofold. First, the binding free energy measured by experiment deviates from ϵ_{BC}, by an offset of "-ϵ_{AB}", which arises from the ionization between A and B. Second, the condensed ions become liberated after the formation of the complex BC, resulting in the contribution $-k_{\mathrm{B}}T \ln\left(\frac{1}{v_0^{\mathrm{AB}}[\mathrm{A}]}\right)$, which indeed leads to the ion releasing entropy. Given the condensed ions concentration $c_{\mathrm{A}}^{\mathrm{b}} = 1/v_0^{\mathrm{AB}}$ in the bound state, and $c_{\mathrm{A}}^{\mathrm{unb}} = [\mathrm{A}]$ in the unbound state, releasing entropy ΔS_{CR} per released ion can be expressed as

$$\Delta S_{\mathrm{CR}} = k_{\mathrm{B}} \ln\left(\frac{c_{\mathrm{A}}^{\mathrm{b}}}{c_{\mathrm{A}}^{\mathrm{unb}}}\right). \tag{3.39}$$

In case the binding process is dominated by N_{CR} released ions, the overall binding free energy scales as $\epsilon_{\mathrm{BC}}^{\mathrm{exp}} = -k_{\mathrm{B}}TN_{\mathrm{CR}}\Delta S_{\mathrm{CR}}$, leading to the relation of the binding constant versus the salt concentration $c_{\mathrm{A}}^{\mathrm{unb}}$ as

$$\frac{dK_{\mathrm{BC}}^{\mathrm{exp}}}{d\ln c_{\mathrm{A}}^{\mathrm{unb}}} = -N_{\mathrm{CR}}. \tag{3.40}$$

This formula agrees with Eq. (3.26) according to the Record-Lohman analysis, which is used as a practical analysis in the experiment to examine the number of released counterions in case the complexation is dominated by the counterion release effect.

Concluding remarks on theoretical methods

To conclude, we aim at formulating the binding free energy ΔU between a pair of charged molecules in a solution. The interactions between two molecules are considered as DLVO type, which leads to ΔU as a superposition of the electrostatic part U_{el} and the van der Waals interaction U_{vdw}. For the electrostatic part, the molecules are represented by their effective charge given the charge renormalization via condensed counterions. These condensed counterions might result in an amount of released entropy, which contributes to the binding free energy. However, the applicability of the above theoretical framework is still limited. For one hand, U_{el} is formulated in the presence of two ideal spheres and accounts only the monopole term. As a result, it does not apply, for instance, to proteins which possess irregular shapes and asymmetric charge distributions. On the other hand, the counterion release is essentially of electrostatic origin, which means the releasing entropy ΔS_{CR} and U_{el} are

inevitably correlated. Hence, errors may arise from the simple assumption of additivity of ΔS_{CR} and U_{el}.

3.2 Molecular and stochastic simulations

Basic principles

The polymer or dendrimer in our study is composed of a large number of atoms, which individually obeys the Newton's second law of motion

$$m_i \frac{\boldsymbol{v}_i}{dt} = \boldsymbol{F}_i, \tag{3.41}$$

where $m_i, \boldsymbol{v}_i, \boldsymbol{F}_i$ denote the mass, velocity, acting force on the atom i, respectively. The atomistic trajectory by integrating Eq. (3.41) can be numerically found through a molecular dynamics (MD) computer simulation, which takes the individual atomistic motion into account while also respecting the strong correlation between bonded or non-bonded atoms. On the other hand, the design of a computer simulation should consider the available computational power. In practice, the MD simulating box consists of many solvent molecules. Yet our central interest is the polymer or dendrimer solutes. In that case, the Langevin dynamics (also termed as stochastic dynamics (SD)) appears as an alternative, that is to model the solvent by a dielectric background continuum with its viscous aspect remained. The corresponding simulation is based on the Langevin's equation of motion

$$m_i \frac{d^2 \boldsymbol{r}_i}{dt^2} = -m_i \xi_i \frac{d\boldsymbol{r}_i}{dt} - \boldsymbol{\nabla}_i U + \boldsymbol{R}_i(t) \tag{3.42}$$

where ξ_i is the relaxation rate of the ith segment. U is the system potential energy, which includes harmonic bonded interactions between neighboring segments, dihedral potentials and inter-atomic Lennard-Jones (LJ) between all non-neighboring segments. The force $\boldsymbol{R}_i(t)$ is a time dependent Gaussian noise process that mimics the solvent impacts and satisfies the fluctuation-dissipation theorem

$$\langle \boldsymbol{R}_i(t) \cdot \boldsymbol{R}_j(t') \rangle = 2 m_i \xi_i k_B T \delta(t - t') \delta_{ij}. \tag{3.43}$$

Note that the solvent in Langevin dynamics is modeled as a continuous medium, thus the electrostatic interaction should be scaled with static dielectric constant ϵ_r.

Simulation techniques

Particle Mesh Ewald

Long-range interactions, for instance electrostatics, are present in most biological processes, which require a lot of computational power for simulations. The calculation gets further complicated in combination with the periodic boundary condition (PBC), corresponding to the Coulomb interaction energy

$$\beta U_{\mathrm{Coul}} = l_{\mathrm{B}} \sum_{n=-\infty}^{\infty} \sum_{i=1}^{N} \sum_{j=1, j\neq i}^{\mathrm{N}} \sum_{k=1}^{3} \frac{Q_i Q_j}{|\boldsymbol{r}_i - (\boldsymbol{r}_j + n\boldsymbol{L}_k)|}. \tag{3.44}$$

The system in this case is interpreted as a single cubic simulation cell with length L and particle number N surrounded by an infinite number n of identical copies of the simulation cell. $\boldsymbol{r}_i$ denotes the coordination vector for the atom i and $\boldsymbol{L}_k$ refers to the length vector pointing to one of the all 3 directions. In that regard, the immediate challenge comes from the convergence of the series. After summing over a large number of cells, there is always a finite contribution. Even in Fourier space, the convergence problem remains due to an infinite number of terms of the delta-like charges.

The essential idea of the Ewald summation [103, 104] is to decompose U_{Coul} into the calculations of the short-range and long-range terms, by introducing a window function $W(r)$ which is 1 for small r and falls rapidly to zero for large r. The particular choice of the window function for the Ewald summation is the complementary error function $W(r) = 1 - \frac{2}{\sqrt{\pi}} \int_0^r e^{-t^2} dt$. This ensures a real-space calculation of $W(r)U_{\mathrm{Coul}}$, which rapidly converges to zero, and a Fourier-space mapping for $(1 - W(r))U_{\mathrm{Coul}}$ that can be represented by only a few terms. Further improvement is the use of Particle Mesh method combined with the Ewald summation, which converts the system of particles into a grid of density values before the Fast Fourier Transform (FFT). The computational time for the Particle Mesh Ewald (PME) method [105] scales as $N \log N$ over N^2 for Ewald summation.

Constant temperature

Concerning a canonical ensemble, the simulation box is imaginatively coupled with an external heat bath with given temperature T. An immediate idea to realize this is to rescale the particle velocity with a factor $\lambda = \sqrt{T/T_i}$, where T_i is the instantaneous temperature calculated after every time step. To do this, one needs to pay the price of losing the fluctuations of the kinetic energy, which usually ends up with incorrect sampling and kinetic energy. One realistic approach is the Berendsen thermostat [106], possessing the time constant τ_t,

that progressively dissipates the energy. The constant τ_t appears in the exponential decay of the temperature deviation, depending on the coupling strength between the system and the external heat bath. A more advanced method is to combine an extra stochastic term with the Berendsen thermostat. The corresponding velocity rescaling thermostat [107] correctly resolves the kinetic energy distribution, which is adopted to all the NVT ensemble simulations in this thesis.

Constant pressure

In the same sprite as the temperature coupling, constant pressure is maintained by coupling the system to a "pressure bath". Instead of manipulating the particle velocity, the constant pressure is maintained via Berendsen barostat [108] by scaling the box length in each dimension with a factor μ, where μ serves as a function of the instantaneous pressure of the system and the characteristic time scale τ_p. The Berendsen barostat can freely adjust the coupling strength by tuning τ_p, albeit the fluctuations in pressure or volume can not be faithfully realized. In cases where those fluctuations are important, the Parrinello-Rahman approach [109, 110] is used to produce the true NPT ensemble. This algorithm is analogous to the Nosé-Hoover barostat [111], but with the extension by making each unit vector of the unit-cell independent, and thus gives control of stress as well as pressure [109].

Potential of mean force calculations

To obtain the PMF between the ligand and receptor, we use steered Langevin Dynamics (SLD) simulations with the 'pull-code' as implemented in GROMACS [112]. The distance r between the centers-of-mass (COM) of the two molecules serves as the reaction coordinate, which is constrained by an external harmonic potential. The fictitious potential is time-dependent such that it exerts a pulling force to steer the molecule moving in a prescribed direction with a prescribed velocity v_p.

A variety of steering velocities have been empirically tested to make sure that the drift is slow enough to sample the equilibrium state, i.e., the simulation results are independent of the choice of v_p. For all results reported in this thesis, the steering velocity $v_p = 0.2\,\mathrm{nm/ns}$ is used along with the harmonic force constant $K = 2500\ \mathrm{kJ\ mol^{-1}\,nm^{-2}}$. During the simulation, we steer the constrained ligand approaching the receptor from a well separated state to the the final state. The friction force $f_f = -m\xi_i v_p$ is subtracted from the constraining force and the result is averaged within a specific interval of the discrete spacing Δr to obtain the mean force of the interaction potential. After that the PMF profile is acquired with a backward integration. Since the molecule is radially constrained in a three-dimensional

space, we need to subtract the center-of-mass translational entropy [113, 114, 115, 78]

$$G(r) = G^I(r) + (D-1)k_{\mathrm{B}}T\ln r, \tag{3.45}$$

where $G^I(r)$ is the integrated mean force and $D = 3$ is the dimensionality of the external constraint. With that, the system binding affinity can then be defined as the free energy value at the global minimum $r = r_b$ of the PMF in the stable complex as

$$\Delta G = G(r_b) - G(\infty), \tag{3.46}$$

where the reference $G(\infty)$ is set to zero.

Analysis of the simulation

Molecular radius of gyration and asphericity

The size of the molecule at study can be characterized by the radius of gyration R_g, which is defined as the trace of the gyration tensor ($\mathbf{R}^2$) [116]

$$\mathbf{R}_{\alpha,\beta}{}^2 = \frac{1}{N_{\mathrm{dP}}}\sum_{i=1}^{N_{\mathrm{dP}}}(\mathbf{r}_\alpha^i - \mathbf{r}_\alpha^M)(\mathbf{r}_\beta^i - \mathbf{r}_\beta^M), \quad \alpha,\beta = x,y,z, \tag{3.47}$$

where $\mathbf{r}_\alpha^i$ is the coordinate of the ith segment, N_{p} is the number of the molecular segments and $\mathbf{r}_\alpha^M$ is the COM position of the molecule along the α direction. The square of the radius of gyration is then

$$R_g{}^2 = \langle \mathrm{tr}(\mathbf{R}^2)\rangle = \langle \sum_{i=1}^{3} \lambda_i{}^2\rangle, \tag{3.48}$$

where $\lambda_i{}^2$ is the ith eigenvalue of the gyration tensor, representing the characteristic length of the equivalent ellipsoid that mimics the molecule. $\langle\cdots\rangle$ stands for the ensemble average. The degree of asphericity A of the molecule is defined in terms of the eigenvalue $\lambda_i{}^2$, which can be written as

$$A = \frac{\langle (T_r^2 - 3M)\rangle}{\langle T_r^2\rangle}, \tag{3.49}$$

with $T_r = \lambda_1{}^2 + \lambda_2{}^2 + \lambda_3{}^2$ and $M = \lambda_1{}^2\lambda_2{}^2 + \lambda_2{}^2\lambda_3{}^2 + \lambda_1{}^2\lambda_3{}^2$. Fot a perfect sphere A equals 0, whereas $A = 1$ corresponds to the extreme of an infinitely thin rod.

The radial electrostatic potential

We integrate Poisson's equation, Eq. (3.3), by numerically feeding the results $\rho_i(r)$ generated from simulations to obtain the local electrostatic potential $\phi(r)$. $\rho_i(r)$ composes of $\rho_+(r)$, $\rho_-(r)$, and $\rho_C(r)$ the distance–resolved radial density profiles for all charged species, namely, cations, anions and molecular segments that are individually with charge valency z_C, respectively. In addition to the potential profile, the running coordination number of charged beads of type $i = \pm, C$ can be calculated:

$$N_i(r) = \int_0^r \rho_i(s) 4\pi s^2 ds. \tag{3.50}$$

$N_i(r)$ explicitly represents the number of cations, anions, and charged molecular segments located within a distance r from the original point, respectively. It follows that the total accumulated charge is

$$Z_{\text{acc}}(r) = N_+(r) - N_-(r) + z_C N_C(r), \tag{3.51}$$

which gives the accumulated molecular charge deduced from the structural one by adding the ionic shell.

The standard binding free energy

Note that the standard binding free energy ΔG reported by experiments refers to the standard binding volume $V_0 = 1/C^0$ of one liter per mole [117]. Hence, the binding constant K_b generated from experiment is formulated as $K_b = e^{-\beta \Delta V_0}$. To connect our simulated binding free energy to the experiment, we average the accessible volume V_b of the COM of the ligand in the bound state. As a result, the standard binding free energy from the simulation can be obtained as [117]

$$\Delta G_b = \Delta G^{\text{corr}} + \Delta G, \tag{3.52}$$

with the term $\Delta G^{\text{corr}} = -k_{\text{B}} T \ln(C^0 V_b)$ being the entropy correction arising from the accessible volume of the COM of the ligand in the bound state.

3.3 Experimental methods

Some experimental results, coming from my partners (not my work), are included later in this thesis together with those theoretical conclusions to complete the study. For the

covenience of the reader, few basic principles of those experiments are introduced in the following paragraphs.

Dynamic light scattering

A very fundamental quantity of the nanoparticle is the associated hydrodynamic radius r_{hd}, which is usually converted from the diffusion coefficient D of the nanoparticle, by means of the Stokes-Einstein equation [62]

$$r_{\mathrm{hd}} = \frac{k_{\mathrm{B}}T}{6\pi\eta D}. \tag{3.53}$$

Here, nanoparticles are buffeted by solvent molecules with the solvent viscosity η. One of the most popular experimental methods to measure the diffusivity D, and thus the hydrodynamic radius r_{hd}, is the dynamic light scattering (DLS) method. That method includes a monochromatic light source (usually a laser) aimed at the nanoparticle sample, and a fast photon counter which sequentially collects the scattered light. From a microscopic point of view, the scattered light from particles under Brownian motion can induce a destructive or constructive interference, which ends up with a time-dependent fluctuation in the intensity of the scattered light. This intensity fluctuation is characterized by the intensity correlation function, the latter is related to the diffusion coefficient D via the formula [118]

$$\Gamma = q^2 D. \tag{3.54}$$

Here, Γ addresses the decay rate of the intensity correlation function and q is the wave vector which depends on the scattering angle. For a simple DLS instrument the scattering angle is fixed, providing only the mean diffusion coefficient. A resolution of the full diffusion coefficient distribution requires more elaborated multi-angle instruments. Since the nanoparticle in a solution typically diffuses with an associated hydration layer, it is important to point out that the hydrodynamic radius r_{hd} measured by DLS experiment is essentially the summation of the thickness of the hydration layer and the bare radius of the nanoparticle.

Electrophoretic mobility experiment

The electrophoretic process defines the migration of charged molecules in an electric field. The electrophoretic mobility U_E of the particle can be measured, as a characterization of the extent of the particle movement. The essential information U_E conveys is the electrokinetic potential of the particle, known as the ζ-potential. Other quantities, like the viscosity η of the solution and the length scale a of the particle, also determine the magnitude of U_E via

the Henry equation [119]

$$U_E = \frac{2\epsilon\zeta f(\kappa a)}{3\eta}. \tag{3.55}$$

Here, κ is the inverse Debye length. Importantly, a characterizes the radius of hydrodynamic shear or slipping plane, defining the boundary within which ions and water molecules move with the particle. As a result, the electrical charges that cause the ζ-potential involve not only with bare charges of the particle, but also with charges of ions and water molecules within the slipping plane. In Eq. 3.55, the characteristic function f accounts for the size effect of the molecule as a function of κa. In the level of the Smoluchowski approximation [120], $f \equiv 1.5$ is used for any shape at any concentration. However, the absence of κ approximates the slipping plane equivalent to the particle surface, indicating that the Smoluchowski approximation is applicable mostly for large particles (e.g., folded capillary cell) with $\kappa a \gg 1$. At low values of κa, an equally simple limiting case $f \equiv 1$ applies known as the Hückel approximation. The Smoluchowski and Hückel approximation can be covered in the equation

$$f(\kappa a) = 1 + \frac{1}{2[1 + \delta/(\kappa a)]^3}, \tag{3.56}$$

proposed by Ohshima [121, 122]. Here, $\delta = (5/2)[1 + 2\exp(-\kappa a)]^{-1}$ is a characteristic function of κa. Equation (3.56) varies smoothly from 1, for low values of κa, to the Smoluchowski approximation $f(\kappa a) = 1.5$ in the limit of $\kappa a \to \infty$. The Ohshima approximation covers a broad range of concentrations and particle sizes. However, concerning a particle with high enough mobility U_E, the surface conductivity of the particle should matter. A better description in that case can be referred to the O'Brien-White theory [123].

Isothermal titration calorimetry experiment

Understanding interactions between the polymeric receptor and the protein ligand is a long standing challenge. Calorimetry, in particular isothermal titration calorimetry (ITC), has become a central tool of these studies [124, 125, 126]. It provides a measure of the binding affinity (binding constant), K_b [127], if a suitable binding model for data analysis is applied and correctly interpreted. The idea of the ITC can be illustrated in the following multi-site binding process. Let us denote the protein ligand as L and the polymeric receptor as M in aqueous solution with the reaction

$$\mathrm{L} + \mathrm{ML_{i-1}} \rightleftarrows \mathrm{ML_i}, \;\; 1 \leq i \leq N, \tag{3.57}$$

where i is the coordination number of the binding sites and N is the binding stoichiometry. $[\cdots]$ stands for the concentration of the respective chemical compound. The ITC measures the binding heat of the above reaction, which can be formulated as

$$Q = [\mathrm{M}]_{\mathrm{tot}} V_{\mathrm{tot}} \Delta H N \theta, \tag{3.58}$$

where $\theta = i/N$ is defined as the coverage of the binding sites, $[\mathrm{M}]_{\mathrm{tot}}$ is the total concentration of the receptor M, and V_{tot} denotes the cell volume. In practice, the ligand is experimentally supplied in terms of the titration number. And it is the heat ΔQ regarding the kth titration to be measured, which is equal to the derivative of the total heat Q with respect to the titration number n_{titr},

$$\Delta Q = \frac{[\mathrm{M}]_{\mathrm{tot}} V_{\mathrm{tot}}}{[\mathrm{L}]_{\mathrm{titr}} V_{\mathrm{titr}}} \Delta H N \left(\frac{\partial \theta}{\partial n_{\mathrm{titr}}} \right), \tag{3.59}$$

where $[\mathrm{L}]_{\mathrm{titr}}$ and V_{titr} is the ligand concentration in the titration cell and volume per titration. As seen in Eq. (3.59), ΔQ is still not explicitly a function of the binding affinity K_b, which will be resolved by the relevant binding model. The Langmuir adsorption isotherm [128], as the most representative one, will be introduced afterwards.

Langmuir adsorption isotherm and ITC data fit

Without loss of generality, we start with the binding stoichiometry $N = 1$ where L is considered as the ligand and M as the molecular receptor with only one binding site available. The Langmuir adsorption isotherm connects the binding affinity K_b with the concentration of the reaction species with the equation

$$K_b = \frac{[\mathrm{ML}]}{[\mathrm{M}][\mathrm{L}]}. \tag{3.60}$$

In Sec. 3.1 and for Eq. (3.33), we arrived at the same formula as Eq. (3.60) in the context of the canonical ensemble. In view of that approach, it can be concluded that Eq. (3.60) only applies to the system where the binding sites are independently equivalent and are free of any degree of the binding cooperativity. With Eq. (3.60), one can easily calculate the concentration of unbound ligands/receptors as a function of their total concentration and the binding affinity K_b with equations

$$\begin{aligned} [\mathrm{M}] &= [\mathrm{M}]_{\mathrm{tot}} - K_{\mathrm{b}}[\mathrm{M}][\mathrm{L}], \\ [\mathrm{L}] &= [\mathrm{L}]_{\mathrm{tot}} - K_{\mathrm{b}}[\mathrm{M}][\mathrm{L}]. \end{aligned} \tag{3.61}$$

Solutions of Eq. (3.61) give the expression of [M], [L] and thus the binding sites coverage θ as a function of the total concentration $[\mathrm{M}]_{\mathrm{tot}}$, $[\mathrm{L}]_{\mathrm{tot}}$ and the binding affinity K_{b}. With that, the titration heat series ΔQ recorded in the ITC binding isotherm, as indicated by Eq. (3.59), can be rephrased as

$$\Delta Q = \frac{-K_{\mathrm{b}}\Delta H V_{\mathrm{tot}}}{[\mathrm{L}]_{\mathrm{titr}} V_{\mathrm{titr}}} \frac{d(\Delta_{\mathrm{tot}}^2/4 - f^2([\mathrm{M}]_{\mathrm{tot}}, [\mathrm{L}]_{\mathrm{tot}}))}{dN_{\mathrm{titr}}}, \tag{3.62}$$

with

$$\Delta_{\mathrm{tot}} = [\mathrm{M}]_{\mathrm{tot}} - [\mathrm{L}]_{\mathrm{tot}}, \quad f([\mathrm{M}]_{\mathrm{tot}}, [\mathrm{L}]_{\mathrm{tot}}) = \frac{1 - \sqrt{(K_{\mathrm{b}}\Delta_{\mathrm{tot}} + 1)^2 + 4K_{\mathrm{b}}[\mathrm{L}]_{\mathrm{tot}}}}{2K_{\mathrm{b}}}. \tag{3.63}$$

A fit based on Eq. (3.62) towards the ITC binding isotherm gives access to the value of the binding affinity K_{b}, the stoichiometry N (fixed as 1 for this case) and the enthalpy change ΔH per binding site. As a result, binding details of the reaction Eq. (3.57) in the microscopic level are featured. The above fit originating from the Langmuir isotherm Eq. (3.60) belongs to the single site of identical sites (SSIS) model. The SSIS fits possess small number of the fitting parameters and are almost free of any preknowledge of the binding details, making the SSIS model as the most popular option to resolve the ITC experiment. However, as discussed mainly in Sec. 6, the interpretation of the SSIS fit can become subtle regarding the electrostatically driven complexation with multiple binding sites. The major challenge there is the involvement of the binding cooperativity that has been completely omitted in the SSIS model. The straightforward solution for that is the inclusion of several correlated binding sites possessing different binding affinities. Nevertheless, applications in that respect are constrained to an extent due to a fast growing number of the fitting parameters proportional to the stoichiometry N.

4 Complexation for the linear polyelectrolyte

The subject of this chapter is to introduce the pair association between two linear PEs (LPEs) of the same size but opposite charge, as well as the complexation between LPE and HSA. For LPE-LPE interaction, the system is systematically studied in terms of the PMF along their center-of-mass reaction coordinate via CG, implicit-solvent, explicit-salt computer simulations. The focus is set on the onset and the intermediate, transient stages of complexation. Our study is complemented by a simple theory based on sliding charged 'DH' rods with renormalized charges in addition to an explicit entropy contribution owing to the release of condensed counterions. The above methods and the CG model of the LPE is employed latter for the study of the LPE-HSA complexation. Note that the wording and figures in sections 4.1 - 4.3 and section 4.4 are taken almost literally from our previous publication [19] and publication [129], respectively.

4.1 Models and methods

In this section, we introduce the CG model for the LPE and relevant simulation protocols. The critical Manning parameter is defined to address the LPE with various bare charges. The binding pathway of the LPEs is characterized by the PMF profile and LPE alignment order paramter, which will be introduced afterwards.

Coarse-grained linear polyelectrolyte model and simulations

Consider an aqueous solution containing two LPE chains of the same size but opposite charge in the presence of salt ions at a finite concentration. We treat the solvent implicitly via a uniform dielectric background with a permittivity constant of water at room temperature, $\epsilon_r = 78.44$. The LPE chains are represented by a coarse-grained beads-on-the-string model [130]. Approximately, each bead represents a monomer for a realistic LPE chain. In addition to electrostatic interactions, the polymer beads interact with each other in terms of the LJ potential

$$U_{\mathrm{LJ}}(r) = 4\epsilon_{\mathrm{LJ}} \left[\left(\frac{\sigma_{\mathrm{LJ}}}{r} \right)^{12} - \left(\frac{\sigma_{\mathrm{LJ}}}{r} \right)^{6} \right] \tag{4.1}$$

with a diameter $\sigma_{\mathrm{LJ}} = 0.3\,\mathrm{nm}$ and an energy $\epsilon_{\mathrm{LJ}} = 0.1\ k_{\mathrm{B}}T$. Monovalent salt ions are modeled explicitly as charged beads with the same LJ potential as that for the LPE beads. The valency of small ions is $z_{\pm} = \pm 1$.

The LPE chain connectivity is imposed by a harmonic potential

$$U_{\text{bond}}(l) = \frac{1}{2}k_{\text{b}}(l - l_0)^2, \tag{4.2}$$

where l represents the distance between consecutive beads, and $l_0 = 0.4\,\text{nm}$ is the equilibrium bond length. The spring constant is $k_{\text{b}} = 4100\,\text{kJ mol}^{-1}\,\text{nm}^{-2}$. To account for the polymer backbone flexibility, we restrain the bond angle also by a harmonic potential

$$U_{\text{angle}} = \frac{1}{2}k_{\text{a}}(\omega - \omega_0)^2, \tag{4.3}$$

where ω is the angle between a triplet of adjacent beads, and $\omega_0 = 120^\circ$ its prescribed equilibrium value. The potential constant is $k_{\text{a}} = 418$ kJ mol^{-1} rad^{-2} [131].

In this work, we consider relatively short LPE chains with the total number of beads $N_{\text{b}} = 25$, close to the degree of polymerization for LPEs used in some related experimental studies [132, 133, 134, 135, 48]. The contour length of the LPE chains is $L_c \simeq (N_{\text{b}} - 1)l_0 \sin(\omega_0/2) \simeq 8.3\,\text{nm}$, where the sine-function takes care of the bond angular constraints in a moderately stretching regime. Each bead carries a bare Coulomb charge $|q_{\text{b}}| = e|z_b^{\pm}|$, with e being the unit charge and $|z_b^+| = |z_b^-| \equiv z_b$ the valency. The total charge of each LPE chain is $|Q_{\text{b}}| = N_{\text{b}}|q_{\text{b}}|$. Since we consider complex formation between two anti-symmetric LPE chains, the final complex is electroneutral. The two polymers have the same properties except with opposite charges, that is, $Q_{\text{b}} > 0$ for one LPE chain, and $Q_{\text{b}} < 0$ for the other.

Our simulations are based on the (LD) (See Sec. 3.2). All beads have the same unit mass, which is set to minimize the inertia effects and enhance sampling. The choice of particle mass does not affect the equilibrium properties of polymers studied in this work. The total potential energy of the entire system is the sum of all the contributions $U = U_{\text{Coul}} + U_{\text{LJ}} + U_{\text{bond}} + U_{\text{angle}}$. The Langevin friction is chosen as $\xi_i = 1.0$ ps^{-1} such that it dissipates energy at constant temperature $T = 300$ K on the time scale much faster than those governing the dynamics of the polymer system. To integrate the equations of motion, we employ the leap-frog algorithm with a time step of 2 fs. The simulations are carried out by the GROMACS 4.5.4 software package [112].

In the production runs, we use a cubic box with a side length of $L = 30\,\text{nm}$ with periodic boundary conditions in all three directions. The center of mass translation of the system is removed in every 10th integration time step. The electrostatic interactions are treated with the PME method (See Sec. 3.2) [136], where the long-range potential is evaluated in the reciprocal space using the FFT with a grid spacing 0.12 nm and the cubic interpolation of the fourth order. We use a cutoff radius $r_{\text{cut}} = 3.0\,\text{nm}$ for the short-range electrostatics and the LJ interactions. The choice of the cutoff is verified by reference simulations with increased

cutoff value $r_{\rm cut} = 5.0\,$nm. For LPE chains with the highest charge density simulated in this work (Manning parameter $\xi = 2.31$, defined below), where the electrostatic interactions are most significant, the potential of mean force (PMF) curves deviated less than 6% from the results treated with $r_{\rm cut} = 3.0\,$nm. In all simulations, the LPEs are immersed in a salt solution with $N_i = 325$ pairs of cations and anions, resulting into a salt bulk concentration of $c_0 = N_i/L^3 \simeq 20$ mM.

Coarse-grained HSA model

The protein sequence for the HSA is provided by PDB databank: ID=1N5U [137]. Every amino acid is described by a single bead positioned at its C_α atom. The native structure of the protein is maintained by a Go-model like force field as provided from the SMOG webtool for biomolecular simulations [138, 139]. In terms of the Go-model force field, the protein is represented as a chain of one-bead amino acids whose structure is biased toward the native configuration by means of simple LJ-like non-bonded interactions between beads. This extreme simple model has successfully reproduced processes of protein folding and ligand complexation [140]. Here, Go-model well persists the electrostatic information and the native structure of the HSA, which thus is very eligible to study the LPE-HSA complexation. We use the Henderson-Hasselbalch equation to calculate the charge of the acidic and alkaline amino acid residues after putting in the respective pK_a value. With that and at physiological pH = 7.4, the amino acids ARG and LYS residues are assigned a charge +1 e, while ASP and GLU are -1 e, and HIS is neutral. In the end, the net charge of the simulated HSA is -14 e.

Charge densities and counterion condensation

In Sec. 3.1, we have introduced the Onsager–Manning–Oosawa theory and the concept of counterion condensation. Essentially, the net charge of a highly-charged LPE is renormalized by partial condensation of the surrounding counterions. The condensed and free ions should be considered separately as two different liquids. While the counterions condensed at the surface of the LPE backbone form a strongly-correlated liquid, the free ions in the diffusive double layer [141, 142] can be approximately described by a DH-like mean-field theory. The analytic approach will be utilized later in this work to develop a simple expression for the PMF between two anti-symmetric LPEs. In this work, we consider a systematic scan of the Manning parameter in the range from $\xi = 0.29$ to $\xi = 2.31$. The line charge density is $\lambda = |q_{\rm b}|/[l_0 \sin(\omega_0/2)]$, and $l_{\rm B} = e^2/(4\pi\epsilon_0\epsilon_r k_{\rm B}T)$ stands for the Bjerrum length, which is $l_{\rm B} = 0.71$ nm for water at room temperature as used in our simulations. That corresponds

to the the bare charge density from $\lambda = 0.412$ to 3.3 e/nm tuned by the monomeric (partial) charge between $q_\mathrm{b} = 0.14286e$ and $q_\mathrm{b} = 1.14286e$. The resultant effective charge of the LPE as Manning parameter $\xi > 1$ can refer to Eq. 3.21.

In order to estimate the number of condensed counterions, N, in our simulations, we count an ion as condensed if it is located within a radial distance r_0 from any bead of a LPE chain with the opposite electrostatic charge. To avoid double counting, each ion is counted only once according to the nearest distance to the polymer beads. Understandably, the radius r_0 lacks a rigorous definition (see, e.g., the discussion in Refs. [78, 143]), in particular for flexible LPEs in an electrolyte solution. In this work, we propose an unambiguous procedure to account for counterion condensation: the radius r_0 is fixed such that the Manning prediction of $N = \lambda/e(1 - 1/\xi)L_c$ is obeyed for each LPE chain. This procedure yields $r_0 = 0.5, 0.56, 0.63, 0.68,$ and $0.74\,\mathrm{nm}$ for $\xi = 1.15, 1.44, 1.73, 2.02,$ and 2.31, respectively. These values are reasonable because it is known that r_0 increases monotonically with increasing ξ and that it should be identical to the effective LPE (modeled as rod) radius for $\xi = 1$ [78], which is about $0.3 - 0.4$ nm for our LPE model. Similar values of r_0 can be estimated from an inspection of the radial distribution of counterions (not shown) around the LPE beads (see, e.g., Refs. [143, 132, 131]).

PMF calculations

The method to obtain the PMF between two oppositely-charged LPEs is introduced in Sec. 3.2. The distance r between the COM of the two LPE chains serves as the reaction coordinate. An exemplifying snapshot of two LPEs before association is shown in Fig. 4.1(a). To be sepcific, the well separated state is taken as $r \sim 12$ nm and the final state is at $r \sim 0.5$ nm. We use an analogous procedure to calculate the free energy of stretching a single LPE chain. In that case, the distance between the head and tail monomers from the same LPE chain serves as the reaction coordinate.

LPE alignment order parameter

In order to characterize and demonstrate the mutual alignment of two highly-charged LPEs during complex formation, we introduce the order parameter m_{pp} defined as

$$m_{pp}^{i} = \left\langle \frac{|\vec{t}_{ic} \cdot \vec{t}_{cc}|}{||\vec{t}_{ic}||\,||\vec{t}_{cc}||} \right\rangle . \tag{4.4}$$

Here, $\vec{t}_{ic}$ is the intra-LPE direction vector connecting one terminal bead and the central bead of the same polymer i, with $i = 1, 2$, whereas $\vec{t}_{cc}$ is the inter-LPE direction vector linking the

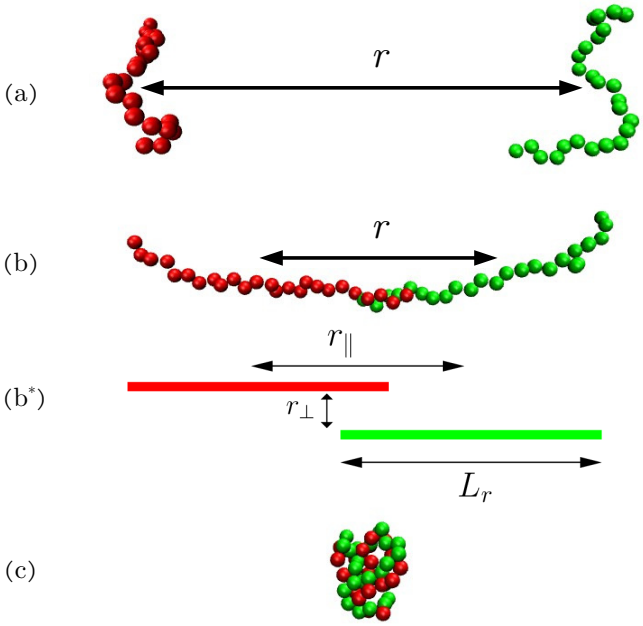

Figure 4.1: Snapshots of the LPE binding process along the center-of-mass reaction coordinate r, depicting the situation of (a) initially separated LPEs in a coil-like state, (b) the 'handshake' at the onset of complexation between elongated LPE chains, and (b*) a schematics thereof where the whole situation is projected on parallel, sliding-rods. The red rod depicts the polyanionic chain, whereas the green rod the polycationic chain in our DH rod model (defined below). Panel (c) depicts the final, entangled LPE complex. The reaction coordinate r corresponds to the COM distance between two LPEs of opposite charge. Each LPE chain consists of 25 monomeric units each of the same absolute partial charge. The Manning parameter in this example is $\xi = 2.02$, and the LPE chains are immersed in a salt solution of the bulk concentration $c_0 \simeq 20$ mM (ions not shown).

central beads of both LPEs. The sign $||\ldots||$ represents the norm of a vector, and $\langle\ldots\rangle$ denotes the ensemble average. For stretched, rod-like polymer configurations, we expect parallel alignment of both vectors $\vec{t}_{ic}$ with $\vec{t}_{cc}$, *i.e.*, the LPE chains are aligned with themselves and with the connection axis. In that case, the order parameter approaches unity for both LPE chains, $m^i_{pp} \lesssim 1$. If two parallel rods approach each other in a perpendicular direction, or if the rods are perpendicularly approaching, or if the orientations of the LPEs are uncorrelated, we would expect an average value of the order parameters much closer to $m^i_{pp} \simeq 1/2$. We will plot and discuss the distance-resolved value for $m_{pp}(r) = [m^1_{pp}(r) + m^2_{pp}(r)]/2$, which is averaged over the two LPE chains.

Moreover, we monitor the distance-resolved end-to-end distance $R_{ee}(r)$ of the LPEs as they approach each other. A stretching of the LPE chains can then be identified simply from the increase of $R_{ee}(r)$ at a certain COM distance.

4.2 An analytical model for the PMF between highly-charged LPE chains

To attain a better understanding of the thermodynamic driving forces and the mechanisms of LPE–LPE association, we now introduce a simple electrostatic model for the PMF between highly-charged LPE chains ($\xi > 1$). We assume that the LPEs adopt an isolated, coil-like state when they are far apart, as sketched in Fig. 4.1(a). In this case, the LPEs interact roughly with a DH-like potential $V_{\mathrm{DH}}(r) \propto Q_{r\mathrm{B}}^2 \exp(-\kappa r)/r$, where $Q_r \simeq 11.7e$ is the renormalized net charge of each LPE and $\kappa = \sqrt{8\pi l_{\mathrm{B}} c_0}$ the usual DH screening parameter. For distances larger than the contour length $r \gtrsim L_c$ this accounts only for weak attraction ($\lesssim k_{\mathrm{B}}T$) and will be discarded in the following discussion. We further assume that during their association at smaller distances $r \lesssim L_c$, the two LPEs are in a parallel sliding conformation, as depicted in Fig. 4.1(b*), until they reach a final state with r close to zero. In the latter, the LPE chains have collapsed into a globular complex, cf. Fig. 4.1(c). Consequently, we assume that the PMF is dominated by a parallel sliding process for a wide range of separations.

We model the two approaching LPE chains in their fully stretched association configuration with the simplest analytically tractable model, that is, two parallel, infinitely thin, and oppositely-charged rods of length L_r. We define the effective rod length L_r as the COM distance at the onset of the elongated LPE configuration, which can be read off in Fig. 4.2(a) at the intersections of the diagonal dashed line, $R_{\mathrm{ee}} = r$, and the profile of the end-to-end distance $R_{\mathrm{ee}}(r)$. The effective length L_r increases with increasing ξ, since larger electrostatic attraction promotes the jump into the elongated state at larger separations. For small values of ξ, the effective length L_r is significantly smaller than the contour length $L_c = 8.3$ nm of the chains, since the attraction in that case is not strong enough to extend the chains considerably. However, for higher charges, that is, for higher values of ξ, the effective length approaches L_c.

The COM distance of the two rods is again denoted by r, with the parallel component $r_{\parallel}$ and the perpendicular component $r_{\perp}$, as shown in Fig. 4.1(b*). The latter is kept fixed and reflects the closest distance of the two LPEs, which is related to the LJ diameter σ_{LJ}. We now assume that the major interaction contribution to the total free energy arises only from the neighboring parallel segments of length $L_r - r$ from each rod. In the following, we will evaluate in detail the electrostatic contribution based on a DH approach and additionally account for the purely entropic contribution of the counterion release effect in the scenarios with $\xi > 1$.

We first evaluate the DH energy corresponding to the electrostatic interaction between two

parallel, partially neighboring rods. Assuming $r_\perp \ll L_r$, we may neglect edge effects and approximate the pair potential between the neighboring segments as those from infinitely long rods. With the pairwise additive approximation, we can derive the overall interaction energy then as [85]

$$\beta W_{\mathrm{DH}}(r) = (r - L_r) l_{\mathrm{B}} (1-\theta)^2 (\lambda/e)^2 \int_{-\infty}^{\infty} \frac{e^{-\kappa\sqrt{x^2+r_\perp^2}}}{\sqrt{x^2+r_\perp^2}} dx. \tag{4.5}$$

Here, $\beta = 1/(k_{\mathrm{B}}T)$, λ is the bare line charge of a LPE rod, which can be renormalized by condensed counterions. The fraction of neutralization is $\theta = 0$ for $\xi < 1$ and $\theta = 1 - 1/\xi$ if $\xi > 1$. Note that in the latter case, the effective charge density stays as e/l_{B}, irrespective of the COM distance r. Performing the above integral, yields [85, 144]

$$\beta W_{\mathrm{DH}}(r) = \frac{2}{l_{\mathrm{B}}} (r - L_r) K_0(\kappa r_\perp) \times \begin{cases} \xi^2 & \text{for } \xi < 1, \\ 1 & \text{for } \xi \geq 1, \end{cases} \tag{4.6}$$

where $K_0(\kappa r_\perp)$ is the Bessel function of the second kind. According to Eq. (4.6), the electrostatic DH part of the PMF is linear in the center-of-mass distance r, which is a logical outcome of our asummption, since only neighboring segments of the parallel aligned rods contribute. Note again that because of the charge renormalization effect for $\xi \geq 1$, this contribution does not explicitly depend on the charge density.

For $\xi \geq 1$, in addition to the direct electrostatic interactions between polyions, we may estimate the contribution to the free energy of LPE complexation due to the release of counterions. For association between two oppositely-charged LPEs with the Manning parameter $\xi \gg 1$, the free energy is dominated by the entropically favored release of condensed counterions. The idea was first proposed by Lohman and coworkers [145, 146] and supported later by other theoretical investigations including coarse-grained (but explicit-salt) computer simulations [18, 131]. The entropy gain upon releasing n bound counterions is

$$\Delta S_{\mathrm{ion}} = n k_{\mathrm{B}} \ln(c_{\mathrm{b}}/c_0), \tag{4.7}$$

where c_{b} corresponds to the effective density of the condensed ions in the vicinity of the LPE and c_0 is the ion bulk density. The corresponding free energy gain due to counterion release is then given by

$$\beta W_{\mathrm{ion}} = -n \ln(c_{\mathrm{b}}/c_0). \tag{4.8}$$

For complex formation between two LPEs of opposite electric charge, each LPE chain carries condensed counterions of a line density $\lambda\theta$, where θ is the fraction of the LPE charge

neutralization by counterions. When the LPE segments approach each other, all counterions in the overlapping region are liberated and released into the bulk solution. The number of released ions is $n = 2 \times \lambda\theta(L_r - r)/e$. In terms of the Manning parameter, n can be expressed as

$$n(r) \simeq \begin{cases} 0 & \text{for } \xi < 1, \\ \frac{2}{l_\mathrm{B}}(\xi - 1)(L_r - r) & \text{for } \xi \geq 1. \end{cases} \tag{4.9}$$

The density of the bound ions [131, 132] is defined by the number of condensed counterions N and their occupied volume V, i.e., $c_\mathrm{b} = N/V$. The condensed counterions reside around each rod at a radial distance between the inner radius σ_LJ and the outer radius r_0. The occupied volume thus corresponds to that of two hollow cylinders, $V = 2s_c(L_r - r)$, where $s_c = \pi(r_0^2 - \sigma_{LJ}^2)$. Accordingly, the density of the bound ions for $\xi > 1$ can be estimated as

$$c_\mathrm{b} = \frac{(\xi - 1)}{l_\mathrm{B} s_c}. \tag{4.10}$$

The free energy contribution from the released counterions is then given by

$$\beta W_\mathrm{ion} = 2\frac{(\xi - 1)}{l_\mathrm{B}}(L_r - r)\ln\Big(\frac{\xi - 1}{l_\mathrm{B} s_c c_0}\Big). \tag{4.11}$$

The above expression is valid only for $\xi > 1$; otherwise, $W_\mathrm{ion} = 0$ since there are no counterions condensed on the LPE surface. For a salt concentration $c_0 = 20$ mM and, for instance, ξ between 1.15 and 2.31, Eq. (4.10) predicts $c_b \simeq 0.7$ M and 2.12 M, respectively. That corresponds to 3.6−4.7 $k_\mathrm{B}T$ of dissociation free energy per single released ion, respectively.

Finally, we sum up the DH contribution W_DH and the counterion release W_ion, viz.

$$\beta W_\mathrm{theo}(r) = \begin{cases} \dfrac{2}{l_\mathrm{B}}\xi^2 K_0(\kappa r_\perp)(r - L_r) \\ \qquad \text{for } \xi \leq 1, \\ \dfrac{2}{l_\mathrm{B}}\Big[K_0(\kappa r_\perp) + (\xi - 1)\ln(\frac{\xi - 1}{l_\mathrm{B} s_c c_0})\Big](r - L_r) \\ \qquad \text{for } \xi > 1. \end{cases} \tag{4.12}$$

Equation (4.12) predicts a PMF between LPE chains to be linearly dependent on the COM distance r. As previously concluded in related simulations of LPE complexation [18], the PMF is dominated by electrostatic enthalpy for $\xi < 1$ and counterion-release entropy for $\xi \gg 1$.

It should be noted that Eq. (4.12) is valid only for a finite length of overlapping rod segments, $r < L_r$. It neglects smaller contributions for larger distances $r > L_r$. The

separation distance between the rods $r_\perp$ is approximately equal to the LJ diameter σ_{LJ}. However, $r_\perp$ could be smaller than that, since a bead of one LPE chain can sit in the region between the two neighboring beads of the other LPE chain. In this work, we obtain the value for $r_\perp$ by the best fit of Eq. (4.12) to the simulation data for $\xi = 1.0$, yielding $r_\perp = 0.28$ nm. We use this value for all other ξ-values.

Finally note that the two LPEs in the overlapping parts are almost free of the surrounding ions and therefore interact as (almost) bare charges via unscreened Coulomb force. However, the total free energy of the LPEs, which is the work of bringing the two LPEs from large separations to close distance, cannot be computed in terms of the unscreened electrostatics, as at large distances the screening always becomes significant. Furthermore, the electrostatic attraction should comprise the portion of the energy penalty to deprive the condensed counterions on the overlapping part. Thus, attraction only in terms of bead bare charge will exclude that energy and eventually lead to a underestimate of the PMF. As an approximation, we adopt the effective charge to implicitly account that energy penalty. Our intention with this simple model is to qualitatively describe the main characteristics of the rather complex association process obtained by the simulations. As seen by the nice agreement between the theory and the simulations later in Fig. 4.3(b), the used model is able to capture the basic features of the association.

4.3 Results for LPE-LPE interaction

Structure of the LPEs during association

A first insight into the configurations of the LPE chains along their approach to association can be attained by analyzing the distance-resolved end-to-end distance $R_{ee}(r)$ of the individual LPEs. Figure 4.2(a) shows the average $R_{ee}(r)$ of the antisymmetric LPEs with different Manning parameters. At large separations, where the LPE chains are in a coil-like state and independent of each other, cf. Fig. 4.2(a), $R_{ee}(r)$ is constant. The effective size of the coil increases with increasing ξ due to self-electrostatic repulsion within the LPE chain. For highly charged chains, $\xi \gg 1$, a significant and steep, almost discontinuous increase of the end-to-end distance can be observed at COM distances close to the contour length $r^* \simeq 5 - 7$ nm. The exact value of the critical distance r^* depends on ξ. For larger ξ, the critical distance increases towards the maximum contour length and the magnitude as well as steepness of the jump grow. This behavior strongly indicates stretching of the LPE chains towards each other and 'handshake' [147] at a critical distance r^* to assume a maximum end-to-end length R^*_{ee} as shown in the snapshots in Fig. 4.1(b). An observed linear

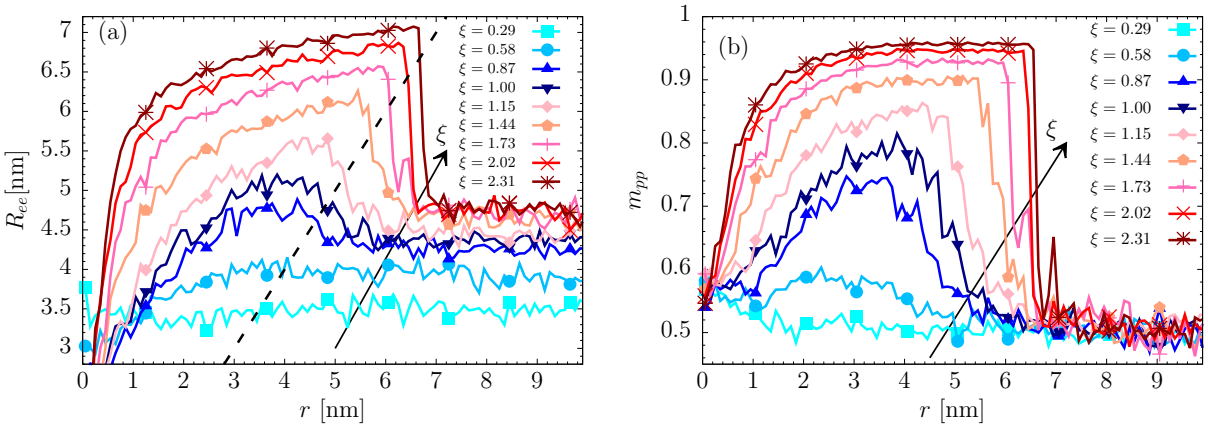

Figure 4.2: (a) The LPE end-to-end distance R_{ee} as a function of the LPE–LPE COM distance r for various values of the Manning parameter ranging from $\xi = 0.29$ to $\xi = 2.31$ at salt concentration $c_0 = 20$ mM. For $\xi > 1$, R_{ee} jumps up at a certain distance r^* to the value R^*_{ee}. The black dashed diagonal line shows the function $R_{ee}(r) = r$, revealing a linear correlation $R^*_{ee} \approx r^*$. (b) The LPE–LPE orientation order parameter m_{pp}, Eq. (4.4), is monitored as a function of the COM distance r for various values of the Manning parameter at salt concentration $c_0 = 20$ mM. For both panels, $\xi = 0.29, 0.58, 0.87, 1.00, 1.15, 1.44, 1.73, 2.02$ and 2.31 (from bottom to top). The arrows signify the trend for increasing ξ.

relation $R^*_{ee} \propto r^*$, cf. Fig. 4.2(a), further consolidates that proposition. At small distances, $r \lesssim 2$ nm, the LPE chains seem to collapse again to with the $R_{ee}(r)$ approaching the values that correspond to the isolated coil states.

The behavior of $R_{ee}(r)$ for the associated states strongly correlates with the alignment order parameter m_{pp}, shown in Fig. 4.2(b). At large distances $r \gtrsim 6.5\,\text{nm}$, the LPE chains are independent of each other and uncorrelated in any alignment, as indicated by Fig. 4.1(a). In that case, the order parameter tends to the value $m_{pp} \simeq 1/2$. At the intermediate distances $r \simeq 5 - 7\,\text{nm}$, again cf. Fig. 4.1(b), the ends of different LPEs jump together and the polymer chains become elongated and m_{pp} rises to high values, indicating parallel alignment of stretched LPEs. The order parameter in this regime increases with increasing ξ. Particularly for $\xi = 2.31$, the order parameter reaches $m_{pp} = 0.95$, implying that the two LPEs get almost completely stretched and perfectly aligned. At smaller distances, $r \lesssim 2$ nm, the order parameter tends to the value $m_{pp} \simeq 1/2$, and the previously extended LPEs collapse into a compact globule. In a relatively large spatial regime roughly appearing at distances between $1 - 2\,\text{nm} < r < 5 - 7\,\text{nm}$ (with the exact values depending on ξ), both LPEs slide along each other in a stretched and parallel configuration, with their orientations pointing along the connection axis.

An interesting question arises as to why do the LPEs tend to associate via the elongated sliding configuration rather than via other possibilities, such as perpendicular or parallel sideward approach. Fixing the COM separation between the two LPEs, the elongated configuration allows the terminal segments on the respective LPEs coming into a close contact.

In presence of the strong electrostatic attraction and counterions release, this configuration has the smallest free energy compared with all other realizations. Similar elongated sliding approaches of LPEs have been reported (but remained undiscussed) in a number of previous publications in coarse-grained as well as atomistic-level simulations [18, 148, 149]. This sliding mechanism has implications on the interpretation and theoretical description of the PMFs along their COM distance reaction coordinate, as discussed in the following.

PMF profiles and counterion-release

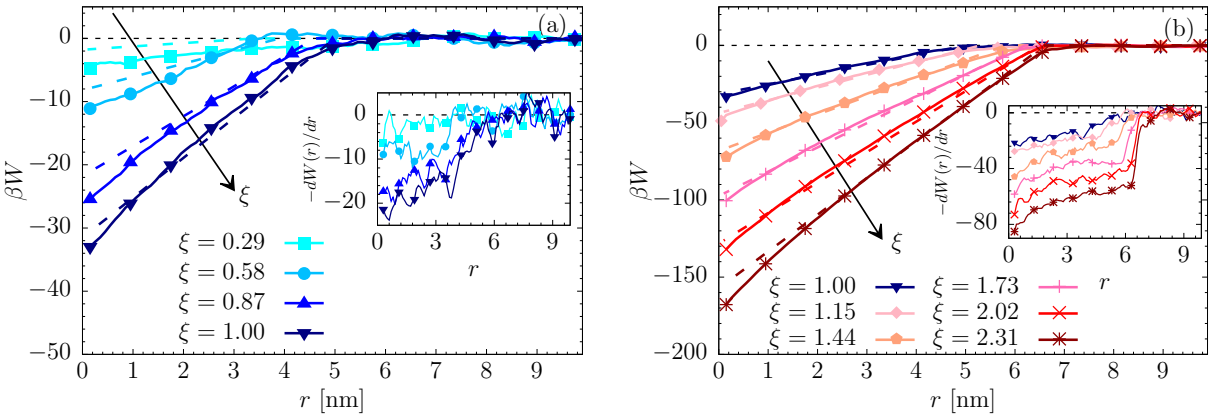

Figure 4.3: The PMF $W(r)$ in units of $k_BT = \beta^{-1}$ between two oppositely charged LPEs as a function of their COM distance r. The simulation results are represented by solid curves for different values of the Manning parameter ξ (see legend). The bold dashed lines are the PMF predictions $W_{\text{theo}}(r)$ from Eq. (4.12). The insets show the mean force $-dW(r)/dr$ in units of $k_BT\,\text{nm}^{-1}$. The thin dashed line is the baseline $W(r) = 0$. The arrows signify the trend for increasing ξ.

In Fig. 4.3 we present the PMF, $W(r)$, between the two LPE chains with different Manning parameters ξ. Here the salt concentration is again $c_0 \simeq 20$ mM. Figure 4.3(a) shows the PMFs for $\xi \leq 1$ and (b) for $\xi \geq 1$. The three generic stages of the LPE–LPE association discussed before are reflected also in the behavior of the PMF: When the LPE chains are far apart, $r \gtrsim 6.5\,\text{nm}$, they do not significantly interact with each other (on the shown scale) regardless of the Manning parameter. Once the LPE chains begin to associate at $r^* = 5 - 7$ nm and stretch at intermediate separations $1 - 2\,\text{nm} < r < r^*$, $W(r)$ becomes nearly a linear function of r, with the slopes increasing with increasing ξ. Consequently, the mean force $f = -dW(r)/dr$, shown in the insets, can be regarded as nearly constant in that r-range, as reported already in previous simulations [148]. However, some slope in the mean force is clearly visible, especially for the smaller ξ-values, so the assumption of a strictly constant mean force is not generally true. Strikingly, the mean force $f = -dW(r)/dr$ exhibits a discontinuity at r^* for $\xi \gtrsim 1$, see the inset to Fig. 4.3(b), a fact that will be discussed later in more detail. At smaller separations $r < 1 - 2\,\text{nm}$, the LPE chains tend to intertwine into

a collapsed globule and by that further increasing the association free energy. In this regime, the corresponding attraction grows even stronger (superlinear) with the distance. The value of $W(r \simeq 0)$ at the associated state represents the free energy of LPE–LPE complexation. Its value increases with the Manning parameter ξ, as can be expected from increased Coulomb attraction between both LPEs. The thermodynamics in terms of enthalpy and entropy of the final complex was investigated in detail by Ou and Muthukumar [18].

In the same figures, we plot the PMF predictions of our simple theory given by Eq. (4.12) by dashed lines. We note again that for each ξ, we determine the effective length L_r at the onset of attraction of stretched LPEs directly from Fig. 4.2(a) and use it as an input to the theory, which is applicable for $r < L_r$. Another parameter in our analytical model, the rod distance $r_\perp = 0.28$ nm, is fixed by fitting the theory to the linear part of the PMF for $\xi = 1$, where LPE chains are mostly stretched and the theory is expected to be most reliable. For all other ξ-values the model now delivers a prediction. We see in Fig. 4.3(a) that for $\xi \leq 1$, the discrepancy between the theory and the simulations grows in relative terms with decreasing ξ at the whole attractive range of r. This is expected as the assumption of a parallel rod-like sliding mechanism becomes less accurate for decreasing ξ. In contrast, for $\xi > 1$ the linear trend of the analytical prediction agrees very well, even quantitatively, with the simulated PMFs for intermediate distances 2.5 nm $\lesssim r \lesssim$ 6.5 nm. Note that in this regime the mean force is relatively constant, as assumed in the theory. At very small distances $r \lesssim 2$ nm, the LPE chains collapse into a globule and therefore the rod model clearly breaks down. This shows that the first steps of the LPE association for highly-charged LPEs can be very well captured by the analytical model based on two rigid sliding rods together with counterion release entropy. Note that the differences between the PMF for $\xi = 1$ and the PMFs for $\xi > 1$ are solely provided by counterion-release entropy. The enthalpic Coulomb part (attraction of rods with renormalized charge) becomes less important with increasing ξ.

As a minor but interesting note we now estimate the relative time period of the association process into the final complex with respect to ordinary diffusion. The typical diffusion time over a length L in a simple Rouse picture [150] would be $\tau_D \simeq N_b \xi_m L^2/k_B T$, where ξ_m is the friction constant of a monomer. This has to be compared to a macromolecule associating a length L with a speed $L/\tau_{\text{assoc}} = f/(N_b \xi_m)$ under the influence of a driving force f. Comparing the time scales, we obtain simply $\tau_{\text{D}}/\tau_{\text{assoc}} \simeq \beta f L$. Pluggin in our calculated values of the mean force (insets to Fig. 3) for L on a nanometer scale we see that, for not too small Manning parameters ξ, the association for electrostatic and counterion-release driven LPE complexation can be easily 1–2 orders of magnitude faster than a simple diffusion-dominated association process. These short time scales have indeed been observed in coarse-grained computer simulations of unrestrained LPE complexation [44, 45, 18].

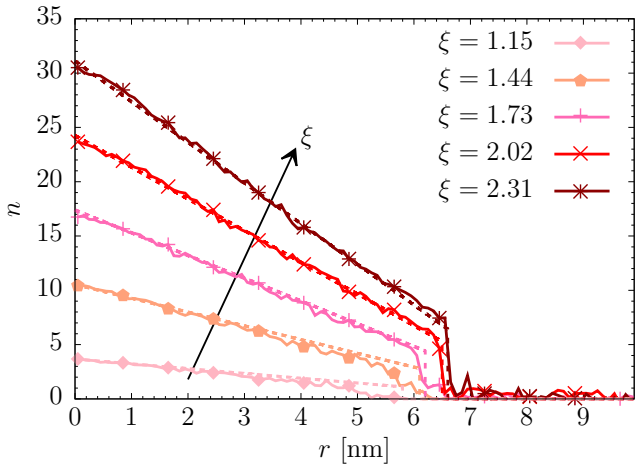

Figure 4.4: The total number of the released counterions n per LPE versus the LPE–LPE COM distance r during LPE complexation. (The numbers *per LPE* are half of that.) The simulation results are represented by solid curves for different values of the Manning parameter ξ (see legend). The dashed lines are the number of released counterions predicted via Eq. (4.9). The arrows signify the trend for increasing ξ.

In order to further corroborate our theoretical assumptions on the counterion release effect, we now examine the number of released ions during the association process. Figure 4.4 presents the number $n(r)$ of released counterions per LPE (averaged over both chains) for various ξ values resolved in COM distance r. In the coil phase, where both LPEs are independent of each other, the amount of condensed counterions reaches its maximal value. As mentioned before, we define the Manning radius r_0 for each value of ξ such that the theoretical prediction for $N = N_b z_b(1 - 1/\xi)$ can be reproduced for an isolated rod. At the critical distance r^*, the number of condensed counterions experiences a discontinuous jump ΔN. Here, the coil phase goes over to the elongated phase where the end parts of the LPEs stick together and by that trigger the release of ΔN counterions. The latter increases with ξ, where in the case of $\xi = 2.31$ more than 3 counterions are liberated per LPE. After the jump, a linear decrease in the number of condensed counterions demonstrates the progressive release of counterions from the overlapping segments of LPEs, as predicted by our theory, Eq. (4.9). Finally, all counterions are released in the final complex at $r = 0$, where both LPEs completely neutralize each other. Here, we can observe that between $\xi = 1.15$ and 2.31 between 2 and 15.5 ions are released per LPE into the bulk, respectively. Assuming approximately 5 $k_\mathrm{B}T$ per ion (see methods after Eq. (4.11)) in the case of $\xi = 2.31$, we end up with a total free energy of complexation about 155 $k_\mathrm{B}T$, in a good agreement with the PMF data in Fig. 4.3(b).

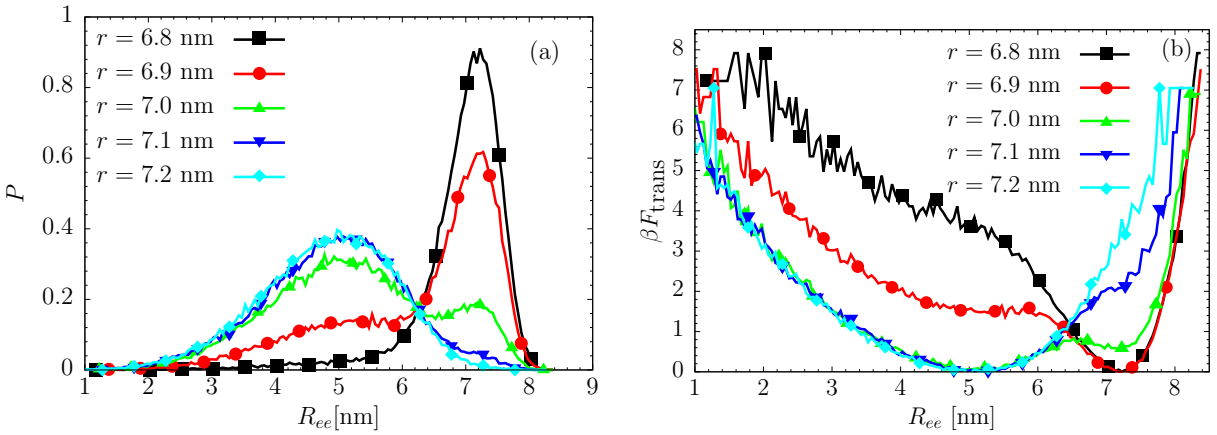

Figure 4.5: (a) Probability distribution $P(R_{ee})$ for different COM distances r close to the critical jump distance $r^* \simeq 6.9 - 7.0$ nm with the Manning parameter $\xi = 2.31$. (b) The corresponding transition free energy $F_{\rm trans} = -k_{\rm B}T \ln P$ as a function of R_{ee}.

Discontinuity in LPE complexation

The discontinuities in the mean force, condensed counterion number $N(r)$, as well as the end-to-end distance R_{ee} clearly suggest that the system undergoes an abrupt change at the critical distance r^* of the approaching LPE chains. In an attempt to characterize this transition in more detail, we have calculated the probability distribution $P(R_{ee})$ of the LPE end-to-end distance for various fixed (harmonically constrained) COM distances r in the range from 6.8 nm to 7.2 nm for the case of $\xi = 2.31$, thereby crossing its critical distance r^*, shown in Fig. 4.5(a). For the two largest as well as for the smallest distance r, we find single-peaked distributions, corresponding to the well defined single states, coil and stretched LPE chains, respectively. At around $r^* = 6.9$–7.0 nm, however, a bimodal distribution between the two states appears, indicating a structural coexistence, separated by unlikely states. The transition free energy profiles $F_{\rm trans}(R_{ee}) = -k_{\rm B}T \ln P(R_{ee})$ are plotted in Fig. 4.5(b). In the bimodal states, the potential barrier separating the two states has a height of the order of $\Delta F_{\rm trans} \sim k_{\rm B}T$. Note also that the peak position of the extended state is located at values of about $L_r \simeq 7.2$ nm, somewhat larger than r^*. The reason is that the stable state apparently needs some finite overlap, i.e., a critical attraction to warrant a stable state.

So, what is the reason for this bimodal distribution? Consider first the LPE chains in the coil state, i.e., when $r > r^*$. In a rare fluctuation, the chains stretch out, accompanied by a significant loss in conformational entropy, and may achieve their handshake by overlapping with one or a few more monomers at the ends. For $\xi > 1$, we have shown that this 'first touch' will be accompanied by a significant release of counterions, contributing a large favorable entropy of several $k_{\rm B}T$ per released ion. Apparently, this gain in counterion entropy is large enough to compensate for the loss in the conformational entropy of LPE chains such that

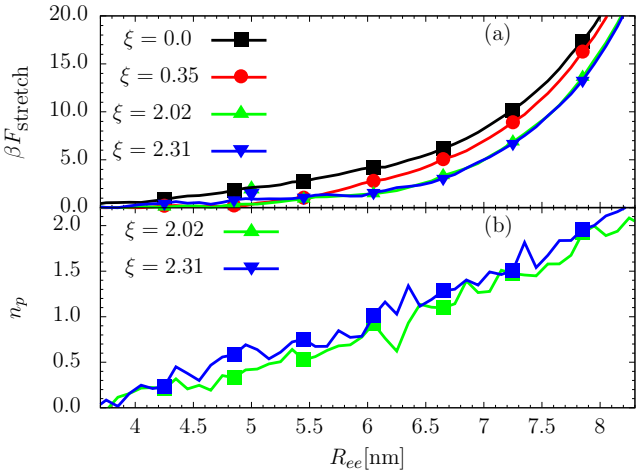

Figure 4.6: (a) The free energy of stretching a single LPE is plotted as a function of R_{ee} as obtained from pulling simulations. (b) The number of the released counterions n_p during stretching a single LPE is plotted as a function of its end-to-end distance R_{ee}.

a coexistence can be established in this restrained equilibrium. Quantitatively, we estimate the stretching entropy of a single LPE from our steered Langevin simulations. Results are shown in Fig. 4.6(a) for various ξ values, including the neutral reference $\xi = 0$. For $\xi > 1$, the LPE stretching is a bit easier than for a neutral polymer owing to the internal electrostatic repulsion. However, for example for $\xi = 2.31$, we measure an appreciable entropy loss of about 10 $k_{\mathrm{B}}T$ per LPE chain for the extension $L_r \simeq 7.5$ nm. This loss in the chain conformation entropy needs to be compensated by the handshake and forthcoming release of counterions in order to establish the coexistence between associated and free states. For this particular example, thus 20 $k_{\mathrm{B}}T$ are needed to be compensated in total for both chains. For $\xi = 2.31$, we estimated 5 $k_{\mathrm{B}}T$ per released ion, so that about four counterions were required. Glancing back at Fig. 4.4, however, we see that for $\xi = 2.31$ in total seven ions are released at the handshake. The apparent discrepancy can be reconciled by investigating the number of condensed and released counterions during stretching, see Fig. 4.6(b). Apparently, ions are released during stretching, very likely due to the increasing effective LPE length (and decreasing charge density) during stretching. At the relevant stretched state at $R_{ee} = L_r \simeq 7.5$ nm for $\xi = 2.31$, a mean of 1.5 ions per chain (thus, three in total) are released. In other words, only four counterions are released in the actual handshake, in agreement with the needed compensation stretching penalty mentioned above. These subtle structural effects on a single-ion level are important for a quantitative interpretation of the transient states in complexation. The free energy barrier between the coil and extended state must then be clearly attributed to the entropy of intermediate stretching.

4.4 Results for LPE-HSA interaction

LPE-HSA binding complex and stoichiometry

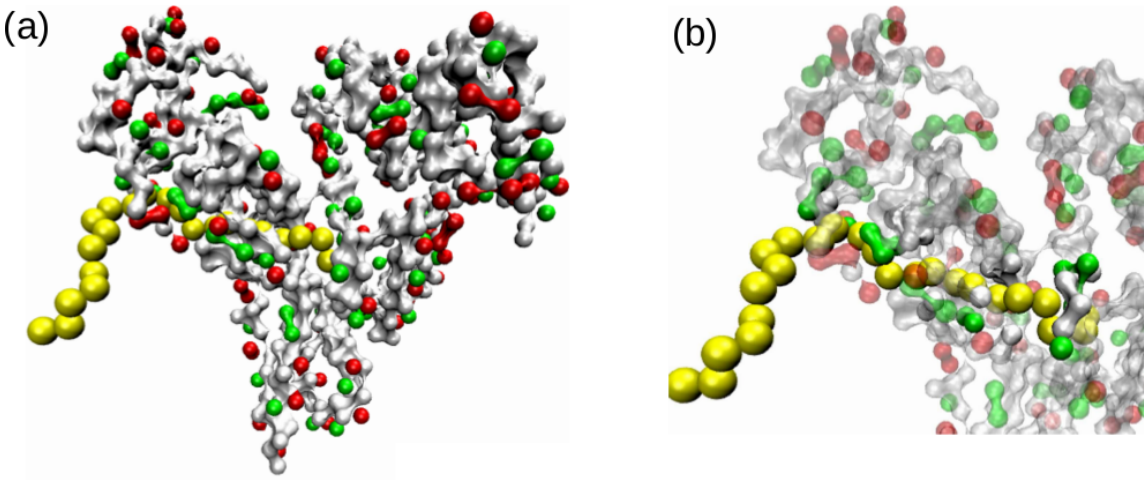

Figure 4.7: (a) Representative computer simulation snapshot of the total LPE-HSA complex. (b) Magnification of the binding site: LPE (yellow string of beads) is bound near the Sudlow II site. The amino acid beads that directly participate in the binding (defined by being within 0.5 nm distance to LPE on average) are depicted by the opaque spheres. The rest of the HSA structure is distinguished by a transparent surface plot. Electrostatically neutral HSA beads are colored white, positive beads are green, and negative beads are red.

Our computer simulations demonstrate that HSA binds with only one LPE chain, independent of temperature, salt concentration, and the molar ratio in the considered parameter ranges. This reconfirms the result obtained previously by experiment [132]. A representative simulation snapshot of the bound complex with one LPE is presented in Fig. 4.7. From a thorough screening of our simulation trajectories, it emerges that this structure is highly reproducible and assumed in 80% of the simulation time. It is hence a highly stable and probable configuration. Additional analysis reveals that the LPE chain spans the sub-domains II A, III A, and III B, involving the Sudlow II binding site. As expected for a negatively charged polyelectrolyte we find that it favorably binds positively charged amino acids, arginine (R) and lysine (K) at positions R410, R484, R485, R413, R538, K541, K199, and K195, see also the green opaque spheres in Fig. 4.7. This is certainly a central result of the present analysis in as much as it defines the precise location of the binding of a highly charged molecule as LPE.

To demonstrate that only one LPE forms a complex with HSA, the running coordination number $n(r)$ of LPE around HSA is shown in Fig. 4.8 for molar ratios $x = 1$, 2, 6, and 10. The quantity $n(r)$ is the total number of LPE-molecules around a given HSA as a function of distance. The plateau of the curves between separations of $r = 4$ and 6 nm just above

the average value of the HSA radius is a proof that the binding number does not exceed one, irrespective of the molar ratio. Only at larger distances $n(r)$ increases beyond unity since here the entire solution is explored. We find qualitatively similar results for the other investigated salt concentrations and temperatures. This finding again is in direct agreement with the previous experimental results [132].

It is furthermore interesting to see the temporal evolution of the complex of HSA with LPE. The LPE chain slides along the Sudlow II site much in a way of threading through an orifice. This fact demonstrates the strong binding of LPE by this side. On the other hand, the threading through this site leads to a strongly increased number of configurations of the complex and thus increases the entropy of the complex. This fact certainly leads to the binding of the LPE-chain at the Sudlow II site and not on other positive patches on the surface of HSA.

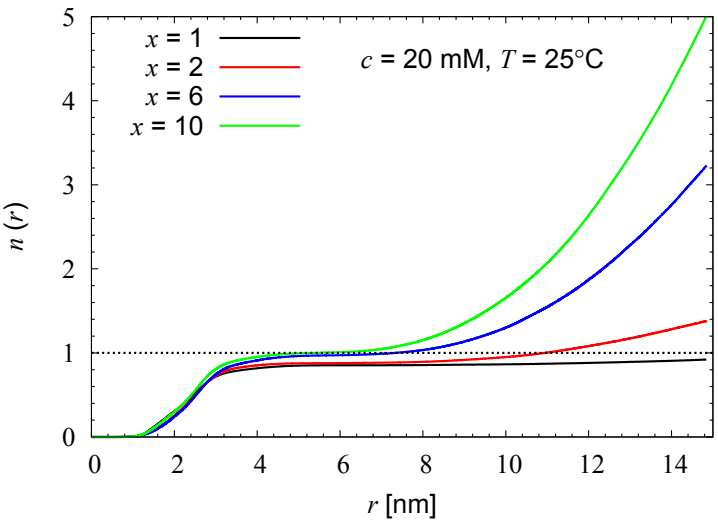

Figure 4.8: Running coordination number $n(r)$ of the LPE chains around HSA versus their center-of-mass distance r at a temperature of 25°, a salt concentration of 20 mM, and molar ratios $x = c_{\mathrm{LPE}}/c_{\mathrm{HSA}} = 1$, 2, 6, and 10, see the legend. In all cases roughly one LPE chain (horizontal black dotted line) is bound to HSA.

LPE-HSA binding affinity

Our simulations allow us to calculate the free energy profiles (potential of mean force) along the LPE-HSA distance coordinate. Examples for this interaction free energy $G(r)$ between a single uncomplexed HSA and one LPE at two salt concentrations are presented in Fig. 4.9. For larger distances of the approach, $r \simeq 7$ nm, a small repulsive barrier can be observed stemming from the monopole charge repulsion which dominates for large separations as expected. The barrier decreases and shifts slightly to shorter distances with higher salt

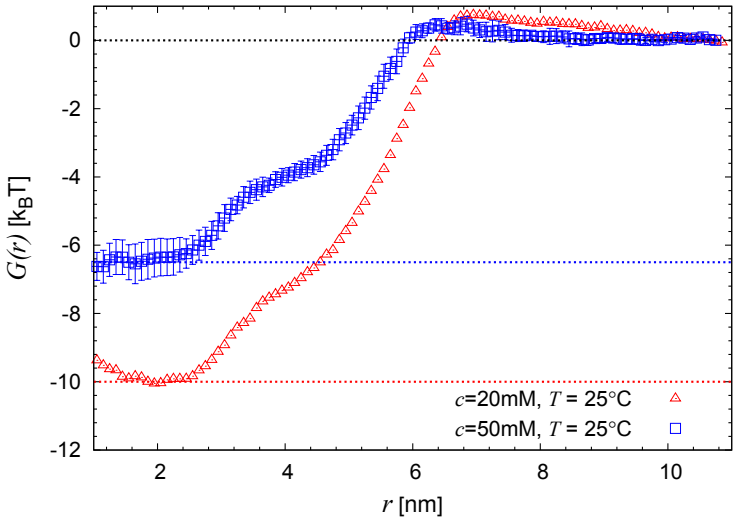

Figure 4.9: Free energy profile (or potential of mean force) $G(r)$ between PAA and HSA versus their center-of-mass distance r at a temperature of 25° and for 20 mM (red) and 50 mM (blue) salt concentrations. The binding free energy ΔG^{sim} derived from the simulation can be read off as the difference between the zero free energy reference state at far separation (horizontal black dotted line) and the global minimum representing the bound state (horizontal blue and red dotted lines).

Table 4.1: The calculated standard binding free energy from the simulations $\Delta G_{\mathrm{b}}^{\mathrm{sim}}$ in comparison with the experimental ones [132] $\Delta G_{\mathrm{b}}^{\mathrm{exp}}$ at various salt concentrations and temperatures in units of kJ mol^{-1}. $\Delta G_{\mathrm{b}}^{\mathrm{sim}}$ is the direct output from the simulations which has to be corrected by ΔG^{corr} for the binding volume V_b to obtain the standard free energy of binding.

Conditions	ΔG^{sim} (KJ mol^{-1})	V_b (nm^3)	ΔG^{corr} (KJ mol^{-1})	$\Delta G_{\mathrm{b}}^{\mathrm{sim}}$ (KJ mol^{-1})	$\Delta G_{\mathrm{b}}^{\mathrm{exp}}$ (KJ mol^{-1})
20 mM, 25°	-24.8±4.0	3.0	-1.5	-26.3±4.0	-27.9±0.2
20 mM, 37°	-25.1±3.6	5.9	-3.1	-28.2± 3.6	-29.2±0.2
50 mM, 25°	-16.1±1.0	16.0	-5.7	-21.8±1.0	-23.5±0.5
50 mM, 37°	-18.9±0.5	7.5	-3.9	-22.8±0.5	-26.2±0.2

concentration. At about $r \simeq 6$ nm, the onset of a strong attraction takes place until a global minimum is observed at a closer approach at about $r = 2$ nm. The onset of attraction occurs right at values comparable to half of the contour length of the LPE chain at which one of its ends is first able to come in contact with the HSA surface. We never found a stable free energy minimum for the adsorption of a second LPE. This is due to a too strong monopole charge repulsion and the covering of the high-potential binding spot by the firstly bound LPE.

For the stable HSA–LPE complex, the binding free energy ΔG^{sim} can be calculated from the difference in the global minimum and the reference free energy at large distances (horizontal lines in Fig. 4.9). The values of the simulation binding free energy, corrected to yield the standard free energy of binding from the simulations $\Delta G_{\mathrm{b}}^{\mathrm{sim}}$ (See Sec. 3.2). At various salt concentrations and temperatures, we find $\Delta G_{\mathrm{b}}^{\mathrm{sim}}$ in a good agreement with the

previous experiments with the largest deviation of only 13% for the case of 50 mM salt at a temperature of 37° [132]. As in the experiments, the binding affinity decreases in the simulations with higher salt concentrations and increases with increasing temperature [132]. The relevant results are illustrated in Tab. 4.1. The highly quantitative description using the simulations, however, is actually somewhat surprising given the simplicity of the underlying model and the negligence of hydration effects and should be discussed with caution. However, we take it as a strong indication that relatively generic electrostatic interactions rule the complexation process and hydration contributions (such as hydrophobic or van der Waals (vdW) attractions) are rather small.

Released counterions and LPE-HSA binding

In order to test our hypothesis introduced above that the binding free energy is essentially dominated by the entropy of released counterions from the LPE chain and/or positive patches on HSA, we have counted the number of released ions upon complexation. In brief, we define an ion as ´condensed' if it is located in the first bound layer near a charged HSA or LPE monomer, defined by a cut-off radius of 0.5 nm. Hence, the number of released ions is calculated as the difference in the average number of condensed ions in the fully separated and the stable bound states. As indicated in Fig. 4.10, for a temperature of 25° and 20 mM and 50 mM salt concentrations, our analysis shows that on average indeed 2.5 condensed ions are diluted away into the bulk upon complexation. This is indeed in good agreement with the Record–Lohman-analysis (See Sec. 3.1) of the experimental data discussed [132].

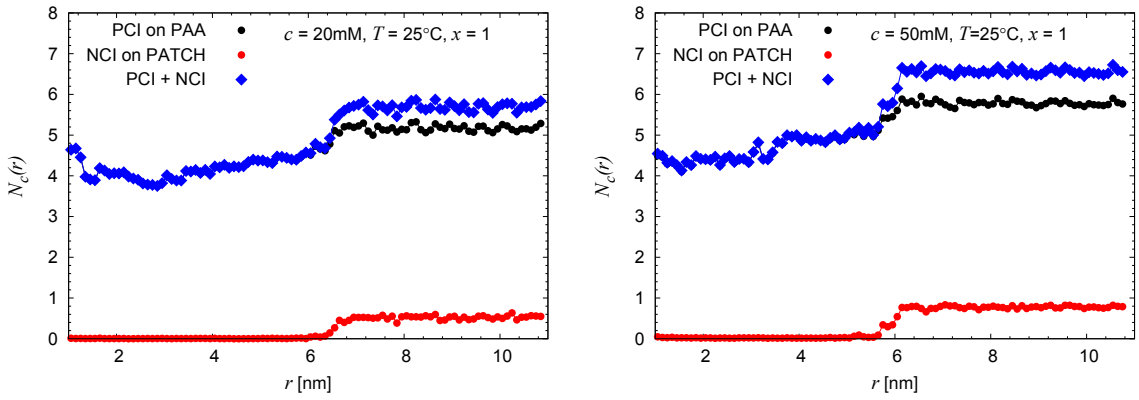

Figure 4.10: Number of positive condensed ions(PCI) and negative condensed ions(NCI) versus distance.

Deeper inspection shows that 2 of those ions come from LPE, at which they were bound in a high density state. If we now just consider the LPE-condensed ions and their average concentration in the bound state $c_{\rm dense} \simeq 1.5 \pm 0.5$ mol L^{-1}, this implies that favorable entropy contributions of about $\simeq k_{\rm B}T \ln(c_{\rm dense}/c_s) = 4.3 \pm 0.4$ and $3.4 \pm 0.4\ k_{\rm B}T$ are gained

per ion upon their release into 20 mM and 50 mM bulk concentrations, respectively. The total release free energies estimated by this analysis are thus roughly -21 ± 2 and 17 ± 2 kJ mol^{-1} for 20 mM and 50 mM salt concentrations, respectively, which are close to the binding free energies from both experimental data and from simulations [132]. Hence, the binding of LPE is to a great part ruled by a counterion release mechanism and entropy. We note, however, that the matching of these numbers may be fortunate since other non-negligible interactions such as (repulsive) chain entropy, vdW attractions, and multipolar charge interactions beyond the bound ion layer (that is, from screening ions), all present in both simulation and the experiment, have been neglected in this simple counterion release concept. The present comparison with experimental data, however, indicates that these contributions are of comparable magnitude and cancel each other roughly for the present system.

Evidently, we obtained the leading contribution of the ions directly condensed on the LPE chain. Hence, the estimate of the entropy of counterion release given above should be considered a lower bound for the absolute entropy contribution. Other contributions not included in the theoretical analysis apparently lead to experimental entropies that are higher by a factor of 2-3. The good agreement between the measured and the calculated ΔG_b, however, demonstrates that these additional entropic contributions are canceled out by an enthalpic contribution of equal magnitude. This "enthalpy– entropy compensation" is well-known for various processes such as solute hydration, protein folding, or protein association [151, 152]. The present comparison of theory and experiment allows us to discern among these terms and the leading contribution to ΔG_b.

4.5 Summary and concluding remarks

In summary, we have studied LPE structure variations and the resultant PMF profiles along the LPE–LPE center-of-mass reaction coordinate for LPE pair complexation with a focus on intermediate association ranges for various LPE charge densities. For charge densities above the condensation threshold, we observed and analyzed in detail a (fast) sliding-rod-like process preceding the LPE complexation. We introduced an abstract model leading to an analytical expression for the PMF. The latter predicts a PMF virtually linear in center-of-mass distance starting at the onset of complexation of the first 'handshake' until collapsing into the final complex, in good agreement with the computer simulations. Furthermore, a detailed inspection of the mean force profile uncovered a discontinuity at the onset of complex formation, which is also embodied as a jump in numerous other simulation measures. We demonstrated that the discontinuity can be attributed to the presence of a free-energy barrier

stemming from cooperative counterion-release effects and single LPE stretching entropy. Perhaps even more complex transient behavior can be expected when tuning chain stiffness, chain length, counterion valency, and the strength of the electrostatic interaction [153, 154], or including the action of explicit solvent [155, 156, 157].

For the LPE-HSA system, we demonstrate that the binding of LPE takes place at the Sudlow II site. Experiments [132] for a series of salt concentrations between 20 mM and 100 mM show that the dependence of binding affinity ΔG_{b} on ionic strengths is mainly determined by the counterion release mechanism and can be described by the Record–Lohman relationship (see Sec. 3.1). This is in a nice agreement with the simulations presented here. Thus, the application of computer simulation is now capable of solving biochemical problems of direct medical importance.

5 Charged dendrimers revisited: effective charge and surface potentials of dendritic polyglycerol sulfate

This chapter we investigate key electrostatic features of charged dendrimers at hand of the biomedically important dPGS macromolecules using multi-scale computer simulations and Zetasizer experiments. In our simulation study, we first develop an effective mesoscale Hamiltonian specific to dPGS based on input from all-atom, explicit-water simulations of dPGS of low generation. Employing this in coarse-grained, implicit-solvent/explicit-salt Langevin dynamics simulations, we then study dPGS structural and electrostatic properties up to the sixth generation. The most important outcome of our dendrimer simulation results in important conclusions of effective net charges and corresponding radii, surface charge densities, and surface potentials of dPGS. The relevant results are validated after a comparison to the analytical theory and experiments. Note that the descriptions and figures in this chapter are taken almost literally from our previous publication [158].

5.1 Models and methods

All-atom model and explicit-water MD simulations

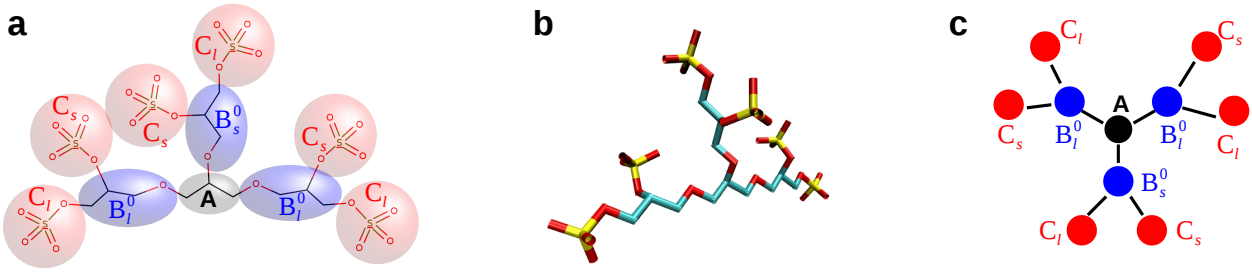

Figure 5.1: (a) Chemical formula, (b) atomistic structure, and (c) coarse-grained (CG) structure sketch of the zeroth generation G_0–dPGS molecule. In panel (a), we depict the atomistic subunits C_3H_5, C_3H_7O, and SO_4^- corresponding to the CG bead types A, B_i, and C_i ($i = s, l$) in panel (c) by the black, blue, red colored regions, respectively.

We start the development of the dPGS CG force–field from fully atomistic (explicit-water) MD simulations of dPGS of generations $n = 0$ and 1 (i.e., G_0 and G_1) from which effective intra-bead potentials are derived. The constituting elements are the initiator core C_3H_5, repeating side chain units C_3H_5O, as well as the terminal sulfate groups, see the exemplary

chemical structure of G_0, in Fig. 1. All our simulations are carried out by the GROMACS 4.5.4 software package [159], where the GROMOS 45a3 force field [160] is applied. The latter is optimized to model lipids with long aliphatic chains or branches, which makes it an appropriate force field to model dPGS. The water is represented by the (SPC/E) model [161]. The partial charges of dPGS are calculated according to the Gaussian 09 software [162] with the cc-PVTZ DFT basis set and used here in combination with the GROMOS 45a3 force field. The assigned partial charges among the glycerol groups stay close to the re-optimized parameters for ethers. [163] And those for the sulfate group agree with recent work [164] which have been applied, for instance, in the simulation of sodium dodecyl sulfate micelles. [165]

The initial configurations of G_0 and G_1-dPGS are constructed in vacuum with the program ChemDraw [166]. A single dendrimer is then placed in the center of a cubic simulation cell with an initial side length $L = 7.9$ nm with periodic boundary conditions in all three directions. The dendrimer is subsequently hydrated with 16543 water molecules. To preserve the overall charge neutrality of G_0 and G_1, six or twelve Na^+-counterions are added, respectively. The electrostatic interactions are calculated via the PME (See Sec. 3.2) [105] summation where the long-range potential is evaluated in the reciprocal space using the FFT with a grid spacing of 0.16 nm and a cubic interpolation of fourth order. A cut-off radius of 1 nm is defined for both PME summation and van der Waals real-space interactions. After a 100 ns equilibration in the isobaric NPT ensemble at conditions of $P = 1$ bar and $T = 310$ K, a production run of 1 μs generates a working trajectory in a canonical NVT simulation. We utilize the Berendsen thermostat and the Rahman-Parrinello barostat (See Sec. 3.2). To integrate Newton's equation of motion (See Sec. 3.2) we employ the leap-frog algorithm with a time step of 2 fs.

Coarse-graining procedure

For our CG model we now define three coarse-grained bead types A, B, and C, chosen to be located at the center-of-mass position of repeating units, cf. Fig. 1. While type A simply models the central core unit (C_3H_5), the natural choice for B and C is reflected in the chemical formula $C_3H_5(C_3H_5S_2O_9)_3$ for G_0-dPGS which defines the repeating units C_3H_5O as type B and the terminal group SO_4 as monomer C. As one can see in the chemical structure in Fig. 1, the intra-bead potentials between B and C beads (as well as between B and B beads in higher generations) depend on how the corresponding atomistic groups are connected: in a given triplet of units around a connecting central hub unit, two units feature an extra bond so that it is needed to introduce 'short' and 'long' bead types B and C for intermediate branching cycles $m = 0..n$. In the following we therefore distinguish between

B_s^m and B_l^m as well as C_s and C_l beads, respectively. Hence, for the coarse-grained force field we need to define bond potentials of types A-B_j^0, B_i^m-B_j^{m+1}, B_i^n-C_j, with $i = s, l$ and angle potentials for all relevant triplets, for example, A-B_i^0-B_j^1, B_i^m-B_j^{m+1}-B_k^{m+2}, B_i^{m+1}-B_j^m-B_k^{m+1}, B_i^{n-1}-B_j^n-C_k, etc. Note that there must be 'up-down' symmetry in the potentials, e.g., B_i^m-B_j^{m+1}=B_i^m-B_j^{m-1} for the bond potentials and analogous rules for the angular potentials. Finally, non-bonded inter-bead interactions have to be defined between types A, B, and C.

We employ harmonic potentials for the intramolecular (bond and angular) interactions and use the LJ interaction for all inter-bead potentials. Additionally, the beads of type C and ions carry charges. Hence, the CG force field can be formally summarized by the CG Hamiltonian

$$\begin{aligned} U^{\mathrm{CG}} &= \sum_{\text{bonds}} \frac{1}{2} k_b (l - l_0)^2 + \sum_{\text{angle}} \frac{1}{2} k_a (\theta - \theta_0)^2 \\ &+ \sum_{i<j} 4\epsilon_{ij} \left[\left(\frac{\sigma_{ij}}{r_{ij}} \right)^{12} - \left(\frac{\sigma_{ij}}{r_{ij}} \right)^{6} \right] + U_{\mathrm{elec}}. \end{aligned} \tag{5.1}$$

where r_{ij} is the bead–bead distance, k_b and k_a are the bond and angular spring constants, respectively, l represents the distance between consecutive beads and l_0 is the equilibrium bond length. The variable θ refers to the angle formed by a triplet of consecutive beads and θ_0 is the equilibrium value. Only the C bead, representing the terminal sulfate group, carries a bare Coulomb charge $q_s = -e$. It follows that the net charge valency for the CG dPGS molecule of generation n is $Z_{\mathrm{bar}} = -6(2^{n+1} - 2^n)$ and thus the terminal beads number $N_{\mathrm{ter}} = |Z_{\mathrm{bar}}|$. The electrostatic interactions for all charged beads (type C and ions) are included in U_{elec}, via the Coulomb law

$$\beta U_{\mathrm{elec}} = \sum_{i=1}^{N_{\mathrm{ter}}+N_{\mathrm{ion}}} \sum_{j=1, j\neq i}^{N_{\mathrm{ter}}+N_{\mathrm{ion}}} \frac{l_B}{2 r_{ij}}. \tag{5.2}$$

The variable $l_{\mathrm{B}} = e^2/(4\pi\epsilon_0\epsilon_r k_{\mathrm{B}} T)$ stands for the Bjerrum length, which is $l_{\mathrm{B}} = 0.7$ nm in this study at body temperature $T = 310$ K and for water with a permittivity constant $\epsilon_r = 78.2$, N_{ion} denotes the number of ions, e is the elementary charge, and ϵ_0 is the permittivity of vacuum.

We derive the bonded potentials by Boltzmann–inverting the corresponding target spatial distribution functions of the beads $f(x)$ we obtain from the atomistic MD simulation, via

$$U(x) = -k_{\mathrm{B}} T \ln f(x), \tag{5.3}$$

where x is either a bond length or angle variable and $f(x)$ is an equilibrium average over the

fluctuations of all identical groups in the dendrimer. All potentials involving beads A and C are derived from simulations of G_0. All potentials involving beads only of type B are derived from simulations of G_1 as B-B bonds are absent in G_0. The results and final parameters of the bonded CG potentials are discussed and summarized in the next section.

The extraction of the non-bonded A-A, B-B and C-C potentials directly from the atomistic MD simulation of G_0 or G_1-dPGS is very difficult due to the convoluted spatial structure of the dendritic dPGS. Therefore, a mapping using the (IBI) scheme [167, 168] is out of reach. We therefore resort to the simplest approximation and perform explicit-water simulations of a one-component fluid of isolated A, B, and C monomers in explicit water, respectively, at relatively high dilution. The respective non-bonded pair potentials are then obtained by the simple Boltzmann–inversion according to Eq. (3), where $f(x)$ then simply represents the radial distribution function. The charged sulfate monomers corresponding to subunit C are protonated to separate out approximately the electrostatic monopole repulsion which later in the CG simulation are added again. The partial charges of the A, B, C chemical subunits are calculated according to the Gaussian 09 software [162] with the cc-PVTZ DFT basis set, and used here in combination with the GROMOS 45a3 force field. We set the concentration of the one-component bead fluid to $c \sim 400$ mM that is chosen high enough to obtain sufficient sampling and low enough to avoid large many-body effects and possibly aggregated states. After obtaining the LJ parameters ϵ_{ii} and σ_{ii} by fitting the LJ potentials to the obtained effective interaction (see next section) for the three subunits, i =A,B,C, the corresponding values for the cross interactions are obtained by the conventional Lorentz-Berthelot mixing rules, i.e., $\sigma_{ij} = (\sigma_{ii} + \sigma_{jj})/2$ and $\epsilon_{ij} = \sqrt{\epsilon_{ii}\epsilon_{jj}}$.

The simple Boltzmann-inversion scheme for the inter-bead potentials that neglects many-body and connectivity effects is approximative. However, the excluded-volume part of the LJ is hardly affected by this treatment, only the attractive (van der Waals) part of the LJ interaction is expected to be affected by the many-body contributions. (Note that most CG simulations in the literature do not include the van der Waals attraction.) Therefore, we tested the influence of varying the bead ϵ_{ii} on some of the key structural and electrostatic of the dendrimers. The results show hardly any influence on the results for dispersion variations in a reasonable window and therefore leave our results quantitatively essentially unchanged.

5.2 Coarse-grained potentials

Selected results of our mapping procedure are plotted in Fig. 5.2. As we see in panels (a) to (c), the intra-bond potentials can be fitted well by a harmonic function. We find that the asymmetry in the glycerol repeat unit leads to an equilibrium bond length that differs

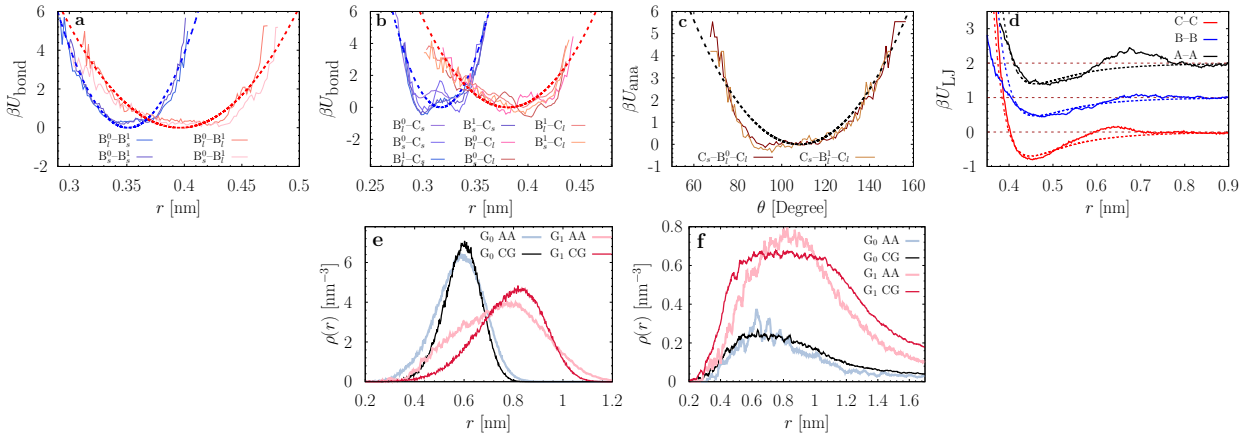

Figure 5.2: The (a) B_i^0-B_j^1 bond, (b) B_i^m-C_j bond, (c) C_i-B_j^m-C_k angular ($m = 0$ for G_0 and $m = 1$ for G_1), and (d) A-A/B-B/C-C effective inter-bead potentials extracted from the all-atom MD simulations (AA; solid lines). The dashed lines are the fits according to the coarse-grained (CG) Hamiltonian Eq. (5.1). For the atomistic simulations, the coordinate r is defined as the bead-bead center-of-mass distance. The indices $i, j = s, l$ distinguish between beads having short or long bond connections in the molecular structure, respectively. In the bottom panels the density distributions of the terminal sulfate groups (e) and counterions (f) around the dPGS center-of-mass from atomistic and CG simulations are compared for the G_0 and G_1 dPGS, respectively. The simulations were performed at salt concentrations $c = 30$ mM for G_0 and $c = 50$ mM for G_1.

if 'short' or 'long' beads are connected at the upper cycle branch $m + 1$. The shift between the bond lengths corresponds to a single covalent bond length on the Ångstrom scale. The structure asymmetry is also reflected in the angular potential $U_{\rm ana}$, although in that case the effect is less notable as compared to the bond potential. As shown in Fig. 5.2(c), the angle θ formed by a triplet of monomers C–B–C has a distribution ranging from 60° to 150° and is thus relatively broad when compared to typical atomistic potentials. Note that in all of the previous CG dendrimers models angular potentials were typically neglected. All bonded bead potentials are summarized in Table 1.

In Fig. 5.2(d), we present the non-bonded LJ potentials between pairwise groups A-A, B-B, and C-C. At small separation, $r \lesssim 0.4$ nm, a strong repulsion demonstrates the excluded–volume interaction, while in the intermediate distance $r \simeq 0.6$ to 0.7 nm, a small energy barrier signifies effects of the first hydration shell around the beads. We neglect these small barriers and fit the curve via the LJ potentials, cf. the dashed lines in Fig. 5.2 (d). The final parameters for the CG ϵ_{ii} and σ_{ii} values for all three bead types are very similar. This can be seen as a justification to set a generic LJ potential for all CG beads as typically utilized in previous CG studies of monomer-resolved dendrimers [36, 169, 170, 171]. We complement the CG force-field by effective potentials for a symmetric monovalent salt where, for simplicity, we chose the same LJ parameters as for the charged C bead. The corresponding LJ size

for the ions is actually the same as for the effective CG sodium-chloride cross interaction in water [172, 173], so it seems a reasonable choice to model a simple monovalent salt. The relatively small energy parameter ϵ_{LJ} parameter of 0.1 kJ/mol models hard-sphere like ions without any strong ion pairing behavior. [173] The parameters for the non-bonded interaction are summarized in Table 5.2.

In order to further scrutinize the validity of the CG force field, we compare density profiles of the terminal sulfate groups, Fig. 5.2(e), and the cations, Fig. 5.2(f), extracted from atomistic and CG simulations (see next section for methods) of generation $n = 0$ and 1. A good agreement is reached between the two approaches in both profiles for both generations, consolidating earlier conclusion on the validity of CG force field for charged dendrimers [174]. For G_1, we find that the width of the distribution of the terminal groups appears to be a bit narrower in the CG force field. Yet, the global structure represented by the location of the density peaks appears to be similar for both approaches. This similarity applies to the counterion distribution as well, indicated by the density peak at $r \sim 0.82$ nm produced by both levels of modeling.

Table 5.1: Parameter for the CG dPGS bonded potentials. The subscript s and l refers to B_i beads with a long or short glycerol arm, respectively. $m = 0$ to n denominates the intermediate branching cycle for a given generation n.

group	k_b ($k_{\mathrm{B}}T\,\mathrm{nm}^{-2}$)	l_0 (nm)	k_a ($k_{\mathrm{B}}T\,\mathrm{deg}^{-2}$)	θ (deg)
A–B_l^0	1381	0.380	–	–
A–B_s^0	5100	0.337	–	–
$B_{s,l}^m$–B_l^{m+1}	1052	0.395	–	–
$B_{s,l}^m$–B_s^{m+1}	3105	0.351	–	–
$B_{s,l}^n$–C_l	1633	0.380	–	–
$B_{s,l}^n$–C_s	6160	0.312	–	–
$B_{s,l}^0$–A–$B_{s,l}^0$	–	–	0.003	115
$B_{s,l}^1$–$B_{s,l}^0$–A	–	–	0.003	115
$B_{s,l}$–$B_{s,l}$–$B_{s,l}$	–	–	0.003	115
$C_{s,l}$–$B_{s,l}^n$–$B_{s,l}^{n-1}$	–	–	0.003	121
$C_{s,l}$–$B_{s,l}^0$–A	–	–	0.003	121
C_s – $B_{s,l}^n$– C_l	–	–	0.005	108

Table 5.2: CG dPGS nonbonded potential.

group	σ_{LJ} (nm)	ϵ_{LJ} (k_{B}T)
A	0.41	0.60
B	0.41	0.53
C	0.40	0.70
cation	0.40	0.10
anion	0.40	0.10

5.3 Coarse-grained simulations: dPGS effective charge and radius

Having established a CG force field, all generations n of dPGS can be now readily constructed. Higher generations G_n with index $n > 0$ are created by iteratively bonding two extra glycerol units to the original one (dendritic segment) on the outer shell of generation G_{n-1}. This Cayley tree-like [175] structure gives an exponentially growing of the polymerization $N_g = 3(2^{n+1} - 1) + 1$ with its generation index n, which thereby leads to the sulfate group number $N_{\mathrm{ter}} = 6(2^{n+1} - 2^n)$ and the gross number $N_{\mathrm{dP}} = 6 \times 2^{n+1} - 2$ of the CG segments. Note the above structure only fits to a perfect dendrimer, whereas an imperfect dendrimer bears a small number of linear segments that corresponds to most experimental dPGS realizations [176]. In our work we investigate seven different generations $n = 0$ up to $n = 6$, depicted and with some features summarized in Table 5.4.

For the CG simulations the dPGS macromolecules are placed in a cubic box with a side length of $L = 35$ nm with periodic boundary conditions in all three directions. We treat the solvent implicitly via a uniform dielectric background, however, ions are treated explicitly to account for ionic correlation effects. In view of the charge status of dPGS, a number of monovalent counterions, $n_c = 6(2^{n+1} - 2^n)$, is added to maintain an electroneutral system. Apart from the counterions, in all simulations, dPGS is immersed in a salt solution with $N_i =$ 257 to 5140 pairs of monovalent cations and anions, resulting into bulk salt concentrations from $c_0 = N_i/L^3 \simeq 10$ mM to 200 mM. The initial dendrimer configuration is assembled according to the equilibrium bond length l_0 and angle θ_0 appeared in Eq. (5.1).

We perform Langevin dynamics simulations ((See Sec. 3.2)) on CG dPGS of generation number ranging from 0 to 6 also using the GROMACS package. All the implicit water

simulations used the second-order SD integrator in GROMACS with the friction in the Langevin equation set with a time constant of $\tau_t = 1$ ps and integration time of 2 fs. We set all CG beads to have a small mass of $m_i = 0.5$ amu to decrease inertial effects and lower the intrinsic viscosity (i.e., internal relaxation time) of the dPGS. Equilibrium properties, as investigated in this work, are not affected by any reasonable mass choices as long as the simulations are ergodic. With an increasing number of the terminal beads the electrostatic interaction becomes more profound and the cut-off radius for the PME summation and short-range van der Waals interactions is extended to $r_{\text{cut}} = 4$ nm as compared to the above atomistic simulation. The choice of the cutoff is verified by reference simulations with increased cutoff value $r_{\text{cut}} = 6.0$ nm. Unless specifically stated otherwise, the temperature was set to 310 K as the default. The static dielectric constant of the solvent is $\epsilon_r = 78.2$ at this temperature. After energy minimization of the initial structure and a 1 ns equilibration period, the production run of a NVT simulation lasts around 60 ns. That time has been proven to be sufficient for equilibrium sampling for all generations as in detail verified by scrutinizing relaxation times and time unit scalings between all-atom and CG simulations.

dPGS effective charge and radius

For the definition of the effective charge of a dendrimer (and thus the effective surface potential) we take the basic DH theory for the radial electrostatic potential distribution (See Sec. 3.2) around a charged sphere with radius r_{eff} and valency Z_{eff} as reference [20],

$$e\beta\phi_{\text{DH}}(r) = Z_{\text{eff}} l_B \frac{e^{\kappa r_{\text{eff}}}}{1+\kappa r_{\text{eff}}} \frac{e^{-\kappa r}}{r}, \tag{5.4}$$

where $\kappa = \sqrt{8\pi l_{\text{B}} c_0}$ is the inverse Debye length for a symmetric, monovalent salt. This solution is derived with the Dirichlet boundary condition, *i.e.*, fixing the surface potential $\phi(r_{\text{eff}})$ and the one far away $\phi(\infty) = 0$. The DH potential usually works well in the region far from the colloid, where nonlinear effects, such as ion–ion correlations and condensation, become irrelevant. For the "correlated Stern layer" at the interface of the charged sphere, the electrostatic potential ϕ is expected to deviate strongly from the DH potential ϕ_{DH} and all nonlinear effects are adsorbed into the effective charge Z_{eff} (as, e.g., based on solutions of the full non-linear Poisson-Boltzmann theory [94, 177, 178, 20, 95]). By taking the logarithm of

eq. (5.4) and mapping directly on the far-field behavior of the electrostatic decay calculated in the simulation, the double-layer behavior can be quantified with high accuracy. [115] This provides also the basis to define the position of the Stern layer, or better expressed, the exact location r_{eff} of the interface between the diffusive double layer in the DH sense and the correlated condensed ion layers. The effective surface potential is then simply $\phi_0 = \phi_{\text{DH}}(r_{\text{eff}})$.

Experimental Materials and Methods

Table 5.3: Properties of dPGS of generation G_n in the experiments. The dPGS weight $M_{\text{n,dPGS}}$ is deduced from the respective core weight $M_{\text{n,dPG}}$ and sulfate group number N_{ter}. DS is the degree of sulfation, and PDI is the polydispersity index. η is the ζ-potential attained from the electrophoretic experiment.

Label	G_2	G_4	$G_{4.5}$	$G_{5.5}$
$M_{\text{n,dPG}}$ [kD]	2	7	10	20
PDI	1.7	1.7	1.5	1.2
DS [%]	100	100	99	98
N_{ter}	28	102	135	266
$M_{\text{n,dPGS}}$ [kD]	5	18	24	47
η [mV]	-47.71	-58.46	-58.73	-70.9

(dPG) was synthesized by anionic ring opening polymerization of glycidol [179]. (GPC) is empolyed to measure the number averaged molecular weight of the core $M_{\text{n,dPG}}$ and (PDI). Afterwards dPGS was prepared by the sulfation of dPG with SO_3-pyridine complex in (DMF) according to reported procedure [180]. The (DS) was determined by elemental analysis. Properties of dPGS in different generations are summarized in Tab. 5.3.

Size and ζ-potential (electrophoretic mobility) measurements were performed with a Zetasizer Nano ZS instrument (ZEN 3500, Malvern Instruments, Herrenberg, Germany) equipped with a 18 mW He-Ne laser (λ=633 nm). The molecule size r_{hd} was measured by DLS in UV-transparent disposable cuvettes (VWR, Germany) at a back scattering angle of 173° (See Sec. 3.3). The compounds were dissolved in 10 mM MOPS buffer (adding NaCl to adjust ionic strength to 10 mM) pH 7.4 at concentration of 1 mg/ml and were filtered through 0.8 μm polyethersulfone syringe filter (PALL, USA). Prior to measurement, each sample was equilibrated for 2 min at 37° and measured with 10 scans each lasting for 10 s. The stated values for the hydrodynamic diameter are the mean of three independent measurements. The electrophoretic mobility was measured at 5 mg/ml in the same buffer as above also in three

independent measurements. The solutions were filtered through 0.2 μm polyethersulfone syringe filter and equilibrated for 10 min at 37° in folded DTS 1060 capillary cells (Malvern, UK). The shown data for the ζ-potential in the resulting figure are based on the Henry function with the Ohshima approximation (See Sec. 3.3). The following reported ζ-potential are the mean of the three independent measurements.

5.4 Results and Discussion

Radius of gyration and asphericity

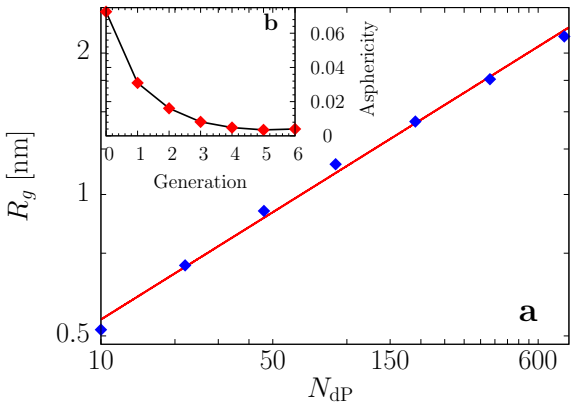

Figure 5.3: (a) Log–log plot of the radius of gyration R_g versus the total beads number N_{dP} for generations G_0 to G_6. The red line is the fitted power law function $R_g \sim N_{\mathrm{dP}}^{0.33}$ for all generations, while the dotted cyan line is a fitted power law function $R_g \sim N_{\mathrm{dP}}^{0.30}$ for generations G_2 to G_6 only. Inset (b): the asphericity parameter A (bottom panel) versus generation of the CG dPGS molecules.

The radius of gyration R_g (See Sec. 3.2) of the dPGS macromolecules as a function of generation n is summarized in Table 5.4. We find that R_g increases from 0.52 nm to 2.17 nm from G_0 to G_6. A linear behavior is revealed in a log–log plot of R_g in terms of the total number of the CG segments, N_{dP}, in Fig 5.3(a). Hence, the dPGS size follows the scaling law $R_g \sim N_{\mathrm{dP}}^{\nu}$, where we find the scaling exponent $\nu = 0.33$ if we fit all generations, while it decreases slightly to $\nu = 0.30$ if we only fit through the larger generations G_2 to G_6, cf. Fig 5.3(a). Such a scaling close to 1/3 is fully consistent with the now well established 'dense-core' picture of dendrimers, where details, however, can depend on the particular dendrimer architecture, see the deeper discussions in exemplary previous work. [36, 37, 54, 181].

In Fig 5.3(b), we plot the asphericity (See Sec. 3.2) versus the generation number. For all inspected generations we find values lower than A ~ 0.07, which suggests an almost perfect spherical shape for dPGS molecules. Larger generations show higher sphericity, very likely due to a more homogeneous distribution of the larger number of closer packed beads and a thus higher compactness. We show snapshots of the CG dendrimers for all investigated generations G_0 to G_6 in Table 5.4.

Table 5.4: Snapshots and Parameters for the CG dPGS model. In the dPGS snapshots on the top, red and orange beads depict the terminal charged and inner neutral beads, respectively. N_{dP} and N_{ter} stand for the total number of CG segments and terminal sulfate (C) beads for dPGS, respectively. We assign $Z_{\mathrm{bar}} = -N_{\mathrm{ter}}$, r_d and R_g as dPGS bare charge, radius, and radius of gyration, respectively. Z_{eff} and r_{eff} define the dPGS effective charge and corresponding radius. Via the inflection point criterion, [20, 182] we can calculate the inflection dPGS radius r_{inf} and accordingly the inflection dPGS charge Z_{inf}. Finally, $\sigma_d = Z_{\mathrm{bar}}/(4\pi r_d^2)$, $\sigma_{\mathrm{eff}} = Z_{\mathrm{eff}}/(4\pi r_{\mathrm{eff}}^2)$ and $\sigma_{\mathrm{inf}} = Z_{\mathrm{inf}}/(4\pi r_{\mathrm{inf}}^2)$ denote the bare, effective surface charge density, and inflection surface charge density, respectively. At the dPGS surface, we assign $\phi(r_{\mathrm{eff}})$ as the surface potential. All the estimates are made given a salt concentration of $c_0 = 10$ mM.

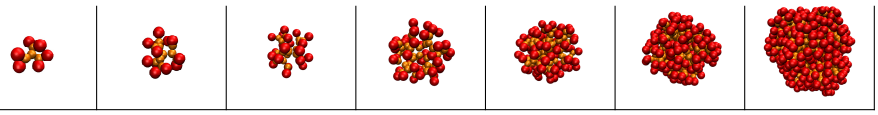

Label	G_0	G_1	G_2	G_3	G_4	G_5	G_6
MW [KDa]	0.79	1.72	4.10	8.32	16.77	33.67	68.00
N_{dP}	10	22	46	94	190	382	766
N_{ter}	6	12	24	48	96	192	384
Z_{bar} $[e]$	-6	-12	-24	-48	-96	-192	-384
R_g [nm]	0.52	0.71	0.92	1.16	1.43	1.76	2.17
r_d [nm]	0.65	0.83	1.10	1.35	1.65	2.05	2.55
σ_d $[e/\mathrm{nm}^{-2}]$	-1.28	-1.34	-1.58	-2.10	-2.81	-3.64	-4.70
r_{eff} [nm]	0.7	1.6	1.9	2.4	2.8	3.3	3.8
Z_{eff} $[e]$	-6.0	-7.3	-10.6	-14.3	-18.7	-24.5	-32.9
σ_{eff} $[e/\mathrm{nm}^{-2}]$	-0.97	-0.23	-0.23	-0.20	-0.19	-0.18	-0.18
$\phi(r_{\mathrm{eff}})$ $[k_{\mathrm{B}}T]$	-4.20	-2.12	-2.37	-2.22	-2.28	-2.25	-2.40
r_{inf} [nm]	–	1.1	1.5	1.8	2.1	2.6	3.1
Z_{inf} $[e]$	–	-9.9	-14.9	-22.9	-37.5	-52.2	-85.8
σ_{inf} $[e/\mathrm{nm}^{-2}]$	–	-0.65	-0.53	-0.56	-0.68	-0.62	-0.71

Density distributions and 'intrinsic' radius

Figure 5.4 shows the radial density distributions $\rho_i(r)$ of selected components with respect to the distance r to the dendrimer core bead. Fig 5.4(a) shows the distribution of the terminal sulfate beads. For the smaller generations $G < 4$, we find a single-peaked distribution, corresponding to the picture that most of the charged terminal beads stay on the molecular

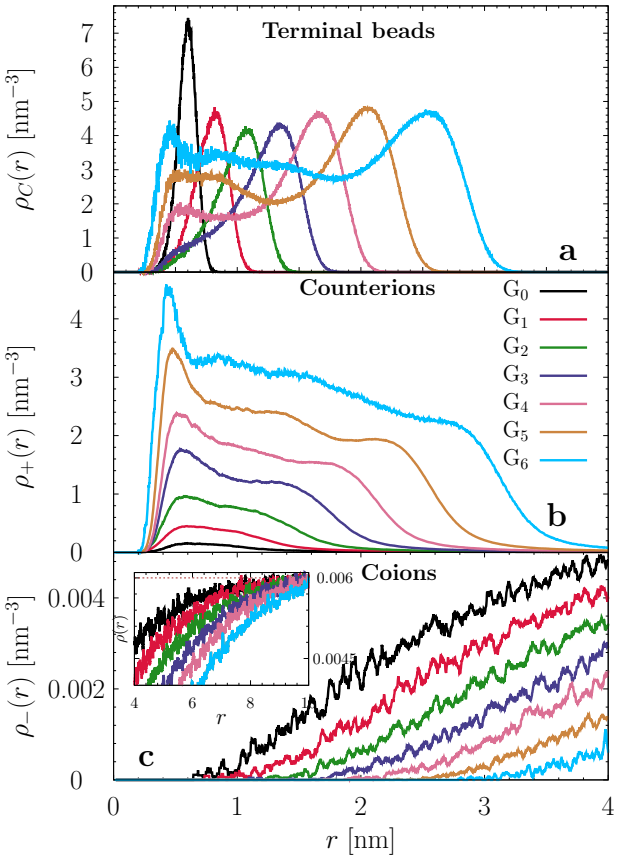

Figure 5.4: Radial density distribution $\rho_i(r)$ with respect to the dPGS core of (a) the terminal sulfate beads, i =C, (b) the cations (counterions; $i = +$), and (c) the anions (coions; $i = -$) for generations G_0 to G_6. In the inset of panel (c) we show the anion density profile at longer distance up to $r = 10$ nm, with the limiting bulk anion density c_0 marked by a dashed horizontal line.

surface [169, 170, 52, 181]. For the larger generations, however, a bimodal distribution signified by a small peak at $r \simeq 0.6$ nm appears, indicating a small number of dendrons backfolding toward the dendrimer core. The backfolding effect was already detected for other terminally-charged CG dendrimer models [169, 170, 52, 181] contributing to a dense-core in contrast to a dense-shell arrangement. [36] An 'intrinsic' dPGS radius r_d can be roughly deduced from the location of maximum density of the terminal groups. As implied in Fig. 5.4(a), we find a dPGS radius $r_d^{G_0} \simeq 0.6$ nm for generation G_0 increasing to $r_d^{G_6} \simeq 2.6$ nm for generation G_6. All values are summarized in Table 5.4.

The radial density $\rho_+(r)$ of the cations, shown in Fig. 5.4(b), is found to have qualitatively the expected response to the distribution of terminal beads and follows roughly the sulfate distribution. In particular, for all generations $\rho_+(r)$ decreases as expected in an exponential (Yukawa or DH-like) fashion to the bulk concentration for large distances. For closer

distances, $r \simeq r_d$ highly nonlinear effects are visible, e.g., in the response to the backfolding of the terminal beads we observe the enrichment of cations at $r \simeq 0.5$ nm inside the dPGS, corresponding to the lower sulfate peaks close to the core in Fig. 5.4(a). On the contrary and as expected, coions are repelled by the dPGS due to the electrostatic repulsion.

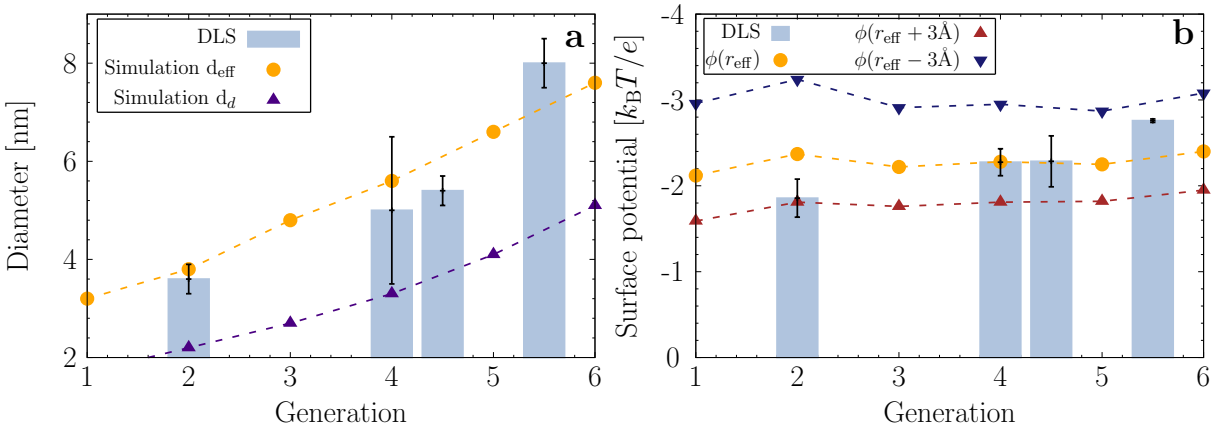

Figure 5.5: (a) Hydrodynamic diameter and (b) surface potential as determined via Zetasizer measurements (blue bars) and simulations (symbols; dashed lines are guided to the eye). In a) the simulation results are plotted for the intrinsic dPGS diameter $d_d = 2r_d$ and the effective diameter $d_{\text{eff}} = 2r_{\text{eff}}$. In b) simulation results are plotted for the effective surface potential $\phi_{\text{eff}} = \phi(r_{\text{eff}})$ at the location r_{eff} and that at one solvation layer shifted, i.e., $r_{\text{eff}} + 0.3$ nm and $r_{\text{eff}} - 0.3$ nm, respectively.

In Fig 5.5(a), we plot the hydrodynamic diameter measured via Zetasizer experiments of generation 2, 4, 4.5 and 5.5, respectively. As expected it increases with the molecular weight. A comparison to the dPGS size estimated from the sulfate peak in Fig. 5.4(a) from the simulation, $2r_d$, shows not a good agreement, probably because the correlated solvation layer, i.e., the Stern layer, is relatively thick and reaches out further into the bulk. The analysis in the next section, where an effective dPGS radius based on the ionic charge distribution is calculated, fully supports this conjecture.

Electrostatic properties of dPGS

Electrostatic potential, charge renormalization and effective 'charge' radius

From the ionic density profiles we can now in detail investigate local charge accumulation and electrostatic potential distributions (See Sec. 3.2). The accumulated number $N_+(r)$ of counterions and the locally total accumulated dPGS charge $Z_{\text{acc}}(r)$ (i.e., the local effective charge according to Eq. (3.51)) are presented in Fig 5.6(a) and Fig 5.6(b), respectively. It is

found that both $N_+(r)$ and $Z_{\rm acc}(r)$ increase sharply with distance r from the dPGS core due to the rising accumulation of charged beads. While $N_+(r)$ naturally rises, $Z_{\rm acc}(r)$ jumps to a maximum at a distance r_Z and drops gradually. At this distance, a large portion of the sulfate charges are neutralized by counterions. As implied by Fig 5.6(b), we find for instance that more than 70% of the charges at $r = r_Z$ for G_6 are compensated by bound counterions. This charge renormalization effect has been extensively studied at hand of simple charged spheres with smooth surfaces, and theories for the effective charge and size have been developed [20, 182, 94, 95, 96]. One important outcome is that one can define the critical location for counterion-condensation in terms of the inflection point in a plot of $Z_{\rm acc}$ as a function of the inverse radial distance $1/r$ [20, 182]. The equation $d^2 Z_{\rm acc}/d(1/r)^2|_{r=r_{\rm inf}} = 0$ leads to the inflection radius, $r_{\rm inf}$, within ions are deemed condensed. We marked $r_{\rm inf}$ by circle symbols for all generations in Fig 5.6. Note that $r_{\rm inf}$ is larger than r_Z and could be used to read off an effective charge size and charge of the macromolecule.

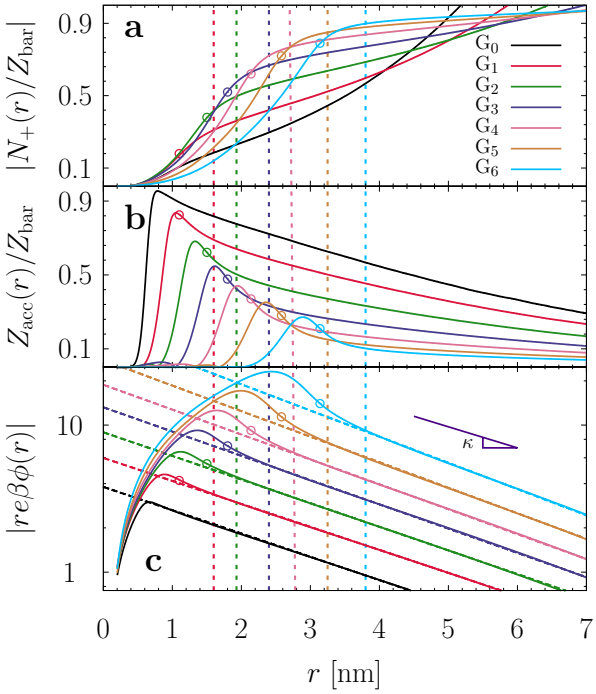

Figure 5.6: Distance–resolved (a) normalized running coordination number of counterions $N_+/Z_{\rm bar}$, (b) normalized accumulated effective charge $Z_{acc}(r)/Z_{\rm bar}$, (c) the product of distance r and dimensionless radial electrostatic potential $|e\beta\phi|$. We put a log-scale in (c) at the y-axis to examine the exponential decay. The long dashed line in (c) are fits according to the DH potential $\phi_{\rm DH}$, see Eq.(5.4). The vertical dashed lines signify the effective radius $r_{\rm eff}$ of dPGS, whereas the circles mark the inflection radius $r_{\rm inf}$. The dPGS generation for that plot ranges from 0 to 6 in condition of salt concentration $c_0 = 10$ mM. The exponential decay with standard inverse DH length $\kappa = 0.33$ nm^{-1} derived by DH theory is plot in panel (c) as a further comparison.

A more practical concept to define an effective size and charge is to quantitatively map the double-layer decay of the potential onto the basic DH-theory, Eq. (5.4). Fig. 5.6(c) plots the rescaled potential $|re\beta\phi|$ versus distance r in a log–linear scale. For the potential far away a homogeneously charged sphere, the DH potential $\phi_{\rm DH}$ with a renormalized charge should apply, yielding an exponential decay $e^{-\kappa(n)r}/r$ attributed to the electrostatic screening. The plot indeed shows the expected linear decay at large separations unambiguously for all presented dPGS with a slope as expected to be close to the standard inverse DH length $\kappa = 0.33$ nm^{-1} for the salt concentration $c_0 = 10$ mM. In detail, we find slopes of $\kappa(n)$ to monotonically increase with n from $\kappa(0) = 0.36$ nm^{-1} to $\kappa(6) = 0.41$ nm^{-1}. That slight increase is due to the increasing number of counterions in the finite system which also contribute to screening. In contrast to the simple exponential decay at large separations, for smaller distances the potential term $|re\beta\phi(r)|$ climbs up quickly with decreasing distance r to a maximum before it decays to almost vanishing potential close to the dPGS core. This highly nonlinear behavior is expected from the high electrostatic and steric correlations between sulfate beads and counterions in this dense Stern layer.

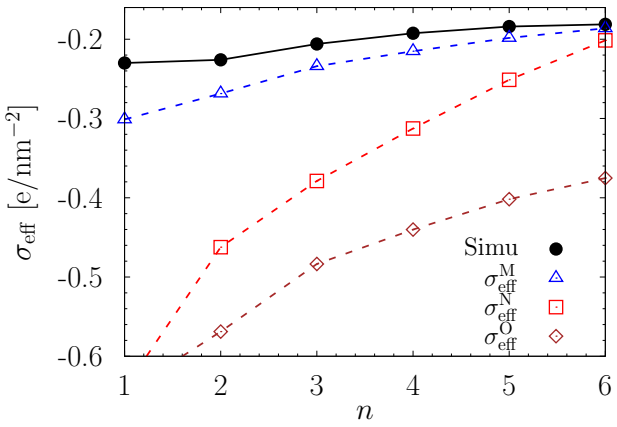

Figure 5.7: dPGS effective surface charge density $\sigma_{\rm eff} = Z_{\rm eff}/(4\pi r_{\rm eff}^2)$ versus dPGS generation number n. The solid circles are simulation results ranging from G_1 to G_6. The empty upward triangles, squares, diamonds are effective charge based on various theories as expressed by $\sigma_{\rm M}, \sigma_{\rm N}, \sigma_{\rm O}$ in eqs. (5.6), Eq. (5.7), and Eq. (5.5), respectively.

As indicated by Fig. 5.6(c), the potential can now be naturally divided into two parts: a DH-regime $r > r_{\rm eff}$, where the DH potential describes correctly the potential, and a non-DH regime $r_d < r < r_{\rm eff}$, where a non-monotonic and highly non-exponential behavior is revealed. In that sense, $r_{\rm eff}$ now acts as a measure of the dPGS effective radius at which we can attain an effective dPGS charge $Z_{\rm eff}$ [20]. We depict the position of the DH radius $r_{\rm eff}$ by

vertical dashed lines in Fig 5.6. We list r_{eff} and Z_{eff} in the Table 5.4 for generations 0 to 6. We find an increase of both r_{eff} and Z_{eff} with dPGS generation index and substantial charge renormalization effects. For instance, the bare charge for G_6–dPGS is $-384\ e$ (still presents at a radius r_d, cf. Fig. 5(b)) is effectively renormalized to $Z_{\text{eff}} = -32.9\ e$ at large distances $r > r_{\text{eff}}$. An exception is G_0 in which case we find $r_d \approx r_{\text{eff}}$ and hardly any renormalization by condensed counterions takes places. In agreement, the accumulated counterions profile N_+ for G_0 in Fig 5.6(a) reveals DH behavior almost in the full range of r and no inflection radius could be identified.

Note that both r_{inf} and r_{eff} can in principle be taken as definition for the effective size and charge of the charge-renormalized sphere. Although the difference between them appears not so large in Fig. 5.6, still a significant charge renormalization happens in between as the gradient $dN_+(r)/dr$ at r_{inf} is relatively large, *i.e.*, there is a marked density decrease of the counterions from distance r_{inf} to r_{eff}. In the following, we base our analysis only on r_{eff} as we believe that the inflection point criterion holds only for more idealized systems (smooth surfaces, no salt). The procedure to obtain r_{eff} rests on the assumption that we can treat the dPGS as simple DH spheres, so it exactly serves our purpose. Interestingly, a comparison of the corresponding effective diameter, $2r_{\text{eff}}$ to the size measured in the Zetasizer experiments in Fig 5.5(a) shows satisfying agreement. This demonstrates that the thickness of the correlated Stern layer in our simulation is of reasonable size and resembles the size of the bound solvation layer revealed by the experiments.

Effective surface charge density and potential

Considering the intrinsic radius r_d and the DH radius r_{eff}, the estimates of Z_{bar} and Z_{eff} lead to the dPGS bare surface charge density σ_d and effective surface charge density $\sigma_{\text{eff}} = Z_{\text{eff}}/(4\pi r_{\text{eff}}^2)$, respectively. Numbers are also summarized in Table 5.4. We find a monotonic decrease on σ_d with generation n, in response to the growing number of the surface beads. (The small portion of backfolding terminal beads increasing with generation decreases the surface charge valency slightly but not significant). Due to the large counterion-binding and charge renormalization effect, the effective charge density σ_{eff} is about one order of magnitude smaller than the bare one. Interestingly, it virtually remains constant, even slightly decreases

from $-0.23\ e\ \mathrm{nm}^{-2}$ for G_1 to a saturated value $-0.18\ e\ \mathrm{nm}^{-2}$ for G_5 and G_6. Experiments of carboxyl-terminated dendrimers at pH much larger than the pKa (i.e., almost full ionization) also found higher effective charge densities of a lower generation G_2 than for G_5 [12].

The results for the effective surface charge can be compared to available theories of charge renormalization of highly charged spheres, typically valid in low or high salt limits. Early approaches are based on approximate solutions of the nonlinear Poisson-Boltzmann equation for isolated spheres at infinite dilution, e.g., improvements of the now classical Ohshima potential [94] lead to [95]

$$\sigma_{\mathrm{eff}}^{\mathrm{O}} = \frac{-2e[1+\kappa(n)r_{\mathrm{eff}}]^2}{\pi l_{\mathrm{B}} r_{\mathrm{eff}}[1+2\kappa(n)r_{\mathrm{eff}}]} \tag{5.5}$$

and should be valid for large $\kappa r_{\mathrm{eff}} \gtrsim 1$, i.e., large spheres and/or high screening by salt. In the framework of standard counterion-condensation theory, Manning later derived a different but related expression for the saturation surface charge density of an isolated sphere in the same regime ($\kappa r_{\mathrm{eff}} \to 0$) as [96]

$$\sigma_{\mathrm{eff}}^{\mathrm{M}} = \frac{e[1+\kappa(n)r_{\mathrm{eff}}]\ln[\kappa(n)l_{\mathrm{B}}]}{2\pi l_{\mathrm{B}} r_{\mathrm{eff}}}. \tag{5.6}$$

In the other limit ($\kappa r_{\mathrm{eff}} \to 0$), Netz *et al.* [97] instead provide an estimate on the effective charge density explicitly dependent on the bare charge valency, Z_{bar}, by means of variational techniques, via

$$\sigma_{\mathrm{eff}}^{\mathrm{N}} = \frac{-e}{4\pi r_d l_{\mathrm{B}}} \ln\left(\frac{l_{\mathrm{B}}|Z_{\mathrm{bar}}|}{r_d^3\kappa^2}\right). \tag{5.7}$$

For our dPGS systems, intermediate values $0.25 < \kappa r_{\mathrm{eff}} < 1.6$ are established, for which an accurate analytical description apparently is difficult to achieve. We plot σ_{eff} in terms of generation number n, together with $\sigma_{\mathrm{eff}}^{\mathrm{M}}$, $\sigma_{\mathrm{eff}}^{\mathrm{N}}$ and $\sigma_{\mathrm{eff}}^{\mathrm{O}}$ in Fig. 5.7. We find that simulation and theory both yield the same trend, i.e., the absolute effective surface charge density decreases with generation n. Given the enormous charge renormalization effects of about one order of magnitude, the agreement to all theories is actually satisfactory, especially for the Manning theory. The relative error with respect to the magnitude of the bare surface charge is thus less than 10%. Based on this empirical comparison, the Manning approach can thus serve as a simple and analytical extrapolation to other systems and experiments.

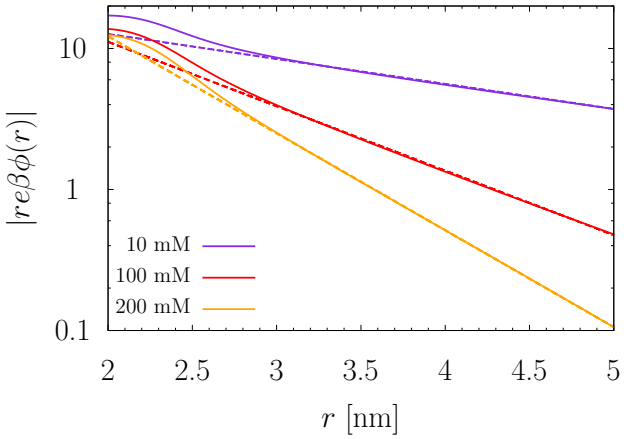

Figure 5.8: Log-linear plot of the distance-resolved G_5-dPGS radial electrostatic potential times distance, $|re\beta\phi|$, as in Fig. 5.6(c), but now for different salt concentrations $c = 10$, 100, and 200 mM. The dashed lines depict the corresponding DH potential ϕ_{DH} after fitting to the linear decay regime.

Correspondingly, we define the dPGS surface potential $\phi(r_{\mathrm{eff}})$, also summarized in Table 5.4. Similarly as the effective surface charge the surface potential is staying relatively constant with generation number. An inspection and comparison to ζ-potentials derived from our electrophoretic mobility experiments is made in Fig 5.5(b). Recall that the shear plane, where the ζ-potential is located, should lie beyond the Stern layer which refers to a position very close to r_{eff} where our effective surface potential $\phi(r_{\mathrm{eff}})$ is in the simulation [183, 184]. Indeed, as we see in Fig 5.5(b), $\phi(r_{\mathrm{eff}})$ reproduces the experimental ζ-potential very well at all generations. The sources of the remaining deviations can be of various origin, e.g., missing explicit water contributions to the electrostatic potential in the CG simulations or simply the lack of the exact knowledge of the shear plane. If, for instance, we assume an up- or down-shift of the location of the shear plane only about one solvation layer, say to be $\simeq r_{\mathrm{eff}} \pm 0.3$ nm, the experimental range is well matched, cf. Fig 5.5(b). Note also that in the experiments not directly the potential is measured but the electrophoretic mobility and their conversion is based on idealized models [185, 12].

5.5 Summary and concluding remarks

In summary, we have investigated the electrostatic (surface) properties of highly charged dendrimers for various generations at hand of the biomedically important dPGS polyelectrolyte. We have defined an effective charge, effective surface charge and potential of dPGS

for various generations and salt concentrations by a direct mapping procedure of the calculated electrostatic potentials onto the long-range Debye-Hückel-like electrostatic decay which defines the effective charge in its most practical level. The dPGS effective radius r_{eff} is accordingly addressed as a distance separating double-layer and condensation regimes and therefore gives the dPGS effective charge without ambiguity. Evidently, with that procedure the effective charge and the surface potential and their trends with generation can be consistently described by counterion-condensation theory and show very good agreement with new experimental ζ-potential measurements as well.

6 Counterion-release entropy governs the inhibition of serum proteins by hyperbranched polyelectrolyte drugs

In this chapter, we concentrate at the interaction between the dPGS molecules of various generations and some serum proteins. Any quantitative knowledge in that respect will become an important reference for the rational optimization of modern dendritic drugs and nanocarriers, especially in view of the dPGS as a focus in drug design because of their high biomedical potential. Lysozyme and HSA as well-defined serum proteins, the respective binding affinity with dPGS is investigated using ITC interpreted and complemented with molecular computer simulations. We demonstrate with high consistency among the methods and available data in literature that the driving force of the strong complexation originates mainly from the release of only a few condensed counterions from the dPGS upon binding. Our findings explain the high selectivity among P, L and E-selectins for dPGS, and can be extended to investigate the temperature effect found from dPGS binding, which follows with a notable enthalpy-entropy compensation. Note that the descriptions and figures in this chapter are taken almost literally from our previous publication [186].

6.1 Material and methods

CG protein and dPGS models

The CG force field for perfectly dendritic dPGS in explicit salts was derived from coarse-graining from all-atom explicit-water simulations as summarized in our previous work (See also Chapter 4) [158]. Briefly, the CG beads represent the inner core C_3H_5, the repeating unit C_3H_5O, and terminal sulfate SO_4 individually. Only the terminal segments are charged with -1 e, leading to the dPGS bare valency $|Z_n| = 6(2^{n+1}-2^n)$ of generation n. The model is fully flexible and has bond and angular intra-bond potentials. The water is modeled as a dielectric continuum, while salt- and counter-ions are explicitly resolved. The CG force field for the

proteins is derived from a structure-based model where every amino acid is represented by a single bead connected by a Go-model Hamiltonian [187] according to the structures from the the Protein Data Bank: 2LZT for lysozyme [188], 3CFW for L-selectin [189], and 1ESL for E-selectin [190]. The protein CG beads that correspond to basic and acidic amino acids were assigned a charge of +1 e and -1 e, respectively, approximating their dissociation state at pH = 7.4. Thus, the net charges of the simulated proteins were +8 e, 0 e, and -4 e for lysozyme, L-selectin, and E-selectin, respectively. Apart from the Coulomb interaction between all charged beads, the Lennard-Jones interaction acts between all CG beads. To approximate the van der Waals interaction energy between pairwise protein CG beads i and dPGS beads j with interaction diameter σ_{ij} we take the Lifshitz-Hamaker approach [191] and use the same $\epsilon_{ij} = 0.06\ k_{\mathrm{B}}T$ for all protein-dPGS beads pairs, equivalent with a Hamaker constant of 9 $k_{\mathrm{B}}T$ [68].

Details for CG and atomistic simulation

The implicit-water, explicit-salt CG simulations used the second-order SD (see Sec. 3.2) integrator in the GROMACS 4.5.4 software package [159]. The friction in the Langevin equation was set with a time constant of $\tau_t = 1$ ps. The electrostatic interactions were calculated via PME [105] summation where the long-range potential was evaluated in the reciprocal space using the FFT with a grid spacing of 0.16 nm and the cubic interpolation of the fourth order. A cut-off radius of 4 nm was defined for both PME summation and short-range van der Waals interactions. The choice of the cutoff is verified by reference simulations with an increased cutoff value $r_{\mathrm{cut}} = 6$ nm. Unless specifically stated otherwise, the temperature was set to 310 K and the salt concentration was set to 10 mM as the default, accompanied with a static dielectric constant of ϵ_r= 74.1 for the solvent modeled as a continuous medium. The production run of a NVT simulation lasted around 60 ns. The procedure to extract the PMF profile please refer to Sec. 3.2.

We employed the atomistic simulation in the respect of dPGS and L-selectin binding. The final complex structure of G3-dPGS and L-selectin was simulated via a standard, fully atomistic MD simulations built on the Optimized Potentials for Liquid Simulations 'All-Atom' (OPLS-AA) force field as included in GROMACS [159] and the SPC/E water model. We

assigned the partial atomic charges for the G3-dPGS inner core according to the OPLS-AA force field. The missing charges on sulfate in the OPLS are taken according to our previous atomistic simulations on G0 and G1 [158] that agree with with recent work [164] which has been applied, for instance, the simulations of sodium dodecyl sulfate micelles [165]. The initial configurations of G3-dPGS are constructed in a vacuum with the program ChemDraw [166]. The equilibrated structure of G3-dPGS is obtained after a 30 ns equilibration in the isobaric NPT ensemble (See Sec. 3.2) at conditions of $P = 1$ bar and $T = 293$ K. A cutoff distance 1 nm for both the PME summation and van der Waals interactions was used in a cubic box of side lengths 10.7 nm. For the atomistic simulation, the condensed counterions of the G3-dPGS are deemed as those within the distance $r_{\text{eff}} = 2.4$ nm with respect to the dPGS COM which has been previously justified [158]. The difference of the condensed counterions between the unbound and bound state leads to the released counterions number, where the bound state was obtained by placing the dPGS initially close to the binding patch observed in the CG simulations and let the system bind and equilibrate within 30 ns. The final statistics were generated from a canonical NVT simulation with a working trajectory of 30 ns

dPGS molecules in experiment and Isothermal Titration Calorimetry

dPG was synthesized by anionic ring opening polymerization of glycidol as reported before [192, 30]. Briefly, GPC was employed to measure the number averaged molecular weight of the core $M_{\text{n,dPG}}$ and the PDI. The synthesis led to samples of generations G2, G4, G4.5, and G5.5 with PDIs of 1.7, 1.7, 1.5, and 1.2, respectively. Afterwards, dPGS was prepared by the sulfation of dPG with SO_3-pyridine complex in DMF. DS was determined by elemental analysis. Standard ITC measurements were performed with a VP-ITC instrument (MicroCal, GE Healthcare, Freiburg, Germany) with a cell volume of 1.43 ml and a syringe volume of 280 μl. Lysozyme was titrated into dPGS in MOPS buffer at 37 °C. The MOPS buffer at pH 7.4 with different ionic strengths was prepared by adding sodium chloride into 10 mM MOPS accordingly. For all generations at 10 mM ionic strength and $T = 310$ K the measurements were independently performed three times with the lysozyme concentration

0.2 g/L (first 7 μL injection followed by 30x9 μL injections), 0.5 g/L (first 6 μL injection followed by 34x8 μL injections), and 1 g/L (first 3 μL injection followed by 55x5 μL injections) to balance the concentration error. At ionic strengths from 25 mM to 150 mM for G2, the lysozyme concentration increased from 1 g/L to 15 g/L, accordingly.

6.2 Definitions and calculation methods

Mean coordination number i^* in ITC and the corresponding coverage θ^*

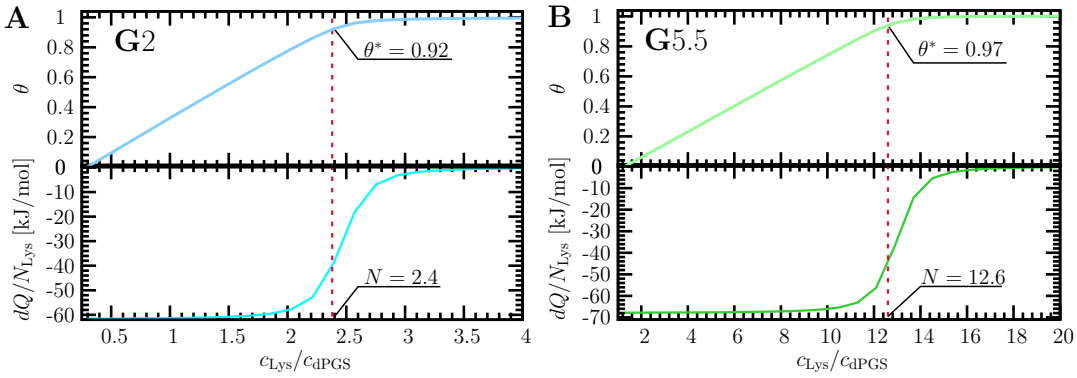

Figure 6.1: In the upper panel, we show the ITC binding isotherm and the corresponding protein coverage θ as a function of molar ratio χ for the generations G2 and G5.5. In the lower panel, the corresponding ITC differential heat is displayed. The dashed line indicates the binding stoichiometry N at the inflection point and the related coverage $\theta^*(N)$.

Given the sigmoidal differential heat curve normalized by the number of injected protein dQ/N_{Lys} versus the molar ratio $\chi = c_{\mathrm{Lys}}/c_{\mathrm{dPGS}}$, the inflection point directly delivers the binding stoichiometry N, see, for example the discussion in [193]. The protein coverage $\theta = i/N$ versus χ (i.e. the binding isotherm) can be calculated by the integrated heat as

$$\theta(\chi) = \int_0^{\chi} f(\chi')\mathrm{d}\chi' \; / \; \int_0^{\infty} f(\chi')\mathrm{d}\chi' \tag{6.1}$$

With that, one can define the protein coverage at which the binding affinity is evaluated by $\theta^* = \theta(\chi = N)$ as well as the the mean coordination number $i^* = N\theta^*$ at the respective binding equilibrium. In Fig. 6.1, we exemplify the calculation of θ^* and i^* concerning G2 and G5.5-dPGS, respectively, at hand of one of the three ITC measurements. The coverage

θ^* is found as $\theta^* = 0.92$ for G2 and $\theta^* = 0.97$ for G5.5, which correspond to the mean coordination numbers $i^* = 2.2$ for G2 and $i^* = 12.2$ for G5.5, respectively. In this thesis we report mean numbers averaged over all three ITC measurements.

The simulation-referenced Langmuir free energy

In a typical canonical simulation setup, the bound ligand concentration c_{bound} is defined by

$$c_{\text{bound}} = \frac{i}{V_b} = c_{\text{free}} \exp(-\beta \Delta G_{\text{b}}), \tag{6.2}$$

where c_{free} is the concentration of free (unbound) ligands and V_b refers to the effective binding volume which the ligand's degrees of freedom are allowed to sample. ΔG_{b} defines the transfer free energy from bulk to the bound state, which we evaluate from the PMF at the global binding minimum. We now assume that the binding complex can be considered as i lysozyme ligands bound in a shell at the spherical dPGS surface, which leads to the binding volume $V_b = 4\pi (r_b^{\text{sat}})^2 \delta_b$. We take the binding distance r_b^{sat} at coordination i directly from the simulation (see Table 6.1) as well as fix $\delta_b = 1$ nm, the thickness of the spherical binding shell, as a constant. The latter is motivated also directly from the PMFs (Fig. 6.3) whose attractive well widths span roughly a distance 1 nm at the bound state.

In comparison, in the Langmuir model the binding equilibrium for the protein coverage θ is defined as

$$\theta = \frac{i}{N} = c_{\text{free}} K_b (1 - \theta). \tag{6.3}$$

with $K_b = v_0 \exp(-\beta \epsilon_{\text{b}})$ the binding constant related to the Langmuir binding energy ϵ_{b}. To obtain a *standard* binding energy, the volume prefactor v_0 is usually taken to be 1 liter/mol. Comparing Eq. (6.2) and (6.3) defines the 'simulation-referenced' Langmuir *free energy*

$$\Delta G_{\text{b}}^{\text{ITC}} = \epsilon_{\text{b}} - k_{\text{B}} T \ln(1 - \theta) - k_{\text{B}} T \ln(V_0 N / V_{\text{b}}). \tag{6.4}$$

which allows a direct comparison between the ITC evaluation and the simulation PMFs. Note again that the standard Langmuir binding energy ϵ_{b} is in practice fitted around the inflection point $\chi = N$ of the ITC isotherm, see the discussion above, which results into coordination dependent binding affinity in non-ideal adsorption systems. That is the reason

Table 6.1: Summary of dPGS characteristics. $r_{\mathrm{b}}^{\mathrm{sat}}$ is the saturated dPGS-lysozyme binding distance as $i = N^{\mathrm{sim}}$, V_{b} the simulation binding volume, c_{ci} the local surface concentration of bound counterions, and $\Delta S_{\mathrm{CR}}T$ the entropic benefit per released counterion with salt concentration $c = 10$ mM.

dPGS	G2	G3	G4	G5
$r_{\mathrm{b}}^{\mathrm{sat}}$ [nm]	2.5	2.9	3.4	3.8
V_{b} [nm^3]	78.5	105.7	145	181.5
c_{ci} [M]	0.96	1.18	1.76	2.43
$\Delta S_{\mathrm{CR}}T$ [$k_{\mathrm{B}}T$]	4.6	4.8	5.2	5.5

why a calculation of $\Delta G_{\mathrm{b}}^{\mathrm{ITC}}$ (See Eq. (6.7)) can only be evaluated at $\theta^* = i^*/N$.

Electrostatic interaction energy calculated from the CG simulation

The (linear) screened part of the electrostatic interaction energy is considered in terms of the electrostatic interaction on the DH level between pairwise charged segments of the system. The gross DH electrostatic interaction energy $G_{\mathrm{ele}}^{\mathrm{sim}}$ presented in the results part is approximated as

$$G_{\mathrm{ele}}^{\mathrm{sim}}(\mathcal{C}) = \left\langle \sum_{m=1}^{N_{\mathcal{C}}} \sum_{j=m+1}^{N_{\mathcal{C}}} l_{\mathrm{B}} Q_m Q_j C_{\mathrm{QQ}} \frac{\exp(-\kappa r_{\mathrm{QQ}})}{r_{\mathrm{QQ}}} \right\rangle, \tag{6.5}$$

where the set $\mathcal{C}$ comprises all charged beads in the system apart from the solution ions. Eq. (6.5) includes all pairwise interaction between CG beads of charges Q_m and Q_j with separation r_{QQ}, ranging from $N_{\mathcal{C}}$ charged beads in the given set. $C_{\mathrm{QQ}} = \exp(2\kappa r_{\mathrm{Q}})/(1+\kappa r_{\mathrm{Q}})^2$ scales the Deybe-Hückel potential with $r_{\mathrm{Q}} = 0.4$ nm, the radius of the CG beads. The charge of the lysozyme beads follow from their used values for simulation. That is, either +1 or -1. Importantly, for the dPGS terminal beads, we assigned the respective bead charge uniformly being its *effective* charge, i.e., $Q = (Z_n + N_{\mathrm{cond}})/N_{\mathrm{ter}}$, where Z_{n} is the dPGS bare charge, N_{ter} the dPGS terminal beads number, and N_{cond} the number of condensed counterions. Thus, the charge renormalization effect is taken into account. N_{cond} is taken from the simulation as a function of the dPGS-dendrimer separation distance r. Moreover, the successively approaching lysozyme ligands gradually increase the number of the released counterions, which means N_{cond} is also as a function of the coordination i. Finally, the electrostatic interaction energy change $\Delta G_{\mathrm{ele,attr}}^{\mathrm{sim}}$ upon binding is given by

$$\Delta G_{\mathrm{ele}}^{\mathrm{sim}} = \langle G_{\mathrm{ele}}^{\mathrm{sim}}(\mathcal{C}) \rangle_{\mathrm{bound}} - \langle G_{\mathrm{ele}}^{\mathrm{sim}}(\mathcal{C}) \rangle_{\mathrm{unbound}}. \tag{6.6}$$

Table 6.2: Summary of dPGS characteristics as well as fitting parameters of the ITC of dPGS-lysozyme complexation evaluated via the standard Langmuir binding model. M_n is the respective dPGS molecular weight and Z_n the bare valency (i.e., number of terminal sulfate groups) both determined experimentally. Z_eff is the effective charge due to charge renormalization and r_eff is the effective Debye-Hückel radius interpolated from previous simulation work on perfect dendrimers [158]. The ITC fits via the Langmuir model yield the standard binding energy $\epsilon_b = -k_\mathrm{B}T \ln K_b$, enthalpy change ΔH, and stoichiometry N. The ITC was conducted at 10 mM salt concentration and $T = 310$ K.

dPGS	G2	G4	G4.5	G5.5
M_n [kD]	5	18	24	47
Z_n	-28	-102	-135	-266
Z_eff	-11	-19	-22	-28
r_eff [nm]	1.9	2.8	3.2	3.6
ϵ_b $[k_\mathrm{B}T]$	-19.0± 0.4	-20.3 ± 0.2	-20.0± 0.3	-19.3 ± 0.1
ΔH $[k_\mathrm{B}T]$	-23.7± 0.7	-24.4± 0.6	-25.3± 0.5	-25.8±0.9
N	2.9± 0.5	8.1± 0.2	8.8± 0.7	13.9±1.4

The difference is made between the bound and unbound state with $\langle \cdots \rangle$ standing for the ensemble average. Recall that the electrostatic repulsion results from the mutual repulsion between the bound lysozyme ligands. Thus, the repulsive part $G^\mathrm{sim}_\mathrm{ele,rep}$ of the electrostatic interaction energy can be computed similarly with Eq. (6.5), but with the set $\mathcal{C}$ consisting only of the lyosozyme charged beads. The difference of $G^\mathrm{sim}_\mathrm{ele,rep}$ at the bound and the unbound state leads to $\Delta G^\mathrm{sim}_\mathrm{ele,rep}$, as Eq. (6.6) indicated. The attractive part thus follows as $\Delta G^\mathrm{sim}_\mathrm{ele,attr} = \Delta G^\mathrm{sim}_\mathrm{ele} - \Delta G^\mathrm{sim}_\mathrm{ele,rep}$, which originates from the interaction between the lysozyme and dPGS carrying an effective charge.

6.3 Results

ITC experiments of dPGS-lysozyme complexation

In the first step we evaluated lysozyme-dPGS complexation for the generations $n = 2, 4, 4.5$ and 5.5 by ITC experiments. The generation index n has non-integer values because of the usual polydisperse synthesis. The released heat normalized by the number of injected proteins is plotted in Fig. 6.2A versus the molar ratio $c_\mathrm{Lys}/c_\mathrm{dPGS}$. The data are satisfactorily fitted with (SSIS) model (See Sec. 3.3 for details), that is, a standard Langmuir adsorption isotherm [128], with fitting parameters summarized in Table 6.2. The resulting number of binding sites per dPGS, i.e., the stoichiometry N, increases from 2.9±0.5 for G2 to 13.9±1.4

for G5.5. Hence, binding is multivalent, with N significantly increasing with growing generation n due to the expanding dendrimer size. The standard binding energy, $\epsilon_\mathrm{b} = -k_\mathrm{B}T \ln K_b$ between -19 and -20 $k_\mathrm{B}T$, is large, however, stays surprisingly constant with n despite the one-order-of-magnitude variation of molecular weight and bare charge among the generations, cf. Table 6.2. Importantly, ITC-experiments on the salt concentration dependence of the lysozyme complexation with G2 are plotted in Fig. 6.2B to scrutinize for counterion release effects according to the Record-Lohman law $d \ln K_b / d \ln c_s = -N_\mathrm{CR}$. The inset in Fig. 6.2B demonstrates that indeed a clear linear relationship, $\ln K_b \propto \ln c_s$, is found, except for the lowest ionic strength where stronger screened electrostatic (Debye-Hückel) interactions come into play (discussed in detail below). Evaluation of the slope suggests that $N_\mathrm{CR}^\mathrm{ITC} = 3.1 \pm 0.1$ ions per protein are released, triggered by the complexation.

The latter analysis strongly suggests that the dominating driving force for complexation originates from counterion-release entropy, in particular for larger (physiological) salt concentrations. However, one has to be aware that the Langmuir assumption of non-interacting ligands is violated for our system where apart from excluded-volume effects there exists a mutual DH-like screened electrostatic repulsion among the charged proteins bound in a multivalent fashion, cf. the protein corona. As a consequence of this *electrostatic anti-cooperativity*, the binding constant K_b is not really a constant but depends on the coordination number i. This renders the interpretation of K_b difficult. In that respect, we should recall that the value of K_b in Fig. 6.2A is actually determined by the slope at the inflection point of the plotted differential heat curves (valid for large affinities in the canonical ensemble [193]). From the integrated heat curves (see Fig. 6.1), we find thus that the obtained binding affinities correspond, for example for the generations $n = 2$, 4, and 5.5, to the binding at (mean) coordination $i^* = 2.7$, 7.8, and 13.1, respectively. The latter correspond to large coverages $\theta^* = i^*/N = 0.93, 0.95$, and 0.94, respectively. In our cooperative system we thus must expect that the binding affinity determined at these large coordinations can be quite different to that of the first binding protein.

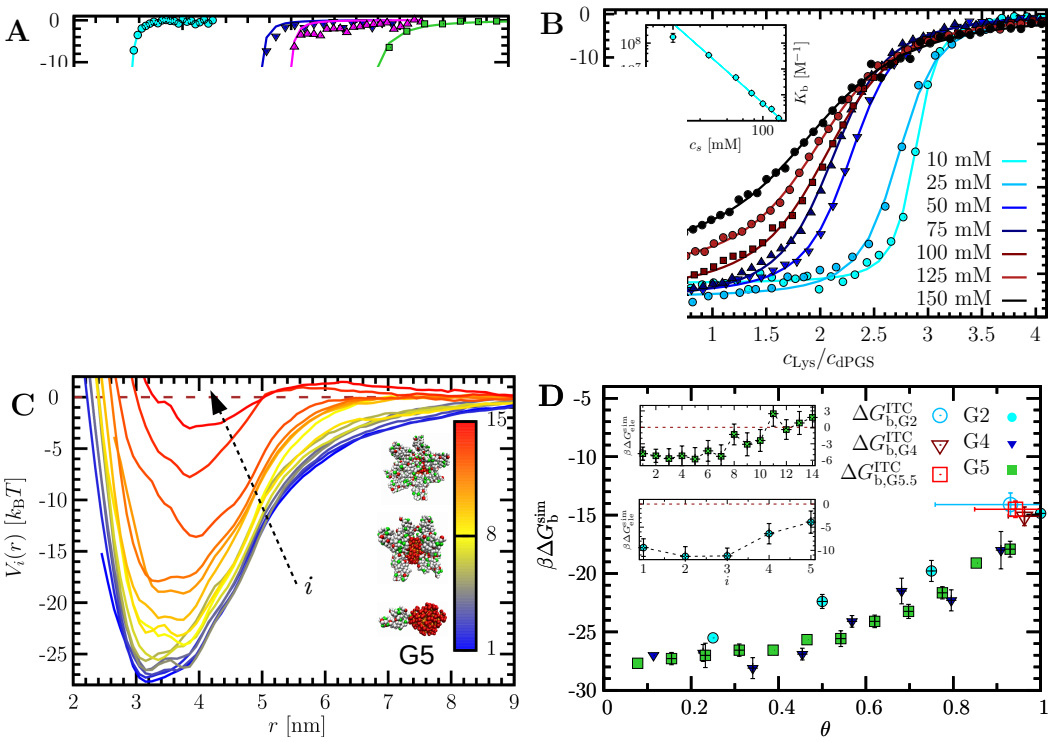

Figure 6.2: (A) ITC isotherms of the lysozyme-dPGS complexation ranging from generations 2 to 5.5 in MOPS buffer pH 7.4 at 310 K and 10 mM salt concentration. The solid lines correspond to the fits by the Langmuir model. (B) ITC isotherms of lysozyme-G2 complexation at different ionic strengths and fitted by the Langmuir model. The inset displays the salt dependence of the binding constant K_b on a log-log scale. According to Record-Lohman [100], $-d\ln K_b/d\ln c_s = N_{CR}^{ITC} = 3.1 \pm 0.1$ counterions are released upon binding. (C) CG simulation results of the PMF, $V_i(r)$, as a function of the center-of-mass distance r between G5 and lysozyme for the successive binding of $i = 1$ to 15 proteins in 10 mM salt concentration, color-coded according to the scale. Snapshots of the equilibrium complex for $i = 1, 8, 13$ are shown. (D) The simulation binding free energy $\Delta G_b^{sim}(i)$ (symbols) plotted versus coverage $\theta = i/N^{sim}$ for G2, G4, and G5, respectively, read off from the global minimum of the PMFs, as such in (C). The large open circle, triangle and square symbols indicate the simulation-referenced Langmuir binding free energy $\Delta G_b^{ITC}(i^*)$, Eq. (6.7), for G2, G4, and G5.5 at their respective coverage θ^*. The insets present the total DH electrostatic interaction energy $\Delta G_{ele}^{sim}(i)$ between ith ligand and the complex for G2 (bottom) and G5 (top).

Binding affinity and interactions from CG simulations

To further dissect and rationalize the experimental problem we employ CG, but ion-resolved, computer simulations of lysozyme association with the perfect dendrimers G2, G3, G4, and G5 [158]. We focus on the case of 10 mM salt concentration where electrostatic cooperativity effects are strongest. The virtue of the simulations is that we can calculate the total binding *free energy* $\Delta G_b^{sim}(i)$ of the ith lysozyme with the complex where $i-1$ proteins are already associated, i.e., we can stepwise investigate the assembly along i. The binding free energy can be conveniently read off from the computed PMF as a function of the pair separation

distance, $V_i(r)$, at hand of the difference between the unbound ($r = \infty$) and the bound state at the PMF minimum at $r = r_\mathrm{b}$. The PMFs for the example of G5 are plotted in Fig. 6.2C, along with snapshots of the growing protein corona. The results for the free energy of binding, $\Delta G_\mathrm{b}^\mathrm{sim}(i) = V_i(r_\mathrm{b})$, as well as those for G2 and G4, are presented in Fig. 6.2D versus the coverage $\theta = i/N^\mathrm{sim}$. We find a strong attraction of very similar magnitude for all generations that diminishes with rising i. For instance, $\Delta G_\mathrm{b}^\mathrm{sim}(i)$ for G5 reduces from $\simeq -28\ k_\mathrm{B}T$ for $i = 1$ to $\simeq -8\ k_\mathrm{B}T$ for the 14th protein and is almost vanishing for $i = 15$. Hence, the maximum coordination in the simulations, N^sim, for G5 is about 15, while for the smaller G4 and G2 we see maximally 10.8 and 5.2 ligands adsorbed, respectively. The stoichiometry from the simulations overestimate the ones evaluated from ITC by about 2 ligands, cf. Table 6.2, which is quite satisfactory given the strong ideality assumptions in the Langmuir model.

One reason for the decreasing attraction with i is the growing anti-cooperative DH repulsion between ligand i and the complex (involving $i - 1$ proteins). The net DH interaction energy between ligand i and the complex is plotted in the insets to Fig. 6.2D for the examples of G2 and G5: For low coordination i, an attractive DH interaction between the oppositely charged dPGS and proteins is observed, as expected. For increasing i, the DH interaction stays roughly constant before it becomes much less attractive near saturation ($i \simeq N^\mathrm{sim}$), due to additional protein-protein repulsions. The net DH interaction becomes even repulsive for G5, i.e., the complex shows a charge-reversal behavior. The second reason for the decreasing attraction (free energy) with rising coordination i arises from the ligands' steric packing near saturation, or, in Langmuir terms, from filling up all possible binding sites.

In order to compare the binding affinity obtained from ITC at coordination i^* consistently to the simulations, we define the simulation-referenced *Langmuir free energy* (for the derivation see Sec. 6.2)

$$\Delta G_\mathrm{b}^\mathrm{ITC}(i^*) = \epsilon_b - k_\mathrm{B}T \ln(1 - i^*/N) - k_\mathrm{B}T \ln(N^\mathrm{sim} v_0/V_b), \tag{6.7}$$

where the first term on the right hand side is the standard Langmuir binding energy (cf. Table 6.2), the second term is the Langmuir entropic packing term, and the third term converts the Langmuir standard reference state with binding volume $v_0 = 1/\mathrm{mol}$ to the

simulation binding volume V_b [127] (see Table 6.1). The results for $\Delta G_{\rm b}^{\rm ITC}(i^*)$ for generations $n = 2, 4$ and $n = 5.5$ are all very similar with 14-15 $k_{\rm B}T$ and shown as big symbols at θ^* in Fig. 6.2D. They nicely match the simulation free energies at coverages of $\theta = 0.9 \pm 0.05$, consistent with the θ^* values where the ITC binding affinity was determined. Note that a more quantitative dissection of only the ITC binding affinity K_b (or ϵ_b) is out of reach as it carries a complex mix of contributions from counterion-release (see below) and DH electrostatics as well as many-body excluded-volume effects. However, our analysis on the free energy level shows full consistency between ITC and computer simulations, in particular regarding the weak n-dependence of the observed complexation affinities.

Counterion-release as main driving force

We now discuss the details of the interactions driving the complexation of only the first protein, $i = 1$, (where no cooperative effects play a role) to dPGS of the various generations n. The PMFs are shown in Fig. 6.3A. The reasons for the weak n dependence of the binding free energy, ranging from $\simeq -26\ k_{\rm B}T$ for G2 to $\simeq -28\ k_{\rm B}T$ for G5, we find are twofold: First, despite the very high net charge of dPGS, the electrostatic screening (DH) part of the PMF, $V_{\rm ele}(r)$, plotted in the inset to Fig. 6.3A, is found to be relatively small. Corresponding contributions are $\simeq -9$ to -4 k_BT in the respective range of $n = 2$ to 5, apparently saturating already for $n > 3$. The main cause for this is that dPGS exhibits a strong counterion condensation and accompanying charge renormalization effect in the saturation regime, leading to a relatively weakly n-dependent *effective* surface charge [158], cf. Table 6.2. Thus, apart for G2, the DH contribution is of minor importance and relatively constant with n. Second, a key consequence of the condensation effect is the release of highly confined counterions upon protein binding. Fig. 6.3B presents the number of released counterions $N_r(r)$ in the CG simulations as a function of distance r, determined by counting the ions within the dPGS condensed ion region [158]. The number of released ions at the bound state is read off at the binding distance $r_{\rm b}$, i.e., $N_{\rm CR}^{\rm sim} := N_r(r_b)$. We find $N_{\rm CR}^{\rm sim} \simeq 3.3, 4.4, 4.5$, and 4.8 for generation G2, G3, G4 and G5, respectively. For G2, we reach a very good agreement with the number $N_{\rm CR}^{\rm ITC} = 3.1 \pm 0.1$ attained by the Record-Lohman analysis of the ITC data in Fig. 6.2B. The difference of $N_{\rm CR}^{\rm sim}$ among the last three generations is quite minor. This is understandable

as the protein surface serves as a generation-independent 'template' that sets the number of replaceable counterions by the number of positive charges in the binding region ('patch'), see the illustrative snapshot in the inset of Fig. 6.3A: Indeed several positively charged beads (colored in green) cluster in the binding patch. Accordingly, for $n \gtrsim 3$, where the dPGS surface area is much larger than the binding patch, the dPGS size has a very weak influence on the number of r

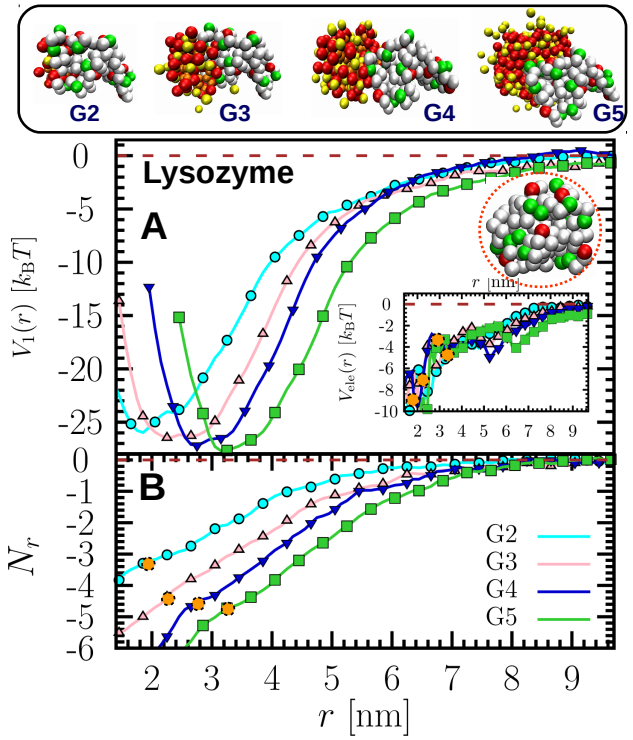

Figure 6.3: (A) The PMF, $V_1(r)$, and (B) the number of released counterions, $N_r(r)$, versus the center-of-mass separation distance r for the first lysozyme, $i = 1$, for G2 to G5 at 10 mM salt concentration from CG simulations. The lysozyme-dPGS complex (with snapshots on top) is stabilized at a distance r_b (PMF minimum) where the binding free energy is $\Delta G_b^{sim}(i = 1) := V_1(r_b)$ and the number of released counterions (indicated by orange circles in (B)) is $N_{CR}^{sim} := N_r(r_b)$. The insets in (A) depict the lysozyme binding patch (top inset, with positively charged beads in green), and the DH electrostatic interaction energy $V_{ele}(r)$ (bottom inset).

For a more quantitative assessment we estimate that the condensed counterions are confined in the dPGS shell with a local surface concentration $c_{ci} \simeq 3N_{ci}/[4\pi(r_{eff}^3 - r_d^3)]$, where $r_{eff} - r_d$ defines the width of the interactive surface shell region (or 'Stern' layer) between the diffusive ionic double layer and the sulfate surface groups [158]. We find $c_{ci} \simeq 2.43$ M for G5, more than one or two orders of magnitude larger than typical physiological or experimental bulk concentrations. According to Record-Lohman analysis, this can be translated

into the entropic benefit $\Delta S_{\rm CR}T \simeq 5.5\ k_{\rm B}T$ per counterion upon its release into bulk at salt concentration $c_s = 10$ mM. That amounts to the gross free energy gain $\simeq -27\ k_{\rm B}T$

ion

to

$_3T$.

ıat

.

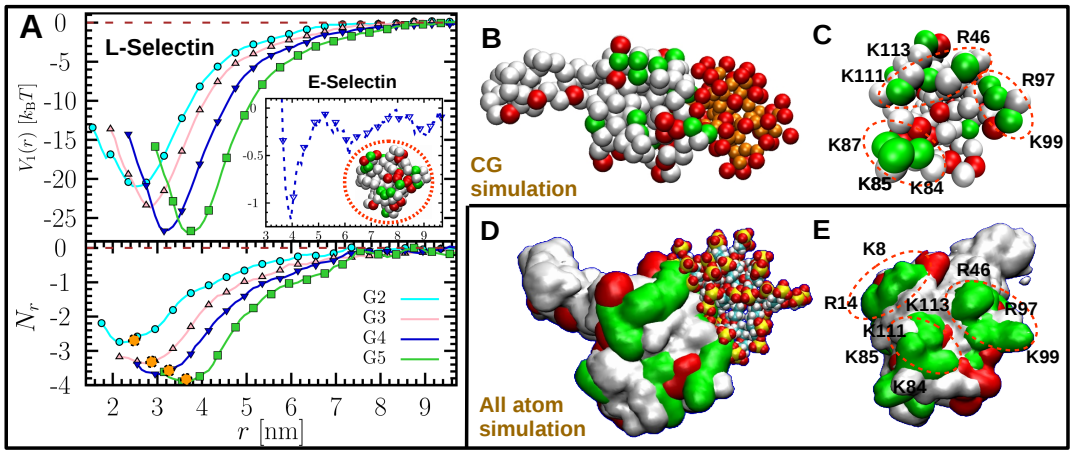

Figure 6.4: (A) The PMF $V_1(r)$ (upper panel) and the corresponding number of released counterions $N_r(r)$ (lower panel) for the first bound L-selectin at dPGS of generations 2 to 5 at 10 mM salt concentration from CG simulations. As a comparison, the inset shows the PMF between G4-dPGS and E-selectin with the same simulation conditions and a snapshot of the E-selectin binding patch. In the center, (B, D) present snapshots of the L-selectin/G3-dPGS binding complex: CG versus all-atom simulations. In the right row, (C, E), the corresponding snapshots of the L-selectin binding patch is shown. The responsible basic amino acids shown to be interactive with dPGS are labeled and highlighted.

We finally applied our CG simulations to the biomedically important (E and L) selectin proteins. Regarding the first ligand coordination, the PMF profiles, binding free energies, released counterions as well as illustrative snapshots are presented in Fig. 6.4. A weak dependence of the binding free energy on dPGS generation is revealed for L-selectin, where $\Delta G_{\rm b}^{\rm sim}(i=1) \simeq -21\ k_{\rm B}T$ for G2 and $\simeq -27\ k_{\rm B}T$ for G5 (See Fig. 6.4A). This behavior resembles that of lysozyme and is again accompanied by a relatively constant number of released counterions upon binding, being $N_{\rm b} \simeq 3 \sim 4$ for all generations. The corresponding binding patch of L-selectin is found to accommodate a number of positively charged groups,

with complexation snapshots shown in Fig. 6.4B and the binding interface presented in Fig. 6.4C. Furthermore, we conducted the CG simulation also for G3-dPGS and L-selectin at near physiological salt concentration $c_s = 150$ mM and temperature $T = 293$ K, for which the experimental binding affinity from fluorescence measurements is available [60]. The simulated result, $\Delta G_b^{sim}(i = 1) \simeq -15.0\ k_B T$ is found in good agreement with $\simeq -12.1\ k_B T$ measured in the experiment for a 1:1 binding stoichiometry.

To further support the structural picture, the final G3-dPGS/L-selectin complex was studied by standard (AA) molecular dynamics simulations. Compared to the CG simulation, we find that the number of released counterions as well as the structure of the complex is virtually the same, cf. Fig. 6.4D and E, regardless of the inclusion of the explicit solvent and atomistic structure. We find 3.3 liberated counterions in the AA simulation and 3.6 for the CG simulation. However, the CG model, where each amino acid is replaced by a simple bead, to some extent brings small deviations to the surface geometry as compared to the fully atomistic protein structure: we find that in the AA simulations two more amino acids R14 and K8 of L-selectin can interact with the dPGS (see Fig. 6.4E). Nevertheless, apparently this deviation in the binding interface does not much affect the mean number of released ions.

Finally, as opposed to L-selectin, we find from the CG simulations that E-selectin has a much weaker affinity to dPGS. The binding free energy (see the inset to Fig. 6.4 A) is only about $-1\ k_B T$, suggesting a very unstable binding complex. Such an intriguing selective binding behavior is in full agreement with the protein's anti-inflammatory potency [30]. Interestingly, the global features of the native structure of E-selectin are not so different from L-selectin. For instance, 157 amino acids and -4 e net charge for E-selectin have to be compared to 156 amino acids and zero net charge for L-selectin. However, our findings clearly show that the underlying difference of $\sim 26\ k_B T$ in the binding affinities must be assigned to local changes in protein interface structure, where a patch accommodating many positive charge clusters as in lysozyme or L-selectin is less developed [194], see also the inset to Fig. 6.4A.

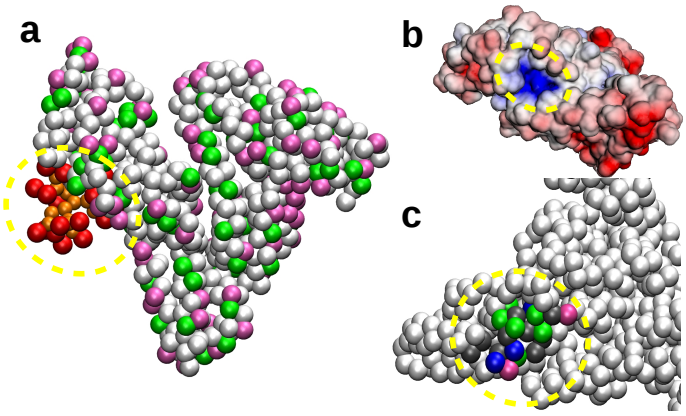

Figure 6.5: (a) Representative CG simulation snapshot of the dPGS-G2-HSA complex at ionic strength 25 mM. Neutral beads in the protein are colored white, positive beads are green, and negative beads are pink. For dPGS-G2, the terminal charged groups are colored red, whereas the monomer beads are orange. The patch on HSA that found in CG simulation responsible for locating dPGS-G2 is marked in yellow dashed circle. In particular, we magnify the HSA binding site in panel (c) which displays the positive amino acids in Sudlow site II that directly participate in the binding. The binding site is hydrophobic with ten hydrophobic beads (dark grey) and three hydrophilic beads (blue). In panel (b), we compute the surface charge potential of the binding site according to its charge distribution at physiological pH via an adaptive Poisson-Boltzmann Solver. Regions possessing positive and negative charges are colored blue and red, respectively.

Interaction between G2-dPGS and HSA

As an extension, we investigate the binding behavior between G2-dPGS and HSA. The convenience of this study is that the binding stoichiometry remains as 1, which means the binding is free of any degrees of cooperativity and the standard Langmuir adsorption isotherm is fully justified. In particular, we find that G2-dPGS binds to Sudlow site II on HSA. The details of the binding site are shown in Fig. 6.5. It is interesting to note that poly(acrylic acid) is also binding to the Sudlow II site [129]. The corresponding site on the protein exhibits a positive surface charge as indicated in Fig. 6.5(c). This site interacts with the dPGS-G2 bearing opposite negative charges of high density. According to the simulation, the amino acids at the binding site that directly contact with dPGS are: positive: Arg410, Lys413, Lys534, Lys536, Lys538, Lys541, and negative: Glu492, Glu542.

The coarse-grained simulation computes the potential of mean force (PMF) as a function of the HSA-dPGS center-of-mass distance r (see Fig. 6.6). The free enthalpy ΔG_{b} obtained by the simulation can be read off as the difference between the zero free energy reference state at far separation (horizontal brown dotted line) and the global minimum representing the bound state. We also calculate the accessible volume $V_b \simeq 1.44$ nm^3 from simulation quite

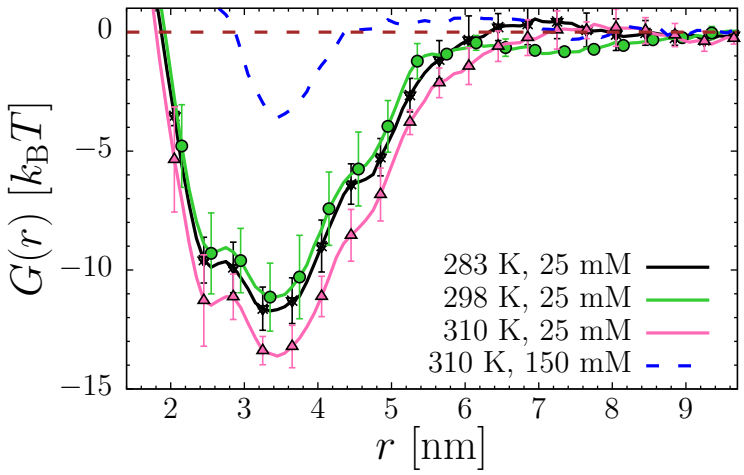

Figure 6.6: The free energy profile (or potential of mean force) $G(r)$ between G2-dPGS and HSA versus their center-of-mass distance r at different ionic strengths and temperatures. The error bars come from 3 independent runs.

quite consistent for all cases. With that, the corresponding standard binding free energy (See Sec. 3.2) $\Delta G_{\rm b}^{\rm sim}$ at $c_{\rm s}$=25 mM agrees very well with the experimental values $\Delta G_{\rm b}^{\rm ITC} \sim -13.7\ k_{\rm B}T$ and $\sim -12.4\ k_{\rm B}T$ at 283 K and 298 K, respectively. The simulation indicates that electrostatic interaction is the dominant driving force for the binding of HSA with dPGS at low ionic strength. Also, there is only a weak dependence of the simulated binding free energy $\Delta G_{\rm b}^{\rm sim}$ on temperature. This is in full agreement with the experimental data. This result indicates the underlying enthalpy-entropy cancellation. The agreement between experiment and simulation implies this cancellation of possible hydrophobic contributions to enthalpy and entropy is nearly total. At 310 K and a higher salt concentration $c_{\rm s}$=150 mM the electrostatic interaction coming from the DH terms gets diminished due to screening. In this case, we estimated $\Delta G_{\rm b}^{\rm sim} \simeq$ -4 $k_{\rm B}$T. However, due to weak binding nature in that case, the ITC experiment is incapable of measuring $\Delta G_{\rm b}^{\rm ITC}$ with reasonable error bar. As an alternative, a rough estimate $\Delta G_{\rm b}^{\rm ITC} \sim -3.5 \pm 1.0\ k_{\rm B}T$ is found by extrapolating the binding free energy profile at low concentration. Hence, simulation shows that HSA exhibits only a very weak binding to dPGS-G2 in full agreement with experiments. The present accuracy of the data, however, allows no further conclusion.

6.4 Concluding remarks

We demonstrated that the complexation of proteins with highly charged dendritic macromolecules is largely dominated by the fully entropic counterion-release mechanism. The complexation is weakly dependent on the generation mainly due to two effects: first, the relatively small effective surface charge of dPGS in the charge renormalization saturation limit leads to a weak generation dependence of the Debye-Hückel interactions. Secondly, for not extremely small dendrimers the magnitude of the dominating counterion contribution (directly proportional to the number of released ions) only depends on the protein-specific interfacial binding patch structure. With that the experimentally found high selectivity and weak generation dependence of dPGS in its anti-inflammatory potential towards relevant proteins can be fully understood. Our clear mechanistic picture behind the dPGS-protein complexation shall be important for the rational optimization of dendritic polyelectrolytes as potential drugs and nanocarriers.

7 Summary of the thesis and outlook

Summary of the thesis

In this thesis, we carried out a systematic study on the electrostatic complexation between strong anionic polyelectrolytes and proteins. We aim at a description of the electrostatic complexation in terms of well-established theories, the Deybe-Hückel theory and the concept of charge renormalization. With that, one can understand and optimize the binding behavior with clean and unprecedented molecular and quantitative insight. The electrostatic complexation is examined for various cases, including the complexation between pairwise polyelectrolytes with opposite charge, as well as for the interactions between the dPGS particle of biomedical importance and several serum proteins. For different complexations we have observed quite diverse binding properties along the binding pathway, ranging from the intriguing hand-shaking phase emerged from polyelectrolyte complexations to the successive protein packing on the dendrimer surface with strong binding cooperativity. Nevertheless, quite consistent for all systems, there is a certain number of the counterions previously condensed on the receptor surface that are released upon its binding to an oppositely charged interface 'patch' specific to the ligand, providing a massive entropy gain. This entropy gain governs the complexation serving as the driving force for all the systems under investigation. Our finding thus provides a quantitative understanding of the binding free energy between proteins and polyelectrolyte ligands, which paves the way for the rational optimization of modern dendritic drugs and nanocarriers.

Particularly, in **chapter 4** we begin the study with linear polyelectrolyte chains which have been well modeled for the past decades. We utilize the coarse-grained, implicit-solvent and explicit-salt computer simulations to resolve the LPE configuration states and the corresponding PMF profiles along the binding pathways. Our simulation accesses the intriguing LPE transient states once the counterion-condensation threshold is exceeded. For that case, the LPE association process exhibits a distinct sliding-rod-like behavior where the polymer chains approach each other by first stretching out at a critical distance close to their contour length, then 'shaking hand' and sliding along each other in a parallel fashion, before

eventually folding into a neutral complex. This is well described by a simple theory based on sliding charged 'Debye–Hückel' rods with renormalized charges in addition to an explicit entropy contribution owing to the release of condensed counterions, which leads to a full quantitative understanding of the PMF from simulations. This method is used to investigate the LPE-HSA complexation. The simulation helps to resolve the binding stoichiometry, complex and affinity, which is subsequently confirmed by ITC experiments.

Inspired by the insights attained from LPE simulations, we increase the complexity by studying the biomedically important dPGS macromolecules. Various degrees of similarity exist between LPE and dPGS. For instance, they are both heavily charged and belong to the PE family but with different connectivity number. Thus, the CG simulations with implicit-solvent and explicit-salt applied previously to PE can be transferred here to resolve the dPGS molecular and electrostatic properties. Since the dPGS is a newly developed chemical compound, in **chapter 5** we first focus at constructing an effective mesoscale Hamiltonian specific to the dPGS based on input from all-atom, explicit-water simulations of the dPGS of low generations. In order to parameterize the proposed CG force field for dPGS, we aim at a proper definition of the dPGS effective radii and charges as a function of generation, given a considerable number of condensed counterions. A systematic mapping of the calculated electrostatic potential onto the Debye-Hückel form is proposed, which serves as a basic defining equation for the effective charge, then we determine well-defined effective net charges and corresponding radii, surface charge densities, and surface potentials of the dPGS, which compare very well with our new electrophoretic experiments and existing analytical theories.

Owing to the mesoscale Hamiltonian specific to the dPGS established previously, in **chapter 6** we investigate the interaction between the dPGS and several serum proteins both resolved on the CG level. The CG simulations give direct access to the binding stoichiometry and free energy which are complemented with ITC experiments. High consistency is found between simulations and experiments, ascribed to the definition of the simulation-referenced *Langmuir free energy* which bridges the simulation results to the ITC experiment even in the presence of the binding cooperativity. Importantly, the driving force of the strong complexation originates mainly from the release of only a few condensed counterions from the dPGS upon binding, which is essentially the same as the LPE-LPE complexation reported in

chapter 4. That concept is confirmed by the Record-Rohmann analysis of the experimental data, and rationalizes a surprisingly weak dependence of the binding affinity on dPGS size, revealed both from simulations and experiments.

To conclude, this thesis provides a systematic investigation to electrostatic complexation in several systems. The models and methods used in this thesis can be easily adopted to describe more general constituents of living cells in nature comprising many charges on their surfaces, including DNA/RNA, architectural proteins, cellular lipid membranes, and natural ion channels [195]. In particular, we revisit the electrostatic properties of the charged dendrimers and the associated electrostatic complexation on the CG level with simulations of large temporal and spatial scale. This approach is justified after a comparison with experiments and theories. The dominant role of counterions in electrostatic complexation is unambiguously demonstrated throughout this study. This knowledge may inspire pharmaceutical developments, for instance, to develop more effective anticancer drugs that interact with DNA and proteins possessing the proper binding affinity [196]

Outlook

Even though the binding affinity in our CG simulations agrees very well with experiments, we still can not resolve all thermodynamic properties of the binding due to the absence of water. From the perspective of enthalpy and entropy, significant contribution comes from water molecules due to their high number. A recent ITC experiment reveals a strong temperature dependence of the dPGS-HSA binding enthalpy which, however, can not be captured by the current CG simulations. Thus, it is necessary to construct full atomistic simulations taking into account explicit solvent to resolve the dPGS hydration layer and the releasing water molecules, much the same way as we did for counterions. With an eligible atomistic force field, especially for the terminal groups, the atomistic simulations can possibly shed light on the very puzzling ion-specific effect revealed by the highly functionalized polyanions based on a dendritic polyglycerol (dPG) scaffold [13], which to date can not be understood by the Hofmeister series.

The current CG simulations are mostly performed at fixed low salt concentrations such

that the notable role of the electrostatics is present. Despite a few simulations are conducted at a higher concentration ($c = 150$ mM) to mimic the physiological environment, we only account the symmetric monovalent electrolytes in absence of any multivalent salts. Thus, it is interesting to explore the counterion condensation and the charge renormalization in a wide range of salt concentrations, as well as the effects after the addition of the multivalent ions. In particular, for a system with multivalent ions, less preference is expected for the system to release the condensed multivalent counterions in view of their strong association with the molecule. This difference thus requires corrections to the current counterion releasing mechanism found for monovalent ions. Moreover, the CG simulations used here can combine with an external electric field to reproduce the electrophoretic behavior of the charged molecules. Important conclusions on locating the very controversial shear plane might be expected.

In chapter 6, we derived a way of connecting the ITC experiment interpreted by the Langmuir isotherm to simulations. As an alternative, the Langmuir isotherm can be replaced by an advanced binding model that explicitly includes the binding cooperativity. Those binding models are supposed to provide a full description of the protein corona construction on a nanoparticle surface. In particular, the interplay of the ligand-receptor interaction, the ligand-ligand interaction, the ligand packing free energy, and the counterion release entropy will be captured. More importantly, the adopted binding models can be utilized to directly fit the ITC data. As a result, the full binding affinity profile with the resolution of every individual binding site will be obtained.

The current study on the protein-polyelectrolyte interaction provides numerous speculations/hints for pharmaceutical science and polymer engineering. Firstly, we deliver a strong indication that the binding affinity between the dendritic polyelectrolyte and serum proteins is insensitive to the dendrimer size. Thus, the preoccupation for the dendritic drug/carrier design should give way to the ligand loading capacity and the circulation time of the dendrimer in vivo [197]. While the binding affinity modification correlates with the control of the released counterions, given a dominant role of counterions for the ultimate binding. In particular, for the optimization of the antifouling properties of polymeric surfaces [10], we suggest a number reduction of the released counterions. A feasible strategy in that respect is to opt polymers that possess functional groups binding less favorably to solution ions.

In view of the intriguing weak dependence of the surface potential versus nanoparticle size uncovered in this thesis, our study indicate the way by adjusting the solution environment in terms of the salt concentration or the inclusion of multivalent ions, in order to generate charged polymeric ligands with desirable surface potential.

List of tables

List of figures

List of abbreviations

AA all-atom

CG coarse-grained

COM center-of-mass

COM centers-of-mass

DH Deybe-Hückel

DLS dynamic light scattering

DLVO Derjaguin-Verwey-Landau-Overbeek

DMF dimethylformamide

dPG Dendritic polyglycerol

dPG dendritic polyglycerol

dPGS dendritic polyglycerol sulfate

DS degree of sulfation

FFT Fast Fourier Transform

GPC Gel permeation chromatography

HSA Human Serum Albumin

HSA human serum albumin

HSA human serum albumin

IBI iterative Boltzmann inversion

ITC isothermal titration calorimetry

LD Langevin dynamics

LPB linearized Poisson Boltzmann

LPECs linear polyelectrolyte complexes

MD molecular dynamics

NaPSS poly(sodium styrene sulfonate)

PAMAMs polyamidoamines

PB Poisson-Boltzmann

PBC periodic boundary condition

PDI Polydispersity index

PEs polyelectrolytes

PME Particle Mesh Ewald

PMF potential of mean force

PTX Paclitaxel

SD stochastic dynamics

SLD steered Langevin Dynamics

SPC/E extended simple point charge

SSIS single set of independent binding sites

vdW Van der Waals

Bibliography

[1] X. Du, Y. Li, Y.-L. Xia, S.-M. Ai, J. Liang, P. Sang, X.-L. Ji, and S.-Q. Liu. "Insights into Protein–Ligand interactions: mechanisms, models, and methods". *Int. J. Mol. Sci.* 17.2 (2016), p. 144.

[2] S. W. Sarsam, D. R. Nutt, K. Strohfeldt, and K. A. Watson. "Titanocene anticancer complexes and their binding mode of action to human serum albumin: A computational study". *Metallomics* 3.2 (2011), pp. 152–161.

[3] T. J. Dolinsky, P. Czodrowski, H. Li, J. E. Nielsen, J. H. Jensen, G. Klebe, and N. A. Baker. "PDB2PQR: expanding and upgrading automated preparation of biomolecular structures for molecular simulations". *Nucleic acids research* 35.suppl_2 (2007), W522–W525.

[4] J. M. Park, B. B. Muhoberac, P. L. Dubin, and J. Xia. "Effects of protein charge heterogeneity in protein-polyelectrolyte complexation". *Macromolecules* 25.1 (1992), pp. 290–295.

[5] C. Yigit, M. Kanduc, M. Ballauff, and J. Dzubiella. "Interaction of charged patchy protein models with like-charged polyelectrolyte brushes". *Langmuir* 33 (2016), pp. 417–427.

[6] C. Yigit, J. Heyda, M. Ballauff, and J. Dzubiella. "Like-charged protein-polyelectrolyte complexation driven by charge patches". *J. Chem. Phys.* 143 (2015), p. 064905.

[7] M. Rooman and R. Wintjens. "Protein–DNA Interactions". *eLS* ().

[8] S. Han et al. "Protein- Protein Recognition Control by Modulating Electrostatic Interactions". *Journal of proteome research* 9.6 (2010), pp. 3118–3125.

[9] H. Gohlke and G. Klebe. "Approaches to the description and prediction of the binding affinity of small-molecule ligands to macromolecular receptors". *Angewandte Chemie International Edition* 41.15 (2002), pp. 2644–2676.

[10] Q. Wei et al. "Protein interactions with polymer coatings and biomaterials". *Angewandte Chemie International Edition* 53.31 (2014), pp. 8004–8031.

[11] M. K. Gilson and H.-X. Zhou. "Calculation of protein-ligand binding affinities". *Annu. Rev. Biophys. Biomol. Struct.* 36 (2007), pp. 21–42.

[12] Q. Huang, P. Dubin, C. Moorefield, and G. Newkome. "Counterion binding on charged spheres: Effect of pH and ionic strength on the mobility of carboxyl-terminated dendrimers". *The Journal of Physical Chemistry B* 104.5 (2000), pp. 898–904.

[13] M. Weinhart, D. Gröger, S. Enders, J. Dernedde, and R. Haag. "Synthesis of Dendritic Polyglycerol Anions and Their Efficiency Toward L-Selectin Inhibition". *Biomacromolecules* 12 (2011), pp. 2502–2511.

[14] P. L. Dubin, J. H. Gruber, J. Xia, and H. Zhang. "The effect of cations on the interaction between dodecylsulfate micelles and poly (ethyleneoxide)". *Journal of colloid and interface science* 148.1 (1992), pp. 35–41.

[15] B. B. Minsky, A. Atmuri, I. A. Kaltashov, and P. L. Dubin. "Counterion condensation on heparin oligomers". *Biomacromolecules* 14.4 (2013), pp. 1113–1121.

[16] J. Frueh, M. Gai, S. Halstead, and Q. He. "Structure and thermodynamics of polyelectrolyte complexes". *Polyelectrolytes*. Springer, 2014, pp. 19–86.

[17] J.-L. Barrat and J.-F. Joanny. "Theory of polyelectrolyte solutions". *Adv. Chem. Phys.* 94 (1996), pp. 1–66.

[18] Z. Ou and M Muthukumar. "Entropy and enthalpy of polyelectrolyte complexation: Langevin dynamics simulations". *J. Chem. Phys.* 124.15 (2006), p. 154902.

[19] X. Xu, M. Kanduč, J. Wu, and J. Dzubiella. "Potential of mean force and transient states in polyelectrolyte pair complexation". *J. Chem. Phys.* 145.3 (2016), p. 034901.

[20] L. Belloni. "Ionic condensation and charge renormalization in colloidal suspensions". *Colloids Surf., A* 140 (1998), pp. 227–243.

[21] A. V. Dobrynin. "Theory and simulations of charged polymers: From solution properties to polymeric nanomaterials". *Curr. Opin. Colloid Interface Sci.* 13.6 (2008), pp. 376–388.

[22] J. L. Lutkenhaus and P. T. Hammond. "Electrochemically enabled polyelectrolyte multilayer devices: from fuel cells to sensors". *Soft Matter* 3.7 (2007), pp. 804–816.

[23] E. Korin, O. Siton, A. Bettelheim, et al. "Fuel cells and ionically conductive membranes: an overview". *Reviews in Chemical Engineering* 23.1 (2007), p. 35.

[24] C. Cooper, P. Dubin, A. Kayitmazer, and S Turksen. "Polyelectrolyte–protein complexes". *Curr Opin Colloid Interface Sci* 10.1 (2005), pp. 52–78.

[25] A. F. Thünemann, M. Müller, H. Dautzenberg, J.-F. Joanny, and H. Löwen. "Polyelectrolyte complexes". *Polyelectrolytes with defined molecular architecture II*. Springer, 2004, pp. 113–171.

[26] M. Gai, J. Frueh, V. L. Kudryavtseva, R. Mao, M. V. Kiryukhin, and G. B. Sukhorukov. "Patterned Microstructure Fabrication: Polyelectrolyte Complexes vs Polyelectrolyte Multilayers". *Scientific Reports* 6 (2016).

[27] A. V. Kabanov. "Polymer genomics: an insight into pharmacology and toxicology of nanomedicines". *Adv. Drug Deliv. Rev.* 58.15 (2006), pp. 1597–1621.

[28] V. A. Kabanov. "From synthetic polyelectrolytes to polymer-subunit vaccines". *Pure Appl. Chem* 76.9 (2004), pp. 1659–1677.

[29] J. Jeon and A. V. Dobrynin. "Necklace globule and counterion condensation". *Macromolecules* 40.21 (2007), pp. 7695–7706.

[30] J. Dernedde et al. "Dendritic polyglycerol sulfates as multivalent inhibitors of inflammation". *Proc. Natl. Acad. Sci. U. S. A.* 107.46 (2010), pp. 19679–19684.

[31] P. Kesharwani, V. Gajbhiye, and N. K. Jain. "A review of nanocarriers for the delivery of small interfering RNA". *Biomaterials* 33.29 (2012), pp. 7138–7150.

[32] J Haesnler and F. Szoka. "Polymeric gene delivery: Principles and applications". *Bioconj. Chem* 4.5 (1993), pp. 372–379.

[33] P. Kesharwani, S. Banerjee, U. Gupta, M. C. I. M. Amin, S. Padhye, F. H. Sarkar, and A. K. Iyer. "PAMAM dendrimers as promising nanocarriers for RNAi therapeutics". *Mater. Today* 18.10 (2015), pp. 565–572.

[34] J. Giri, M. S. Diallo, A. J. Simpson, Y. Liu, W. A. Goddard, R. Kumar, and G. C. Woods. "Interactions of Poly(amidoamine) Dendrimers with Human Serum Albumin: Binding Constants and Mechanisms". *ACS Nano* 5.5 (2011), p. 3456.

[35] B. Klajnert and M. Bryszewska. "Dendrimers: properties and applications". *Acta Biochim Pol* 48.1 (2001), pp. 199–208.

[36] M. Ballauff and C. N. Likos. "Dendrimers in Solution: Insight from Theory and Simulation". *Angew. Chem., Int. Ed.* 43 (2004), p. 2998.

[37] W. Tian and Y. Ma. "Theoretical and computational studies of dendrimers as delivery vectors". *Chem. Soc. Rev.* 42 (2013), p. 705.

[38] C. C. Lee, J. A. MacKay, J. M. Fréchet, and F. C. Szoka. "Designing dendrimers for biological applications". *Nature Biotechnology* 23 (2005), pp. 1517–1526.

[39] D. Gröger et al. "Synthesis and Biological Evaluation of Radio and Dye Labeled Amino Functionalized Dendritic Polyglycerol Sulfates as Multivalent Anti-Inflammatory Compounds". *Bioconjug. Chem.* 24.9 (2013), pp. 1507–1514.

[40] M. Weinhart, D. Gröger, S. Enders, S. B. Riese, J. Dernedde, R. K. Kainthan, D. E. Brooks, and R. Haag. "The Role of Dimension in Multivalent Binding Events: Structure–Activity Relationship of Dendritic Polyglycerol Sulfate Binding to L-Selectin in Correlation with Size and Surface Charge Density". *Macromol. Biosci.* 11.8 (2011), pp. 1088–1098.

[41] A. Sousa-Herves, P. Würfel, N. Wegner, J. Khandare, K. Licha, R. Haag, P. Welker, and M. Calderón. "Dendritic polyglycerol sulfate as a novel platform for paclitaxel delivery: pitfalls of ester linkage". *Nanoscale* 7 (2015), pp. 3923–3932.

[42] P. Dubin, J. Bock, R. Davis, D. N. Schulz, and C. Thies, eds. *Macromolecular Complexes in Chemistry and Biology*. Springer Verlag, New York, 1994.

[43] J. van der Gucht, E. Spruijt, M. Lemmers, and M. A. C. Stuart. "Polyelectrolyte complexes: Bulk phases and colloidal systems". *J. Colloid Interface Sci.* 361.2 (2011), pp. 407–422.

[44] D. Srivastava and M. Muthukumar. *Macromolecules* 27 (1994), pp. 1461–1465.

[45] R. G. Winkler, M. O. Steinhauser, and P. Reineker. *Phys. Rev. E* 66 (2002), p. 021802.

[46] M. Neu, D. Fischer, and T. Kissel. *J. Gene Med.* 7 (2005), 992–1009.

[47] J. Ziebarth and Y. Wang. *Biophys. J.* 97 (2009), pp. 1971–1983.

[48] J. Zhou, J. Liu, T. Shi, Y. Xia, Y. Luo, and D. Liang. "Phase separation of siRNA–polycation complex and its effect on transfection efficiency". *Soft Matter* 9.0 (2013), pp. 2262–2268.

[49] D. Langevin. "Complexation of oppositely charged polyelectrolytes and surfactants in aqueous solutions. A review". *Advances in colloid and interface science* 147 (2009), pp. 170–177.

[50] S. V. Lyulin, L. J. Evers, P. van der Schoot, A. A. Darinskii, A. V. Lyulin, and M. A. J. Michels. "Effect of Solvent Quality and Electrostatic Interactions on Size and Structure of Dendrimers. Brownian Dynamics Simulation and Mean-Field Theory". *Macromolecules* 37.12 (2004), pp. 3049–3063.

[51] H. Lee and R. G. Larson. "Molecular Dynamics Simulations of PAMAM Dendrimer-Induced Pore Formation in DPPC Bilayers with a Coarse-Grained Model". *J. Phys. Chem. B* 110.37 (2006), pp. 18204–18211.

[52] J. S. Kłos and J.-U. Sommer. "Simulations of Terminally Charged Dendrimers with Flexible Spacer Chains and Explicit Counterions". *Macromolecules* 43 (2010), pp. 4418–4427.

[53] W. Tian and Y. Ma. "pH-responsive dendrimers interacting with lipid membranes". *Soft Matter* 8 (2012), p. 2627.

[54] P. K. Maiti, Y. Li, T. Cagin, and W. A. Goddard. "Structure of polyamidoamide dendrimers up to limiting generations: A mesoscale description". *J. Chem. Phys.* 130 (2009), p. 144902.

[55] C. C. Lee, J. A. MacKay, J. M. J. Frechet, and F. C. Szoka. "Designing dendrimers for biological applications". *Nature Biotechnology* 23 (2005), pp. 1517–1526.

[56] S. Svenson and D. A. Tomalia. "Dendrimers in biomedical applications—reflections on the field". *Adv, Drug. Deliv. Rev* 57 (2005), pp. 2106–2129.

[57] D. E. Owens and N. A. Peppas. "Opsonization, biodistribution, and pharmacokinetics of polymeric nanoparticles". *Intern. J. Pharamceutics* 307 (2006), pp. 93–102.

[58] D. I. Cattoni, O. Chara, S. B. Kaufman, and F. L. G. Flecha. "Cooperativity in Binding Processes: New Insights from Phenomenological Modeling". *PLOS ONE* 10.12 (2015), e0146043.

[59] M. Calderón, M. A. Quadir, S. K. Sharma, and R. Haag. "Dendritic Polyglycerols for Biomedical Applications". *Adv. Mater.* 22 (2010), pp. 190–218.

[60] A. Boreham et al. "Detecting and Quantifying Biomolecular Interactions of a Dendritic Polyglycerol Sulfate Nanoparticle Using Fluorescence Lifetime Measurements". *Molecules* 21.1 (2015), p. 22.

[61] C. N. Likos. "Effective interactions in soft condensed matter physics". *Physics Reports* 348.4 (2001), pp. 267–439.

[62] D. Andelman. "Introduction to electrostatics in soft and biological matter". *Soft condensed matter physics in molecular and cell biology* 6 (2006).

[63] H.-J. Butt, K. Graf, and M. Kappl. *Physics and chemistry of interfaces*. John Wiley & Sons, 2006.

[64] G. Hartley. "The application of the Debye-Hückel theory to colloidal electrolytes". *Transactions of the Faraday Society* 31 (1935), pp. 31–50.

[65] N. Hoffmann, C. N. Likos*, and J.-P. Hansen. "Linear screening of the electrostatic potential around spherical particles with non-spherical charge patterns". *Molecular Physics* 102.9-10 (2004), pp. 857–867.

[66] D. Ben-Yaakov, D. Andelman, D. Harries, and R. Podgornik. "Beyond standard Poisson–Boltzmann theory: ion-specific interactions in aqueous solutions". *Journal of Physics: Condensed Matter* 21.42 (2009), p. 424106.

[67] J. N. Israelachvili. *Intermolecular and surface forces*. Academic press, 2011.

[68] M. Lund and B. Jönsson. "A Mesoscopic Model for Protein-Protein Interactions in Solution". *Biophys. J.* 85 (2003), pp. 2940–2947.

[69] B. Derjaguin. "Theory of the stability of strongly charged lyophobic sols and the adhesion of strongly charged particles in solutions of electrolytes". *Acta Physicochim. USSR* 14 (1941), pp. 633–662.

[70] B. Derjaguin and L Landau. "A theory of the stability of highly charged lyophobic sols and of the adhesion of particles in electrolyte solutions". *Zh. Eksp. Teor. Fiz.* 15 (1945), p. 662.

[71] E. J. W. Verwey, J. T. G. Overbeek, and J. T. G. Overbeek. *Theory of the stability of lyophobic colloids*. Courier Corporation, 1999.

[72] R. M. Fuoss, A. Katchalsky, and S. Lifson. "The potential of an infinite rod-like molecule and the distribution of the counter ions". *Proceedings of the National Academy of Sciences* 37.9 (1951), pp. 579–589.

[73] T. Alfrey, P. W. Berg, and H. Morawetz. "The counterion distribution in solutions of rod-shaped polyelectrolytes". *Journal of Polymer Science Part A: Polymer Chemistry* 7.5 (1951), pp. 543–547.

[74] M. Deserno, C. Holm, and S. May. "Fraction of condensed counterions around a charged rod: Comparison of Poisson- Boltzmann theory and computer simulations". *Macromolecules* 33.1 (2000), pp. 199–206.

[75] M. L. Bret and B. H. Zimm. "Distribution of counterions around a cylindrical polyelectrolyte and Manning's condensation theory". *Biopolymers* 23.2 (1984), pp. 287–312.

[76] J. Ray and G. S. Manning. "An Attractive Force between Two Rodlike Polyions Mediated by the Sharing of Condensed Counterions". *Langmuir* 10.0 (1994), pp. 2450–2461.

[77] G. S. Manning and J. Raya. "Counterion Condensation Revisited". *J. Biomol. Struct. Dyn.* 16.2 (1998), pp. 461–476.

[78] M. Deserno, C. Holm, and S. May. "Fraction of Condensed Counterions around a Charged Rod: Comparison of PoissonBoltzmann Theory and Computer". *Macromolecules* 33.1 (2000), pp. 199–206.

[79] H. Qian and J. A. Schellman. "Transformed PoissonBoltzmann Relations and Ionic Distributions". *J. Phys. Chem. B* 104.48 (2000), pp. 11528–11540.

[80] A. Naji and R. R. Netz. "Scaling and universality in the counterion-condensation transition at charged cylinders." *Phys Rev E Stat Nonlin Soft Matter Phy* 73.5 (2006), p. 056105.

[81] W. K. Kim and W. Sung. "Charge density and bending rigidity of a rodlike polyelectrolyte: Effects of multivalent counterions". *Physical Review E* 83.5 (2011), p. 051926.

[82] I. A. Shkel, O. V. Tsodikov, and J. M. Thomas Record. "Asymptotic solution of the cylindrical nonlinear Poisson–Boltzmann equation at low salt concentration: Analytic expressions for surface potential and preferential interaction coefficient". *Proc. Natl. Acad. Sci. U. S. A.* 99.5 (2001), pp. 2597–2602.

[83] A. R. Denton. "Poisson-Boltzmann Theory of Charged Colloids: Limits of the Cell Model for Salty Suspensions". *J. Phys.: Condens. Matter* 22.0 (2010), pp. 364108–1–12.

[84] J. Heyda and J. Dzubiella. "Ion-specific counterion condensation on charged peptides: Poisson–Boltzmann vs. atomistic simulations". *Soft Matter* 8.0 (2012), pp. 9338–9344.

[85] G. Manning. "Limiting Laws and Counterion Condensation in Polyelectrolyte Solutions I. Colligative Properties". *J. Chem. Phys.* 51.3 (1969), p. 924.

[86] B. O'Shaughnessy and Q. Yang. "Manning-Oosawa counterion condensation". *Phys. Rev. Lett.* 94.4 (2005), p. 048302.

[87] L. M. Penafiel and T. A. Litovitz. "Counterion condensation and ionic conductivity". *J. Chem. Phys.* 96.4 (1992), pp. 3033–3038.

[88] G. S. Manning. "Is the counterion condensation point on polyelectrolytes a trigger of structural transition?" *J. Chem. Phys.* 89.6 (1988), pp. 3772–3777.

[89] G. S. Manning. "Counterion condensation theory constructed from different models". *Physica A* 231.1-3 (1996), pp. 236–253.

[90] A. V. Dobrynin and M. Rubinstein. "Counterion condensation and phase separation in solutions of hydrophobic polyelectrolytes". *Macromolecules* 34.6 (2001), pp. 1964–1972.

[91] P González-Mozuelos and M. O. de la Cruz. "Ion condensation in salt-free dilute polyelectrolyte solutions". *J. Chem. Phys.* 103.8 (1995), pp. 3145–3157.

[92] A. Deshkovski, S. Obukhov, and M. Rubinstein. "Counterion phase transitions in dilute polyelectrolyte solutions". *Phys. Rev. Lett.* 86.11 (2001), p. 2341.

[93] M. J. Stevens and K. Kremer. "Structure of salt-free linear polyelectrolytes". *Phys. Rev. Lett.* 71.14 (1993), p. 2228.

[94] H. Ohshima, T. W. Healy, and L. R. White. "Accurate analytic expressions for the surface charge density/surface potential relationship and double-layer potential distribution for a spherical colloidal particle". *J. Colloid Interface Sci.* 90 (1982), pp. 17–26.

[95] L. Bocquet, E. Trizac, and M. Aubouy. "Effective charge saturation in colloidal suspensions". *J. Chem. Phys.* 117 (2002), p. 8138.

[96] G. S. Manning. "Counterion Condensation on Charged Spheres, Cylinders, and Planes". *J. Phys. Chem. B* 111.29 (2007), pp. 8554–8559.

[97] R. Netz and H. Orland. "Variational charge renormalization in charged systems". *Eur. Phys. J. E* 11 (2003), p. 301.

[98] F. Chiba, T. Chou, L. J. Twyman, and M. Wagstaff. "Dendrimers as size selective inhibitors to protein–protein binding". *Chem. Commun.* 36 (2008), pp. 4351–4353.

[99] K. Henzler, B. Haupt, K. Lauterbach, A. Wittemann, O. Borisov, and M. Ballauff. "Adsorption of β-lactoglobulin on spherical polyelectrolyte brushes: direct proof of counterion release by isothermal titration calorimetry". *Journal of the American Chemical Society* 132.9 (2010), pp. 3159–3163.

[100] M. T. Record, C. F. Anderson, and T. M. Lohman. "Thermodynamic analysis of ion effects on the binding and conformational equilibria of proteins and nucleic acids: the roles of ion association or release, screening, and ion effects on water activity". *Quarterly reviews of biophysics* 11.02 (1978), pp. 103–178.

[101] C. F. Anderson and M. T. R. Jr. "Salt dependence of oligoion-polyion binding: a thermodynamic description based on preferential interaction coefficients". *Journal of Physical Chemistry* 97.27 (1993), pp. 7116–7126.

[102] M. J. L. And and H. H. Strey. "Phase Diagrams of Stoichiometric PolyelectrolyteSurfactant Complexes". *Macromolecules* 36.25 (2005), pp. 9549–9558.

[103] P. P. Ewald. "Die Berechnung optischer und elektrostatischer Gitterpotentiale". *Annalen der Physik* 369.3 (1921), pp. 253–287.

[104] A. Y. Toukmaji and J. A. Board. "Ewald summation techniques in perspective: a survey". *Computer physics communications* 95.2-3 (1996), pp. 73–92.

[105] U. Essmann, L. Perera, M. L. Berkowitz, T. Darden, H. Lee, and L. G. Pedersen. "A Smooth Particle Mesh Ewald Method". *J. Chem. Phys.* 103.19 (1995), pp. 8577–8593.

[106] H. Berendsen. "Transport properties computed by linear response through weak coupling to a bath". *Computer Simulation in Materials Science*. Springer, 1991, pp. 139–155.

[107] G. Bussi, D. Donadio, and M. Parrinello. "Canonical sampling through velocity rescaling". *The Journal of chemical physics* 126.1 (2007), p. 014101.

[108] H. J. Berendsen, J. v. Postma, W. F. van Gunsteren, A. DiNola, and J. Haak. "Molecular dynamics with coupling to an external bath". *The Journal of chemical physics* 81.8 (1984), pp. 3684–3690.

[109] M. Parrinello and A. Rahman. "Polymorphic transitions in single crystals: A new molecular dynamics method". *Journal of Applied physics* 52.12 (1981), pp. 7182–7190.

[110] S. Nosé and M. Klein. "Constant pressure molecular dynamics for molecular systems". *Molecular Physics* 50.5 (1983), pp. 1055–1076.

[111] W. G. Hoover. "Canonical dynamics: equilibrium phase-space distributions". *Physical review A* 31.3 (1985), p. 1695.

[112] B. Hess, C. Kutzner, D. van der Spoel, and E. Lindahl. "GROMACS 4: Algorithms for Highly Efficient, Load-Balanced, and Scalable Molecular Simulation". *J. Chem. Theory Comput.* 4.3 (2008), pp. 435–447.

[113] R. M. Neumann. "Entropic approach to Brownian movement". *American Journal of Physics* 48.0 (1980), p. 354.

[114] B. Hess, C. Holm, and N. van der Vegt. "Osmotic coefficients of atomistic NaCl (aq) force fields". *J. Chem. Phys.* 124.0 (2006), p. 164509.

[115] I. Kalcher and J. Dzubiella. "Structure-thermodynamics relation of electrolyte solutions". *J. Chem. Phys.* 130.0 (2009), p. 134507.

[116] P. Carbone and L. Lue. "Prediction of Bulk Density and Molecular Packing in Model Dendrimers with Different Chain Stiffness". *Macromolecules* 43 (2010), pp. 9191–9197.

[117] M. K. Gilson and H.-X. Zhou. "Calculation of protein-ligand binding affinities". *Annual review of biophysics and biomolecular structure* 36 (2007).

[118] B. J. Berne and R. Pecora. *Dynamic light scattering. With applications to chemistry, biology, and physics*. Wiley, 1976.

[119] D. Henry. "The cataphoresis of suspended particles. Part I. The equation of cataphoresis". *Proceedings of the Royal Society of London A: Mathematical, Physical and Engineering Sciences*. Vol. 133. 821. The Royal Society. 1931, pp. 106–129.

[120] V. Smoluchowski. "Graetz Handbuch der Electrizitat und des Magnetismus, vol. II". *VEB Georg Thieme, Barth, Leipzig* (1921), p. 385.

[121] H. Ohshima. "Electrophoretic mobility of soft particles". *Journal of colloid and interface science* 163.2 (1994), pp. 474–483.

[122] H. Ohshima. "A simple expression for Henry's function for the retardation effect in electrophoresis of spherical colloidal particles". *Journal of Colloid and Interface Science* 168.1 (1994), pp. 269–271.

[123] R. W. O'Brien. "Electrophoretic Mobility of A Spherical Colloidal Particle". *Journal of the Chemical Society Faraday Transactions* 74.1 (1978), pp. 1607–1626.

[124] I. Jelesarov and H. R. Bosshard. "Isothermal titration calorimetry and differential scanning calorimetry as complementary tools to investigate the energetics of biomolecular recognition". *Journal of molecular recognition* 12.1 (1999), pp. 3–18.

[125] J. B. Chaires. "Calorimetry and Thermodynamics in Drug Design". *Annu. Rev. Biophys.* 37 (2008), 135–51.

[126] T. Cedervall, I. Lynch, S. Lindman, T. Berggård, E. Thulin, H. Nilsson, K. A. Dawson, and S. Linse. "Understanding the nanoparticle-protein corona using methods to quantify exchange rates and affinities of proteins for nanoparticles". *Proc. Natl. Acad. Sci. U. S. A.* 104.7 (2007), p. 2050.

[127] M. K. Gilson and H.-X. Zhou. "Calculation of protein-ligand binding affinities". *Annual Review of Biophysics* 36 (2007), pp. 21–42.

[128] R. I. Masel. *Principles of adsorption and reaction on solid surfaces*. Vol. 3. John Wiley & Sons, Inc, 1996.

[129] S. Yu, X. Xu, C. Yigit, M. van der Giet, W. Zidek, J. Jankowski, J. Dzubiella, and M. Ballauff. "Interaction of human serum albumin with short polyelectrolytes: a study by calorimetry and computer simulations". *Soft Matter* 11 (2015), pp. 4630–4639.

[130] M. Rubinstein. "Discretized model of entangled-polymer dynamics". *Phys. Rev. Lett.* 59 (1987), p. 1946.

[131] C. Yigit, J. Heyda, M. Ballauff, and J. Dzubiella. "Like-charged protein-polyelectrolyte complexation driven by charge patches". *J. Chem. Phys.* 143.0 (2015), p. 064905.

[132] S. Yu, X. Xu, C. Yigit, M. van der Giet, W. Zidek, J. Jankowski, J. Dzubiella, and M. Ballauff. "Interaction of human serum albumin with short polyelectrolytes: a study by calorimetry and computer simulations". *Soft Matter* 11.0 (2015), pp. 4630–4639.

[133] J.-L. Popot et al. "Amphipols: polymeric surfactants for membrane biology research". *Cell. Mol. Life Sci.* 60.8 (2003), pp. 1559–1574.

[134] F. Wiesbrock, R. Hoogenboom, M. A. M. Leenen, M. A. R. Meier, and U. S. Schubert. "Investigation of the Living Cationic Ring-Opening Polymerization of 2-Methyl-, 2-Ethyl-, 2-Nonyl-, and 2-Phenyl-2-oxazoline in a Single-Mode Microwave Reactor". *Macromolecules* 38.12 (2005), pp. 5025–5034.

[135] E. Pezron, L. Leibler, and F. Lafuma. "Complex formation in polymer-ion solutions. 2. Polyelectrolyte effects". *Macromolecules* 22.6 (1989), pp. 2656–2662.

[136] U. Essmann, L. Perera, M. L. Berkowitz, T. Darden, H. Lee, and L. G. Pedersen. "A smooth particle mesh Ewald method". *J. Chem. Phys.* 103.0 (1995), p. 8577.

[137] M. Wardell, Z. Wang, J. X. Ho, J. Robert, F. Ruker, J. Ruble, and D. C. Carter. "The atomic structure of human methemalbumin at 1.9 Å". *Biochemical and biophysical research communications* 291.4 (2002), pp. 813–819.

[138] J. K. Noel, P. C. Whitford, K. Y. Sanbonmatsu, and J. . N. Onuchic. "SMOG@ ctbp: simplified deployment of structure-based models in GROMACS". *Nucleic acids research* 38.suppl_2 (2010), W657–W661.

[139] C. Clementi, H. Nymeyer, and J. N. Onuchic. "Topological and energetic factors: what determines the structural details of the transition state ensemble and "en-route" intermediates for protein folding? An investigation for small globular proteins". *Journal of molecular biology* 298.5 (2000), pp. 937–953.

[140] V. Tozzini. "Coarse-grained models for proteins". *Current opinion in structural biology* 15.2 (2005), pp. 144–150.

[141] D. C. Grahame. "The Electrical Double Layer and the Theory of Electrocapillarity". *Chem. Rev.* 1947.3 (1947), pp. 441–501.

[142] I. Prigogine, S. A. Rice, S. L. Carnie, and G. M. Torrie. "The Statistical Mechanics of the Electrical Double Layer". *Advance in Chemical Physics* 56.0 (2007), pp. 1–139.

[143] S. Liu and M. Muthukumar. *J. Chem. Phys.* 116 (2002), p. 9975.

[144] W. C. K. Poon and D. Andelman, eds. *Soft Condensed Matter Physics in Molecular and Cell Biology*. Taylor & Francis, 2006.

[145] M. T. R. Jr, T. M. Lohman, and P. de Haseth. "Ion effects on ligand-nucleic acid interactions". *J. Mol. Biol.* 25.2 (1976), pp. 145–158.

[146] D. P. Mascotti and T. M. Lohman. "Thermodynamic extent of counterion release upon binding oligolysines to single-stranded nucleic acids". *Proc. Natl. Acad. Sci. U. S. A.* 87.0 (1990), pp. 3142–3146.

[147] R. Beck, J. Deek, J. B. Jones, and C. R. Safinya. *Nature Materials* 9 (2010), p. 40.

[148] B. Peng and M. Muthukumar. "Modeling competitive substitution in a polyelectrolyte complex". *J. Chem. Phys.* 143 (2015), p. 243133.

[149] S. W. Cranford, C. Ortiz, and M. J. Buehler. "Mechanomutable properties of a PAA/PAH polyelectrolyte complex: rate dependence and ionization effects on tunable adhesion strength". *Soft Matter* 6 (2010), pp. 4175–4188.

[150] P. E. Rouse. *J. Chem. Phys.* 21 (1953), p. 1272.

[151] V Ball, M Winterhalter, P Schwinte, P. Lavalle, J.-C. Voegel, and P Schaaf. "Complexation mechanism of bovine serum albumin and poly (allylamine hydrochloride)". *The Journal of Physical Chemistry B* 106.9 (2002), pp. 2357–2364.

[152] M. Kabiri and L. D. Unsworth. "Application of isothermal titration calorimetry for characterizing thermodynamic parameters of biomolecular interactions: peptide self-assembly and protein adsorption case studies". *Biomacromolecules* 15.10 (2014), pp. 3463–3473.

[153] M. J. Stevens. "Simple Simulations of DNA Condensation". *Biophys. J.* 80 (2001), pp. 130–139.

[154] Z. Ou and M. Muthukumar. "Langevin dynamics of semiflexible polyelectrolytes: Rod-toroid–globule-coil structures and counterion distribution". *J. Chem. Phys.* 123 (2005), p. 074905.

[155] R. Chang and A. Yethiraj. "Dilute Solutions of Strongly Charged Flexible Polyelectrolytes in Poor Solvents: Molecular Dynamics Simulations with Explicit Solvent". *Macromolecules* 39 (2006), pp. 821–828.

[156] G. Reddy, R. Chang, and A. Yethiraj. "Adsorption and Dynamics of a Single Polyelectrolyte Chain near a Planar Charged Surface: Molecular Dynamics Simulations with Explicit Solvent". *J. Chem. Theory Comput.* 2.3 (2006), pp. 630–636.

[157] G. Reddy and A. Yethiraj. "Solvent effects in polyelectrolyte adsorption: Computer simulations with explicit and implicit solvent". *J. Chem. Phys.* 132 (2010), p. 074903.

[158] X. Xu, Q. Ran, P. Dey, R. Nikam, R. Haag, M. Ballauff, and J. Dzubiella. "Charged Dendrimers Revisited: Effective Charge and Surface Potential of Dendritic Polyglycerol Sulfate". *Macromolecules* 50.12 (2017). DOI: 10.1021/acs.macromol.7b00742, pp. 4579–4769.

[159] B. Hess, C. Kutzner, D. van der Spoel, and E. Lindahl. "GROMACS 4: Algorithms for Highly Efficient, Load-Balanced, and Scalable Molecular Simulation". *J. Chem. Theory Comput.* 4.3 (2008), pp. 435–447.

[160] L. D. Schuler, X. Daura, and W. F. van Gunsteren. "An improved GROMOS96 force field for aliphatic hydrocarbons in the condensed phase". *J. Comput. Chem.* 22.11 (2001), pp. 1205–128.

[161] H. J. C. Berendsen, J. R. Grigera, and T. P. Straatsma. "The missing term in effective pair potentials". *J. Phys. Chem.* 91.24 (1987), pp. 6269–6271.

[162] M. J. e. a. Frisch. *Gaussian 09 Revision D.01*. Gaussian Inc. Wallingford CT 2009. 2009.

[163] B. A. C. Horta, P. F. J. Fuchs, W. F. van Gunsteren, and P. H. Hünenberger. "New Interaction Parameters for Oxygen Compounds in the GROMOS Force Field: Improved Pure-Liquid and Solvation Properties for Alcohols, Ethers, Aldehydes, Ketones, Carboxylic Acids, and Esters". *J. Chem. Theory Comput.* 7 (2011), pp. 1016–1031.

[164] D. Jozica. "GROMOS Developer". *Private Communication* (2013).

[165] X. Tang, P. H. Koenig, and R. G. Larson. "Molecular Dynamics Simulations of Sodium Dodecyl Sulfate Micelles in Water - The Effect of the Force Field". *J. Phys. Chem. B* 118 (2014), pp. 3864–3880.

[166] D. A. Evans. "History of the Harvard ChemDraw Project". *Angew. Chem., Int. Ed.* 53 (2014), p. 11140.

[167] F. Müller-Plathe. "Coarse-graining in polymer simulation: from the atomistic to the mesoscopic scale and back". *ChemPhysChem* 3 (2002), p. 754.

[168] D. Reith, M. Pütz, and F. Müller-Plathe. "Deriving effective mesoscale potentials from atomistic simulations". *J. Comput. Chem.* 24 (2003), p. 1624.

[169] S. Huißmann, A. Wynveen, C. N. Likos, and R. Blaak. "The effects of pH, salt and bond stiffness on charged dendrimers". *J. Phys.: Condens. Matter* 22.23 (2010), p. 232101.

[170] S. Huißmann, A. Wynveen, C. N. Likos, and R. Blaak. "Conformations of high-generation dendritic polyelectrolytes". *J. Mat. Chem.* 20 (2010), pp. 10486–10494.

[171] A. K. Das and P.-Y. Hsiao. "Charged Dendrimers in Trivalent Salt Solutions under the Action of DC Electric Fields". *J. Phys. Chem. B* 118 (2014), pp. 6265–6276.

[172] D. E. Smith and L. X. Dang. "Computer simulations of NaCl association in polarizable water". *J. Chem. Phys.* 100 (1993), p. 3757.

[173] I. Kalcher, J. C. F. Schulz, and J. Dzubiella. "Electrolytes in a nanometer slab-confinement: Ion-specific structure and solvation forces". *J. Chem. Phys.* 133 (2010), p. 164511.

[174] S. Huißmann, C. N. Likos, and R. Blaak. "Explicit vs Implicit Water Simulations of Charged Dendrimers". *Macromolecules* 45 (2012), p. 2562.

[175] B. I. Voit. "Dendritic polymers: from aesthetic macromolecules to commercially interesting materials". *Acta Polym.* 46.2 (1995), pp. 87–99.

[176] J. Dernedde et al. "Dendritic polyglycerol sulfates as multivalent inhibitors of inflammation". *Proc. Natl. Acad. Sci. U. S. A.* 107.46 (2010), pp. 19679–19684.

[177] S. Alexander, P. M. Chaikin, P. Grant, G. J. Morales, and P. Pincus. "Charge renormalization, osmostic pressure, and bulk modulus of colloidal crystals: Theory". *J. Chem. Phys.* 80 (1983), p. 5776.

[178] G. V. Ramanathan. "Counterion condensation in micellar and colloidal solutions". *J. Chem. Phys.* 88.6 (1988), p. 3887.

[179] A. Sunder, R. Hanselmann, H. Frey, and R. Mülhaupt. "Controlled synthesis of hyperbranched polyglycerols by ring-opening multibranching polymerization". *Macromolecules* 32.13 (1999), pp. 4240–4246.

[180] H. Türk, R. Haag, and S. Alban. "Dendritic polyglycerol sulfates as new heparin analogues and potent inhibitors of the complement system". *Bioconjugate chemistry* 15.1 (2004), pp. 162–167.

[181] J. S. Kłos and J.-U. Sommer. "Simulations of Neutral and Charged Dendrimers in Solvents of Varying Quality". *Macromolecules* 46 (2013), pp. 3107–3117.

[182] D. A. J. Gillespie, J. E. Hallett, O. Elujoba, A. F. C. Hamzah, R. M. Richardson, and P. Bartlett. "Counterion condensation on spheres in the salt-free limit". *Soft Matter* 10 (2014), pp. 566–577.

[183] J. Lyklema. *Fundamentals of interface and colloid science: vol. II, Solid-liquid interfaces*. Academic Press, London, 1995.

[184] S. Ahualli, Á. V. Delgado, F. Carrique, and M. L. Jiménez. *AC Electrokinetics of Concentrated Suspensions of Soft and Hairy Nanoparticles: Model and Experiments*. John Wiley & Sons, Inc., 2016.

[185] R. J. Hunter. *Foundations of Colloid Science*. Oxford University Press, Oxford, 2001.

[186] X. Xu, Q. Ran, P. Dey, R. Nikam, R. Haag, M. Ballauff, and J. Dzubiella. "Counterion-release entropy governs the inhibition of serum proteins by polyelectrolyte drugs". *Biomacromolecules* 19.2 (2018), pp. 409–416.

[187] J. K. Noel, P. C. Whitford, K. Y. Sanbonmatsu, and J. N. Onuchic. "SMOG@ctbp: simplified deployment of structure-based models in GROMACS". *Nucleic Acids Res.* 38 (2010), W657–W661.

[188] M. Ramanadham, L. Sieker, and L. Jensen. "Refinement of triclinic lysozyme: II. The method of stereochemically restrained least squares". *Acta Crystallogr.,Sect.B* 46 (1990), p. 63.

[189] P. Mehta-D'souza et al. "Glycan Bound to the Selectin Low Affinity State Engages Glu-88 to Stabilize the High Affinity State under Force". *J. Biol. Chem.* 292.6 (2017), pp. 2510–2518.

[190] B. J. Graves et al. "Insight into E-selectin/ligand interaction from the crystal structure and mutagenesis of the lec/EGF domains". *Nature* 367.6463 (1994), pp. 532–538.

[191] D. B. Hough and L. R. White. "The Calculation of Hamaker Constants From Lifshitz Theory With Applications to Wetting Phenomena". *Adv. Colloid Interface Sci.* 14.1 (1980), pp. 3–41.

[192] H. Türk, R. Haag, and S. Alban. "Dendritic Polyglycerol Sulfates as New Heparin Analogues and Potent Inhibitors of the Complement System". *Bioconjug. Chem.* 15.1 (2004), p. 162.

[193] C. Yigit, N. Welsch, M. Ballauff, and J. Dzubiella. "Protein sorption to charged microgels: Characterizing binding isotherms and driving forces". *Langmuir* 28.40 (2012), pp. 14373–14385.

[194] A. L. Woelke, C. Kuehne, T. Meyer, G. Galstyan, J. Dernedde, and E.-W. Knapp. "Understanding Selectin Counter-Receptor Binding from Electrostatic Energy Computations and Experimental Binding Studies". *J. Phys. Chem. B* 117 (2013), p. 16443.

[195] A. G. Cherstvy. "Electrostatic interactions in dense DNA phases and protein-DNA complexes". *Electrostatics*. InTech. 2012.

[196] F. Gago. "Stacking interactions and intercalative DNA binding". *Methods* 14.3 (1998), pp. 277–292.

[197] Y. Zhong, M. Dimde, D. Stöbener, F. Meng, C. Deng, Z. Zhong, and R. Haag. "Micelles with Sheddable Dendritic Polyglycerol Sulfate Shells Show Extraordinary Tumor Targetability and Chemotherapy In Vivo". *ACS Appl. Mater. Interfaces* 8 (2016), p. 41.

Acknowledgements

I would like to begin by thanking my supervisor Prof. Dr. Joachim Dzubiella, who gives me a profound support both to my PhD thesis and personal life. Four years ago, he was the one who opened this interesting topic down to the nano scale for me and consistently guide me how to do research based on curiosity and passion. Thank you, Prof. Dr. Dzubiella, I will never forget the moments we were together in Berlin facing the most ambitious scientific challenges and your optimism in any occasions. You set yourself as a role model for me, not only as a creative scientist, but also as an excellent football player.

I owe a special thank to Prof. Dr. Matthias Ballauff for his endless support, substantial opinions and encouragements at the experimental side throughout my PhD study.

I am very appreciated Dr. Stefan Kirstein, Prof. Dr. Felix Höfling as well as Prof. Dr. Caterina Cocchi for accepting my invitation as the committee members.

I gratefully acknowledge the financial support from Chinese Scholar Council.

I express my sincere thanks to all the members of soft matter theory group for those scientific discussions and inspirations, beers and parties, which create me fun and determination to finish this thesis. Special thanks to Mila, Rohit, Wonkyu, Karol and Matej for reviewing this thesis. Many thanks also to other HZB colleagues, Prof. Dr. Yan Lu, Shun Yu, He Jia, Sasa Gu, Jie Cao, Shilin Mei, Martin, and Andy for a wonderful stay with you all in HZB.

My deepest gratitude goes to my family in China for your faithful accompany through many of my ups and downs. I dedicate this thesis to my father and mother.

Selbständigkeitserklärung

Hiermit versichere ich, dass ich die vorliegende Dissertation selbständig verfasst und keine anderen als die angegebenen Quellen und Hilfsmittel verwendet habe.

Ferner erkläre ich, dass ich nicht anderweitig mit oder ohne Erfolg versucht habe, eine Dissertation einzureichen oder mich einer Doktorprüfung zu unterziehen.

Berlin, den

.....
Xiao Xu